STRUCTURAL AND OPTICAL PROPERTIES OF STRAINED-LAYER SUPERLATTICES

Thesis by

Richard Henry Miles

In Partial Fulfillment of the Requirements

for the Degree of

Doctor of Philosophy

California Institute of Technology

Pasadena, California

1989

(Submitted August 18, 1988)

Acknowledgments

It is a pleasure to acknowledge my advisor, Dr. T. C. McGill, whose guidance and support have contributed tremendously to this work and to my own personal and scientific development.

I am fortunate to have benefited from interactions with a great number of people at Caltech. I especially wish to thank Dr. T. A. Tombrello, whose enthusiasm has been passed to many students, this one included. I would also like to thank Dr. S. I. Chan, who has always given freely and gladly of his time to discuss numerous matters, both personal and professional.

Many students, past and present, have contributed greatly to my years as a graduate student. Little of the optical work could have been done without the experience patiently passed along by Dr. Steve Hetzler. I have also profited from useful discussions with Drs. G. Y. Wu and T. E. Schlesinger. I especially wish to acknowledge the people with whom I have interacted extensively: Dr. Bob Hauenstein, who was always happy to share his keen curiosity and deep understanding of physics; Matthew Johnson, to whom I owe the better half of my experimental technique, and who is every bit as foolhardy as myself on a mountain; and Mike Jackson, whose insight, good nature, and good sense are a pleasure to encounter. It has been a delight interacting on numerous occasions with Dave Chow, to whom I am particularly grateful for a critical reading of Chapter 1, and with Yasantha Rajakarunanayake, who has so often taken the time to explain theory to an experimentalist. It is also a pleasure to acknowledge many discussions with my classmates, Wesley Boudville and Ted Woodward, as well as with Dr. Dave Ting, Ed Croke, Ed Yu, and Pete Zampardi.

Many thanks are due Marcia Hudson and Carol McCollum, without whose help on many matters, administrative and otherwise, the group would rapidly grind to a halt. I have greatly enjoyed conversing with Brian Cole in the brief moments

free to an engineer working with a multichamber MBE machine. I also wish to recognize the excellent secretarial help of Vere Snell, who is greatly missed.

I have profited from many valuable discussions with Dr. J. O. McCaldin, Dr. D. L. Smith of Los Alamos National Laboratories, and Mr. O. J. Marsh and Dr. A. T. Hunter of Hughes Research Laboratories. I also wish to thank Dr. M. D. Strathman of Charles Evans and Associates, for performing the RBS measurements; Dr. C. W. Nieh, who provided the TEM work on the Ge_xSi_{1-x} samples; Dr. P. P. Chow of Perkin-Elmer, who provided the Ge_xSi_{1-x} samples; and Dr. J.-P. Faurie of the University of Illinois, who provided the $Cd_xZn_{1-x}Te$ samples.

I would like to acknowledge the financial support of the California Institute of Technology, International Business Machines corporation, General Telephone, the Army Research Office, and the Office of Naval Research.

Finally, I wish to acknowledge my parents, without whom none of this would have been possible, and my wife Mayumi, who put up with all of this.

Abstract

This thesis describes investigations into the optical and structural properties of strained-layer superlattices. The purpose of the work was twofold: to establish the merits of strained-layer structures in applications, particularly to optoelectronics; and to examine structural characteristics of superlattices in which the lattice-mismatch between adjacent layers is large. Optical properties of CdTe/ZnTe superlattices have been examined through photoluminescence experiments. Observed band gaps have been compared with those expected from calculations of electronic band structure, including effects that are due to strain. Band gaps of a variety of II-VI superlattices have been calculated based on the agreement between theory and experiment in the CdTe/ZnTe system. The accommodation of lattice mismatch has been investigated for CdTe/ZnTe and $Ge_{0.5}Si_{0.5}/Si$ superlattices. The assumptions behind traditional single-film critical thicknesses and their extensions to multilayer structures were of particular interest in these studies.

In Chapter 2 we use photoluminescence experiments to examine the optical properties of CdTe/ZnTe superlattices grown on a variety of $Cd_xZn_{1-x}Te$ buffer layers. The work was motivated by interest in wide-band-gap II-VI's as possible visible light emitters and detectors and, more generally, by interest in the effects of strain and dislocations on the optical properties of strained-layer superlattices. Photoluminescence from the superlattices is observed to be several orders of magnitude more intense than from a $Cd_{0.37}Zn_{0.63}Te$ alloy. Spectra are dominated by Gaussian distributions of excitonic lines. The 20-30meV widths of these distributions show that superlattice layer thicknesses were controlled to approximately one monolayer. Identifying the superlattice band gaps as the high-energy edges of the observed excitonic luminescence yields sample energy gaps substantially lower than expected for alloys. Observed gaps are in excellent agreement with those calculated from a $\vec{k} \cdot \vec{p}$ model, assuming strain appropriate to a free-standing structure. This

configuration is one in which dislocations at the superlattice/buffer-layer interface have redistributed strain within an otherwise dislocation-free superlattice in a manner that minimizes the elastic strain energy within the structure. The free-standing configuration is argued to be plausible in view of calculated critical thicknesses and strain relaxation rates. Calculations of the effects of a free-standing strain on the electronic band structure of CdTe/ZnTe superlattices show that strain can substantially reduce band gaps (on the order of 100meV for a 6% mismatch), and causes transitions from type-I to type-II band alignments. Attempts to observe laser oscillation in these CdTe/ZnTe superlattice structures have proven unsuccessful to date, although $Cd_{0.25}Zn_{0.75}Te/ZnTe$ structures have recently been reported to lase.

Chapter 3 describes a structural study of the CdTe/ZnTe superlattices examined in Chapter 2. Strain fields and dislocation densities are inferred from x-ray diffraction, *in situ* reflection high-energy electron diffraction (RHEED), and transmission electron microscopy (TEM). All of our samples are observed to exceed the critical thickness for the nucleation of misfit-accommodating dislocations. Although each of the structures appears to be highly defective, the free-standing limit appears to be plausible, as defect densities drop substantially within a micron of the superlattice/buffer-layer interface, regardless of the buffer layer used. Although several samples substantially exceed predicted critical thicknesses, the sample that shows the smallest degree of residual strain lies below limits derived from a previous empirical study. This result demonstrates that dislocation formation in superlattices is not appropriately characterized by applying traditional critical thickness models to an alloy of equivalent total thickness and average composition. Variations in strain fields appear to be correlated with sample growth conditions. As growth parameters are neglected in traditional energy-balancing models of critical thickness, it is argued that activation barriers associated with the nucleation or glide of dislocations can substantially inhibit the relaxation of strain beyond the equilibrium limits.

In Chapter 4 we demonstrate that the accommodation of lattice mismatch in $Ge_{0.5}Si_{0.5}/Si$ superlattices is highly dependent on the conditions under which a sample is grown. Dislocation densities of $1.5 \times 10^5 cm^{-1}$ drop to levels undetectable by TEM ($< 10^5 cm^{-2}$) as the growth temperature of compositionally identical superlattices is lowered from 530 °C to 365 °C. Thus, by lowering growth temperatures, it is possible to freeze a structure in a highly strained metastable state well beyond the critical thickness limits calculated by equilibrium theories. There appears to be a large kinetic barrier blocking dislocation nucleation or glide; the effect we observe cannot be explained by mismatched thermal expansion coefficients alone. These results are contrary to initial studies of Ge_xSi_{1-x} alloys, which appear to display critical thicknesses relatively independent of temperature over the ranges described here. Recognizing that defect creation can be inhibited in severely mismatched superlattices should be important in growing heavily strained films of high quality.

Finally, the Appendix contains maps of band gap as a function of layer thicknesses for a variety of II-VI superlattice systems, calculated using the Bastard model described in Chapter 2. Agreement with experiment is good for the CdTe/ZnTe superlattices examined here. As mentioned in Chapter 1, comparison of these calculated gaps with those measured experimentally leads to a prediction of $\Delta E_v = 1.0 \pm 0.1 eV$ for the ZnSe/ZnTe valence band offset.

Parts of this thesis have been or will be published under the following titles:

Chapter 1:

Variation in the Properties of Superlattices with Band Offsets,

T. C. McGill, R. H. Miles, and G. Y. Wu, *Mater. Res. Soc. Symp. Proc.* **90**, 143 (1987).

Band Structure of ZnSe-ZnTe Superlattices,

Y. Rajakarunanayake, R. H. Miles, G. Y. Wu, and T. C. McGill, *Phys. Rev. B* **37**, 10215 (1988).

Band Offset of the ZnSe-ZnTe Superlattices: A fit to photoluminescence data by $k \cdot p$ theory,

Y. Rajakarunanayake, R. H. Miles, G. Y. Wu, and T. C. McGill, *J. Vac. Sci. Technol. B*, to be published.

Energy-band Structure of ZnSe-ZnTe Superlattices Calculated by $k \cdot p$ Theory,

Y. Rajakarunanayake, R. H. Miles, G. Y. Wu, and T. C. McGill, submitted to *Optical Engineering*.

Chapter 2:

Photoluminescence Spectra from CdTe-ZnTe Superlattices,

R. H. Miles, G. Y. Wu, M. B. Johnson, T. C. McGill, J. P. Faurie, and S. Sivananthan, *Bull. Am. Phys. Soc.* **31**, 654 (1986).

Photoluminescence Studies of ZnTe/CdTe Strained-layer Superlattices,

R. H. Miles, G. Y. Wu, M. B. Johnson, T. C. McGill, J. P. Faurie, and S. Sivananthan, *Appl. Phys. Lett.* **48**, 1383 (1986).

Chapter 3:

Structure of CdTe/ZnTe Superlattices,

R. H. Miles, T. C. McGill, S. Sivananthan, X. Chu, and J. P. Faurie, *J. Vac. Sci. Technol. B* **5**, 1263 (1987).

Perspectives on Formation and Properties of Semiconductor Interfaces,

R. S. Bauer, R. H. Miles, and T. C. McGill, in *Semiconductor Interfaces: Formation and Properties*, edited by G. Le Lay, J. Derrien, and N. Boccara (Springer, Berlin, 1987), p. 372.

Superlattices of II-VI Semiconductors,

R. H. Miles, J. O. McCaldin, and T. C. McGill, *J. Cryst. Growth* **85**, 188 (1987).

Chapter 4:

Opportunities in Devices and Physics,

T. C. McGill, R. H. Miles, R. J. Hauenstein, and O. J. Marsh, in *Proceedings of the 2nd International Symposium on Si MBE* (Electrochemical Society, Pennington, USA, 1988), p. 1.

Photoluminescence Studies of Ge/Si Superlattices,

R. H. Miles, T. C. McGill, P. P. Chow, O. J. Marsh, and R. J. Hauenstein, *Bull. Am. Phys. Soc.* **33**, 1349 (1988).

Dependence of Critical Thickness on Growth Temperature in Ge_xSi_{1-x}/Si Superlattices,

R. H. Miles, T. C. McGill, P. P. Chow, D. C. Johnson, R. J. Hauenstein, C. W. Nieh, and M. D. Strathman, *Appl. Phys. Lett.* **52**, 916 (1988).

Accommodation of Lattice Mismatch in Ge_xSi_{1-x}/Si Superlattices,

R. H. Miles, P. P. Chow, D. C. Johnson, R. J. Hauenstein, O. J. Marsh, C. W. Nieh, M. D. Strathman, and T. C. McGill, *J. Vac. Sci. Technol. B*, to be published.

Raman Study of Temperature-Dependent Strain Relaxation in SiGe/Si Strained-Layer Superlattices,

R. J. Hauenstein, A. T. Hunter, R. H. Miles, T. C. McGill, and P. P. Chow, in preparation.

Contents

List of Figures

List of Tables

Chapter 1

Introduction

1.1 Introduction to thesis

This thesis describes investigations into the optical and structural properties of strained-layer superlattices. The experimental work is divided between studies of CdTe/ZnTe and Ge_xSi_{1-x}/Si structures. Although the results presented are derived exclusively from these systems, many of the conclusions can be extended to other heteroepitaxial structures in which the lattice match between constituent materials is poor. The excellent optical properties of the CdTe/ZnTe superlattices have recently been matched by other wide-band-gap II-VI superlattices, and the nature of the dislocation network observed in these structures is similar to that of extended defects in strained III-V and group-IV semiconductor systems. To date, the Ge_xSi_{1-x}/Si structural results have not been confirmed in other materials systems, but it is believed that the nature of stress relaxation should be similar in other lattice-mismatched heterostructures.

The purpose of Chapter 1 is to summarize the results obtained in the thesis and to place the work in context. Section 1.2 briefly outlines the motivation for investigations into small structures. Section 1.3 describes strained-layer superlattices with an emphasis on the advantages of these structures over alloys or closely lattice-matched superlattices. Effects that are due to strain are the subject of Section 1.4. Perturbations of the electronic band structure arising from strain are discussed (Section 1.4.1), as well as defect formation and the attempts to model it in a strained heterostructure (Section 1.4.2). The thesis is summarized in Section 1.5. A photoluminescence study of CdTe/ZnTe superlattices is outlined in Section 1.5.1. The section that follows this describes investigations of the structural characteristics of these samples, addressing in particular the degree to which lattice mismatch is accommodated by elastic strain for growth on a variety of templates. Lastly, Section 1.5.3 summarizes a study of the effects of growth conditions on defect formation in $Ge_{0.5}Si_{0.5}/Si$ superlattices.

1.2 Background

The drive to create electronic devices that are both faster and more compact is leading to enormous improvements in device fabrication and processing techniques. Foremost amongst the improvements in crystal growth has been development of the techniques of molecular beam epitaxy (MBE) and chemical vapor deposition (CVD), which has made possible the fabrication of epitaxial films with deposition controlled to the submonolayer coverage level. While promising to greatly improve the speed and packing density of conventional solid-state electronic devices, these technologies have also forced changes in descriptions of the physics behind old devices and introduced a host of new structures demonstrating a wealth of new characteristics.

When device dimensions approach the de Broglie wavelength of an electron in a crystal,* device characteristics are rarely described adequately by extensions

---

*Within the effective mass approximation, $\lambda = \frac{h}{mc} \approx 2.4\frac{m}{m^*}\,\text{Å} \approx 35\,\text{Å}$ in GaAs.

of bulk material properties through semiclassical theories. Several factors contribute to this breakdown. Effects associated with confinement radically alter the electronic states within a structure, making quantum mechanical descriptions necessary. Crystal band gaps are shifted substantially from those of the constituent materials, yielding very different radiative recombination energies. Phenomena such as electron or hole tunneling can make large, if not dominant, contributions to the behavior of a given device. Transport properties are further removed from classical theory by scattering lengths that are comparable to device dimensions.

While greatly changing the descriptions necessary to predict the characteristics of a particular structure, reducing device size also presents the possibility of growth of a large number of lattice-mismatched heterostructures with a minimum of structural defects. The desirability of commensurate* growth has long been recognized; extended dislocations often act as sources of electrically and optically active point defects or are themselves active, to the detriment of device performance. Until recently, this had limited attention to a few closely-lattice-matched pairs (*e.g.*, GaAs/AlAs and HgTe/CdTe) in applications in which device performance was at a premium. This situation has changed in the last few years, however, as it has become possible to reproducibly deposit films that are sufficiently thin to inhibit dislocation formation for lattice mismatches as large as 7%. Relaxing the constraint of lattice match to this degree has opened to investigation a great number of new commensurate heterostructures.

The subject of this thesis is the strained-layer superlattice, a structure that was first suggested in 1983 by Osbourn[1] and that springs directly from the capability to grow ultrathin epitaxial films with a high degree of reproducibility. The potential

---

*While the term *commensurate* is defined variously in the literature, we will restrict its use to heterostructures in which the interfaces between adjacent layers are dislocation-free. The "coherently strained" structure that results is one in which stress arising from lattice mismatch is accommodated purely by elastic strain.

of these structures is great; relaxing the constraint of lattice match allows a large number of new heterostructures to be grown, while the strain that results from a substantial lattice mismatch can have enormous effects on the optical and electrical properties of a structure. However, the obstacles to introducing strained-layer structures within devices are considerable; extended structural defects are readily introduced during growth and processing, and the stability of strained devices under prolonged use remains uncertain.

The work presented here is aimed at three goals. It was primarily the hope of new light-emitters and detectors that initially stimulated the optical experiments described in Chapter 2. The effects on electronic band structure of strain arising from a substantial lattice mismatch are still uncertain, and this provided additional direction and motivation for the work in this chapter. The structural experiments presented in Chapters 3 and 4 investigated the limits on commensurate strained epitaxy and the nature of stress relaxation in strained superlattices. Resolution of these issues will be essential to the successful application of strained heterostructures.

1.3 Small structures

1.3.1 Superlattices

Semiconductor superlattices have attracted much attention since being proposed by Esaki and Tsu[2] in 1970. Fig. 1.1 is a schematic representation of such a structure. Growth takes place on a clean, heated substrate, starting typically with the deposition of one or more buffer layers of thickness on the order of a micron. While buffer layers are rarely essential to the superlattice itself, they serve several functions. An appropriate choice of buffer material and growth conditions can improve subsequent growth by providing a surface that is both cleaner and more

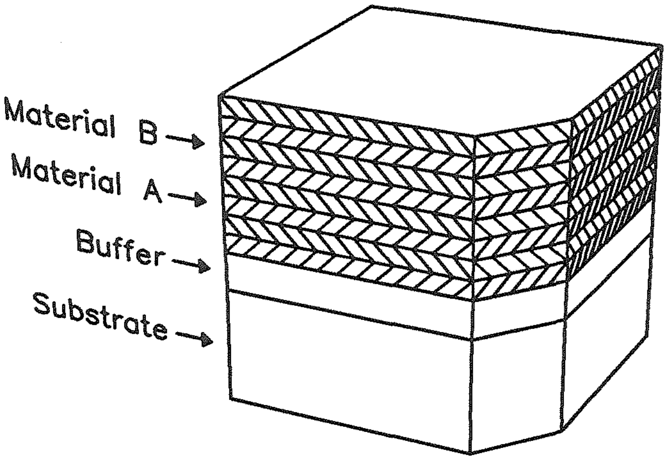

Figure 1.1: Schematic of a semiconductor superlattice, consisting of two distinct layers deposited consecutively and repeatedly to form a periodic structure. The superlattice is typically grown atop a comparatively thick substrate after deposition of one or more buffer layers. (From Ref. 3.)

abrupt than can be achieved by standard substrate preparation procedures. In addition, buffer layers can improve crystal quality by bending dislocations threading through the substrate, forcing them to the edge of a wafer rather than allowing them to propagate through subsequent overlayers. Lastly, the topmost buffer may act as a template for future growth, with the result that strain within a superlattice can sometimes be modulated by the choice of this top layer.

The superlattice itself is grown on top of the buffers and consists of thin layers of one semiconductor interleaved between thin layers of another. This alternating structure is typically repeated for many periods, with layer thicknesses and compositions controlled for optimal uniformity and regularity. While adjacent layers are compositionally distinct in the superlattices studied in this thesis, it is also possible to grow a superlattice by periodically grading the introduction of impurities during deposition of a single material.[4] Such modulation-doped superlattices display many of the electrical characteristics of compositionally graded structures.

Superlattices have several advantages over alloys. Although it is often possible to reproduce the band gap of a superlattice by growing an alloy composed of the same materials,* superlattices provide the parameter of layer thickness in addition to overall composition. The importance of this extra parameter is illustrated in Fig. 1.2, which depicts energy gaps and effective masses for transport normal to the layers in HgTe/CdTe superlattices. The abscissa and ordinate correspond to numbers of monolayers of CdTe and HgTe, respectively, per superlattice period. Whereas growth of an alloy with a given energy gap constrains the effective mass to one or two values, it is clear from Fig. 1.2 that by changing HgTe and CdTe layer thicknesses it is possible to adjust the effective mass over a comparatively wide range while maintaining a single value of the band gap.

Practical considerations sometimes provide additional motivation for growing superlattices rather than alloys. Although precise alloy composition can be difficult to reproduce with techniques such as MBE, layer thicknesses are easily monitored during growth. Although the situation is complicated by issues such as interdiffusion between adjacent superlattice layers and by the precision to which composition and layer thickness must be defined for a particular application, there are many circumstances in which superlattice characteristics are more readily reproduced than those of alloys. Alloy decomposition is another problem that can be circumvented by growing superlattices composed of alternating layers of pure material (this is one of the motivations for growing CdTe/ZnTe instead of $Cd_xZn_{1-x}Te$). Another practical consideration is the difficulty associated with growing a thick highly strained film. While it is possible to grow a thick commensurate superlattice consisting of layers strained alternately in tension and compression, growth of a

---

*This is *usually* the case, but not always; *e.g.*, strained $Ga_xIn_{1-x}Sb/Ga_yIn_{1-y}Sb$ superlattices can be grown with band gaps smaller than obtainable in $Ga_zIn_{1-z}Sb$ alloy films of comparable thickness.[5]

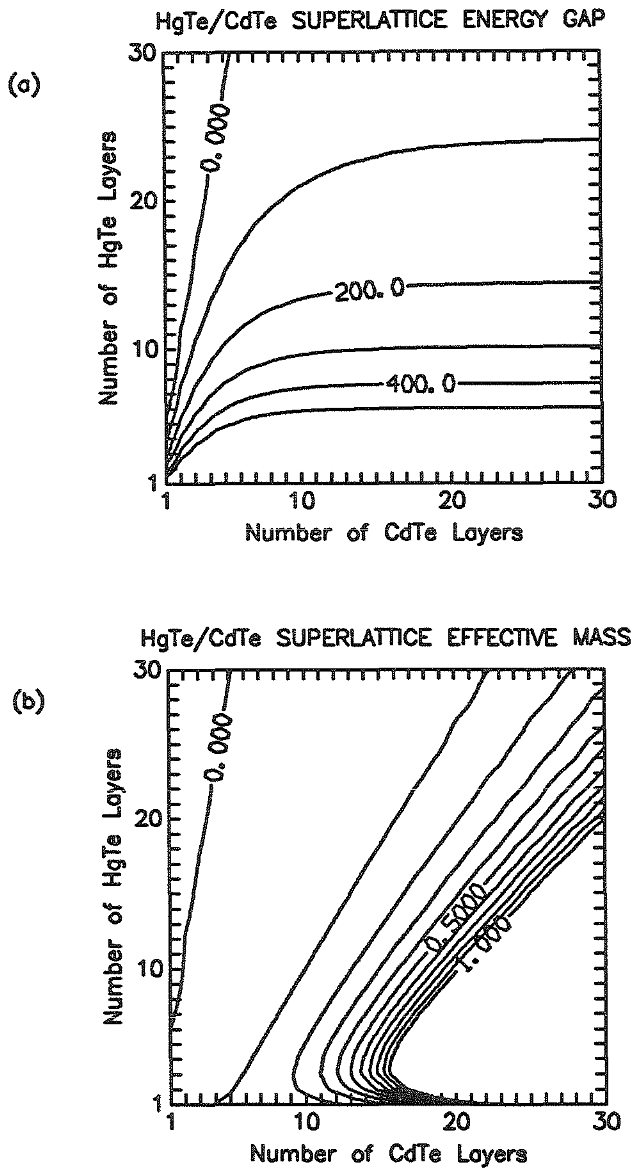

Figure 1.2: Properties of the HgTe/CdTe superlattice, calculated from a Bastard model[6] assuming zero valence band offset. The axes correspond to the number of HgTe and CdTe layers per superlattice period. (a) Energy band gaps of HgTe/CdTe superlattices at 4.2K. Energies are expressed in meV. (b) Effective masses for transport normal to the superlattice layers, expressed in fractions of the free-electron mass. Contours have been omitted for masses greater than m_e. (Adapted from Ref. 7.)

thick highly strained single film results in dislocation formation. This phenomenon is described in greater detail in Section 1.4.2.

Lastly, radiative efficiencies of superlattices have often been observed to be superior to those of alloys,[8,9] for reasons not entirely understood. Improvements have been attributed variously to carrier confinement in quantum wells,[10] defect and impurity gettering at interfaces,[11] and reductions in surface recombination velocities.[12] Differences in oscillator strengths do not appear to be sufficient to explain the radiative enhancements.[13] It is probable that each of these effects improves the radiative efficiencies of superlattices.

1.3.2 Strained-layer structures

It has been known for some time that overlayers deposited on a substrate to which they are poorly lattice matched often relieve mismatch stresses by developing dense networks of interfacial dislocations.[14,15,16,17] Although limiting the amount of material deposited on a substrate to a so-called "critical thickness" was long ago observed to inhibit the appearance of these structural defects, these limiting thicknesses were sufficiently thin to preclude defect-free epitaxial growth for all but a few closely lattice matched systems. The development of techniques such as MBE has made possible the growth of ultrathin epitaxial films, which has in turn opened to investigation a large number of commensurate heterostructures composed of poorly lattice-matched materials.

As illustrated in Fig. 1.3, very few semiconductors are lattice-matched well to others. The number of materials that can be usefully codeposited within a single growth chamber is further reduced by constraining pairs to be in the same group in the periodic table. This limitation springs from doping considerations; elements from one column of the periodic table act as electron donors or acceptors in a semiconductor composed of elements from other columns. Growing, for example,

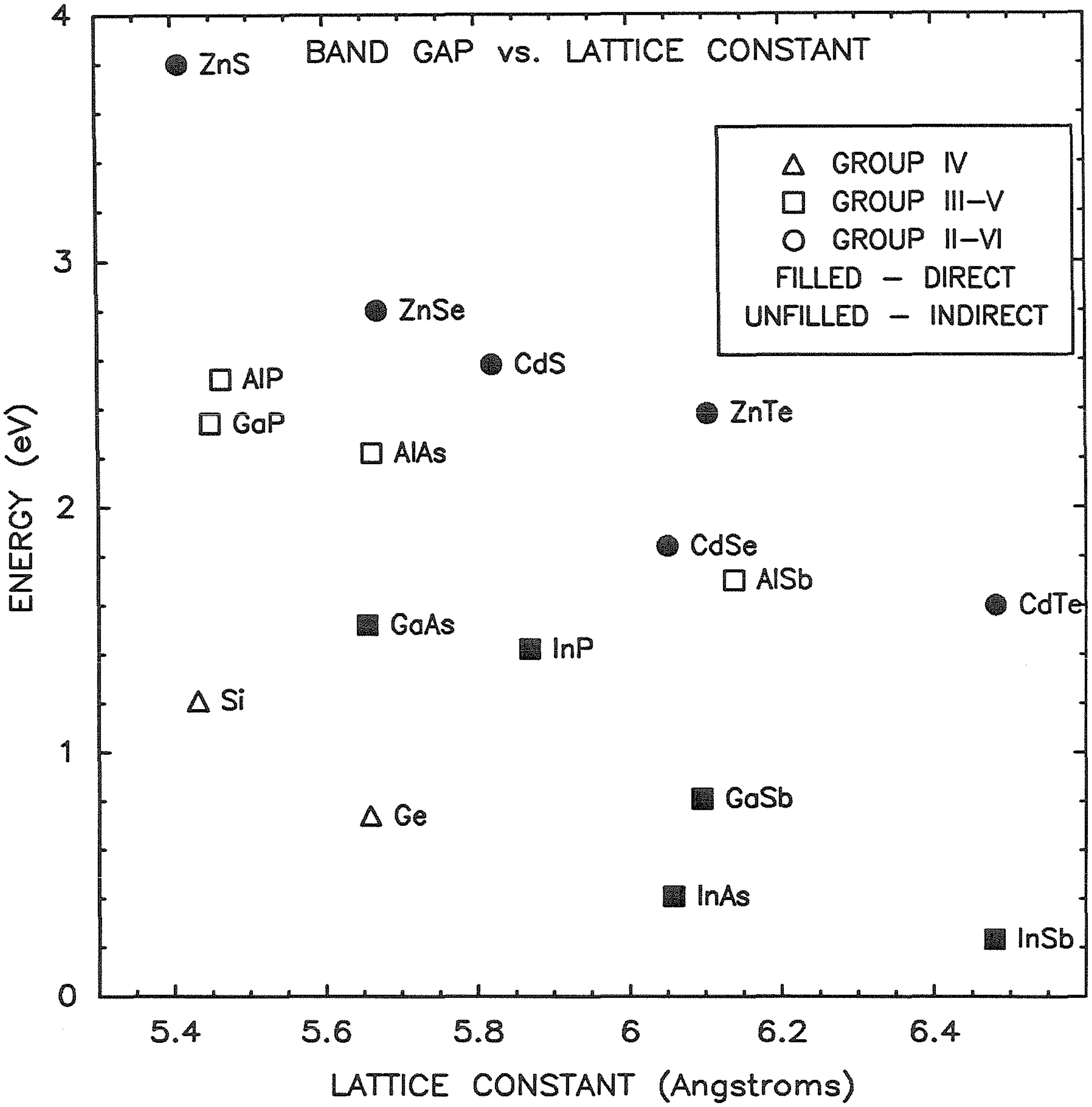

Figure 1.3: Energy band gaps and lattice constants of assorted semiconductors at 4.2K. Group-IV, III-V, and II-VI semiconductors are labeled differently, as indicated in the inset. Direct band gap materials are indicated with solid symbols, indirect with unfilled.[18,19,20]

type II-VI semiconductors in a III-V growth chamber can be expected to have long-term effects on the electrical and optical characteristics of future structures grown in that chamber. While some such pairs have been grown (*e.g.*, ZnSe with GaAs[21]), research on mixed-system heterostructures has been slow.

It is clear from Fig. 1.3 that relaxing the constraint of lattice match to allow growth of materials with lattice constants differing by as much as 7% greatly increases the number of material combinations possible within heterostructures. The elastic strain which arises from commensurate lattice-mismatched growth acts as a considerable perturbation on electronic band structure.[22] This effect is described in greater detail in Section 1.4.1. While strain cannot always be viewed as a free parameter to be adjusted at will,[9] it can be used to advantage. The interest in heterojunction bipolar transistors (HBT's) fabricated from Ge_xSi_{1-x} is fueled in large part by the effect of strain-induced conduction band splitting on transport in the growth direction. Strain-induced band-gap shrinkages have brought attention to $Ga_xIn_{1-x}Sb/Ga_yIn_{1-y}Sb$ superlattices as possible alternatives to $Hg_xCd_{1-x}Te$ for application as infrared detectors in the $8-12\,\mu$m range.[5] There are many other examples of structures in which strain can act as a beneficial perturbation.

Recently, strained films have been used to improve the structural quality of subsequent epitaxial growth. Thin strained-layer superlattices incorporated in buffer layers have been shown to greatly reduce the number of dislocations threading from a substrate to an overlayer.[16,23] At present it is not clear that lattice mismatch is intrinsic to this effect; it is possible that layered structures composed of materials differing only in elastic properties would bend dislocations along interfaces and out of a crystal. Lastly, it is sometimes possible to isolate mismatch-accommodating dislocations to a buffer-layer/substrate interface, greatly improving the structural perfection of an overlayer poorly lattice-matched to its substrate. This technique has been applied successfully in the $Ga_xIn_{1-x}Sb$ system,[5] where a $Ga_xIn_{1-x}Sb$

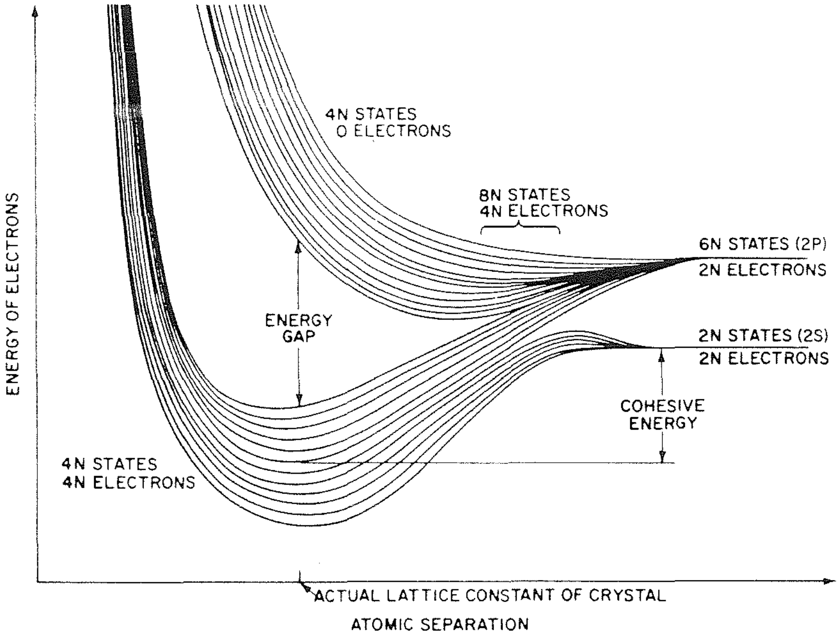

Figure 1.4: Banding of energy levels in diamond as atoms are drawn together. (From Ref. 24.)

buffer layer grossly mismatched to an InSb substrate eliminates microcracks and dislocations in a subsequent structure.

1.4 Effects arising from strain

1.4.1 Electronic band structure

The complex nature of the electronic band structure of solids arises directly from the interactions of electrons in close proximity to each other. As depicted in Fig. 1.4, distantly separated atoms display electronic levels at essentially identical energies. As atoms are drawn together, these levels interact to satisfy the Pauli Exclusion Principle, splitting and shifting according to the proximity and geometry of surrounding atoms. As can be inferred from Fig. 1.4, this interaction substantially alters the relative and absolute positions of electronic bands; changes in interatomic distances associated with strain will clearly have a substantial effect on the band structure.

The regular arrangement of atoms on a lattice greatly simplifies the electronic band structure of a crystal. Knowledge of the space group to which a particular crystal belongs allows predictions of the interactions and energetic degeneracies of the electronic states within that crystal. Strains are readily divided into two classes according to their effects on the crystal space group: hydrostatic strains, which (barring a phase transition) preserve the space group and consequently the high-symmetry degeneracies; and uniaxial, which in general lower the crystal symmetry and split these degeneracies. In the following discussion we will limit ourselves to considerations of the shifts of the conduction and valence bands under hydrostatic and $< 100 >$ uniaxial strains in zinc blende crystals. This is a case of real interest in strained-layer superlattices, as the majority of structures grown to date are either diamond or zinc blende in structure and are biaxially strained to fit a two-dimensional $< 100 >$- or $< 111 >$-oriented template.*

As is apparent from Fig. 1.4, hydrostatic strains change the absolute positions of the conduction and valence band edges, as well as the energy gap separating them. These shifts are approximately linear with atomic separation for small strains. Following the notation of Ref. 25, the change in absolute position of the valence band edge under hydrostatic dilation or contraction, ε, can be expressed in terms of a deformation potential a as $\Delta E_v = a\varepsilon$. We define a parameter c that satisfies an analogous relationship for the conduction band. While the change in energy gap under hydrostatic strain is readily measured and yields $(c - a)$ with high accuracy, the relative shifts of band edges in different materials (*i.e.*, the absolute values of a and c) are difficult to determine experimentally. Relative band

---

*Note that these biaxial strains are equivalent to sums of hydrostatic and uniaxial strains.

offsets across heterojunctions are typically determined for structures in which lattice mismatches are small or in which stresses have been relieved by the formation of misfit defects. The role of strain in determining the band offsets has not yet been measured. We have chosen to use values of a and c calculated by chemical bonding considerations.[26] Strained band offsets have been obtained by adding the shifts from these deformation potentials to the measured values of the unstrained band offsets. Recently, there have been calculations that suggest that hydrostatic strain has very little effect on the band offsets.[27] This issue remains to be resolved.

The effects of uniaxial strains on states at the Brillouin zone center are described by parameters b and d, which characterize band splittings under the influence of [100]– and [111]-oriented strains, respectively. Exciton splittings determined from reflection spectroscopy provide accurate estimates of these deformation potentials for stresses up to approximately 1kbar (equivalent to a strain of about 0.1% in these systems). Observed exciton splittings are approximately linear with applied stress at these pressures[28,29] but are assumed to deviate substantially from linearity for strains of the magnitude typically encountered in strained-layer superlattices. For [001]-oriented, zinc blende, strained-layer superlattices, the $\Gamma-$point band edges become

$$E_{\mathrm{LH}} = a\varepsilon + b(\varepsilon_{zz} - \varepsilon_{xx}) + 2\frac{b^2}{\Delta}(\varepsilon_{zz} - \varepsilon_{xx})^2 \tag{1.1}$$

$$E_{\mathrm{HH}} = a\varepsilon - b(\varepsilon_{zz} - \varepsilon_{xx}) \tag{1.2}$$

$$E_{\mathrm{CO}} = E_{\mathbf{gap}} + c\varepsilon \tag{1.3}$$

(to first order in spin-orbit splitting, Δ). Deformation potentials are typically on the order of electron-Volts. Values for zinc blende II-VI semiconductors are listed in Table 1.1.

The effects of strain on the band edges of a ZnSe/ZnTe superlattice are illustrated in Fig. 1.5. For the strained case we have calculated for a configuration in

Table 1.1: Deformation potentials of some zinc blende II-VI semiconductors. Energies are in eV.

Material	a^a	c^a	b	d
ZnTe	1.35	-2.7	-1.78^b	-4.58^b
ZnSe	1.35	-2.82	-1.2^c	-3.81^c
ZnS	1.58	-3.6	0.53^d	-3.71^d
CdTe	1.23	-2.2	-1.18^e	-4.83^e
CdSe	1.24	-2.47		
CdS	1.31	-2.68		

a. From Ref. 26.

b. From Ref. 28.

c. From Ref. 30.

d. From Ref. 31.

e. From Ref. 29.

which the elastic energy of a [100]-oriented, 50% ZnSe, 50% ZnTe structure has been minimized with respect to a single in-plane lattice constant. In this "free-standing" case the lattice constant is an average of the bulk lattice constants of the constituent materials, weighted by layer thicknesses and relative rigidities of the bulk materials (see Section 2.4.1). ZnSe, with a bulk lattice constant of 5.669 Å, is under biaxial tension when combined with ZnTe, which has an unstrained lattice constant of 6.104 Å. This biaxial tension is equivalent to a hydrostatic dilation and

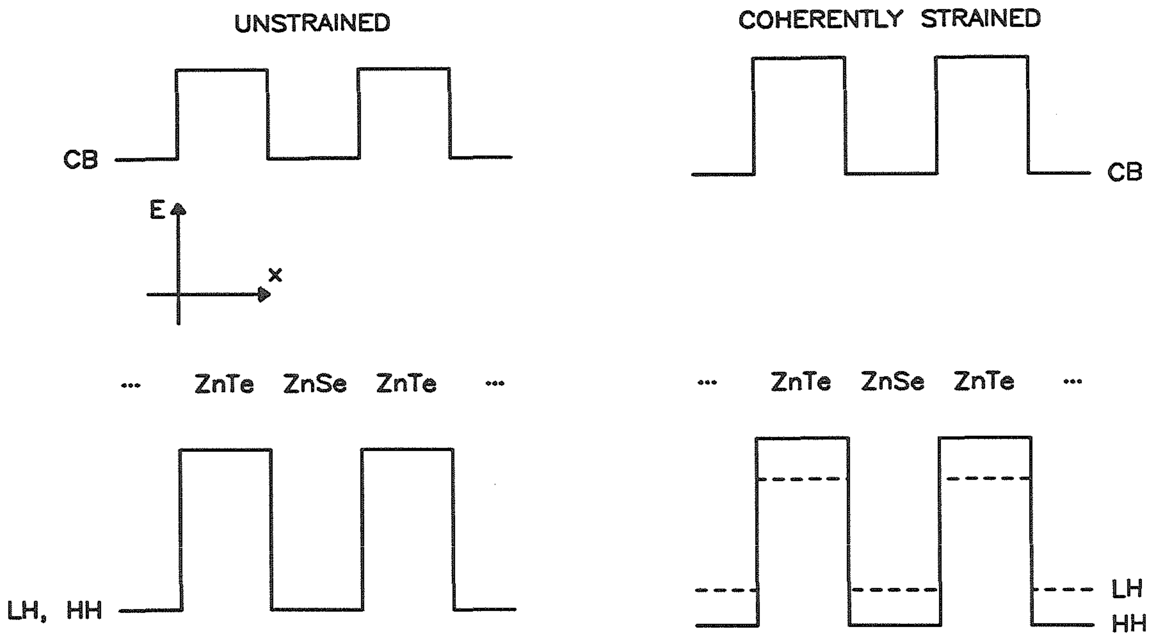

Figure 1.5: Effect of strain on the band edges in a ZnSe/ZnTe superlattice. A valence band offset of 1eV was assumed before the application of strain.[32]

a uniaxial compression. In this case the hydrostatic component shifts the ZnSe valence and conduction bands to lower the band gap by several tens of meV's, while the uniaxial component shifts the light hole band above the heavy hole by 218meV. Conversely, biaxial compression moves the ZnTe heavy-hole band above the light-hole by 253meV and further separates the conduction band edge from the energy of the unsplit valence bands. Note that the strained ZnTe band gap is actually smaller than that of unstrained ZnTe; uniaxial splitting more than compensates for the increase in band gap coming from hydrostatic compression.

While there are several methods for calculating electronic band structure that incorporate effects arising from strain,[25,33] our calculations are based on a $\vec{k} \cdot \vec{p}$ perturbation theory. The fact that the strain tensor ε_{ij} transforms like $k_i k_j$ under the symmetry operations of a given space group makes this technique particularly well suited to the incorporation of strain. In addition, this is the method of choice for calculations of optical properties since $< \psi_i|p|\psi_j >$ matrix elements are dealt with explicitly. These are readily related to oscillator strengths, from which it is possible to calculate optical properties of interest.

The $\vec{k} \cdot \vec{p}$ method is a perturbation technique that allows complex band structure to be calculated around a point for which the eigenvalues of the system are known. Details of the technique are described in Section 2.4.1. This method can, in principle, yield complex band structure to arbitrarily great accuracy as more bands are included and higher-order corrections are added to the Hamiltonian. As with any perturbation method, the approximations are best near the point at which the eigenvalues are known (in our case, the zone center). Uncertainties associated with deformation potentials are much larger than those associated with the $\vec{k} \cdot \vec{p}$ method for the superlattices we have considered.*

Results of the $\vec{k} \cdot \vec{p}$ calculations for the ZnSe/ZnTe system are shown in Fig. 1.6. The figure shows bulk band structures calculated for $\vec{k}_{||} = 0$ for the cases in which material is either unstrained or biaxially strained along $< 100 >$ directions. As in Fig. 1.5, the strained band structures were calculated under the assumption that the two in-plane $< 100 >$ lattice constants had adopted a value appropriate to a free-standing structure composed of equal amounts of ZnSe and ZnTe. It is apparent from the figure that the higher valence band is light-hole-like in ZnSe and heavy-hole-like in ZnTe. This could be expected to have a significant effect on transport of holes in this direction.

---

*The envelope function approximation starts to break down in the limit of very thin superlattice layers.[34] The thinnest layers we have considered are 20 Å, for which the approximation should still be good.

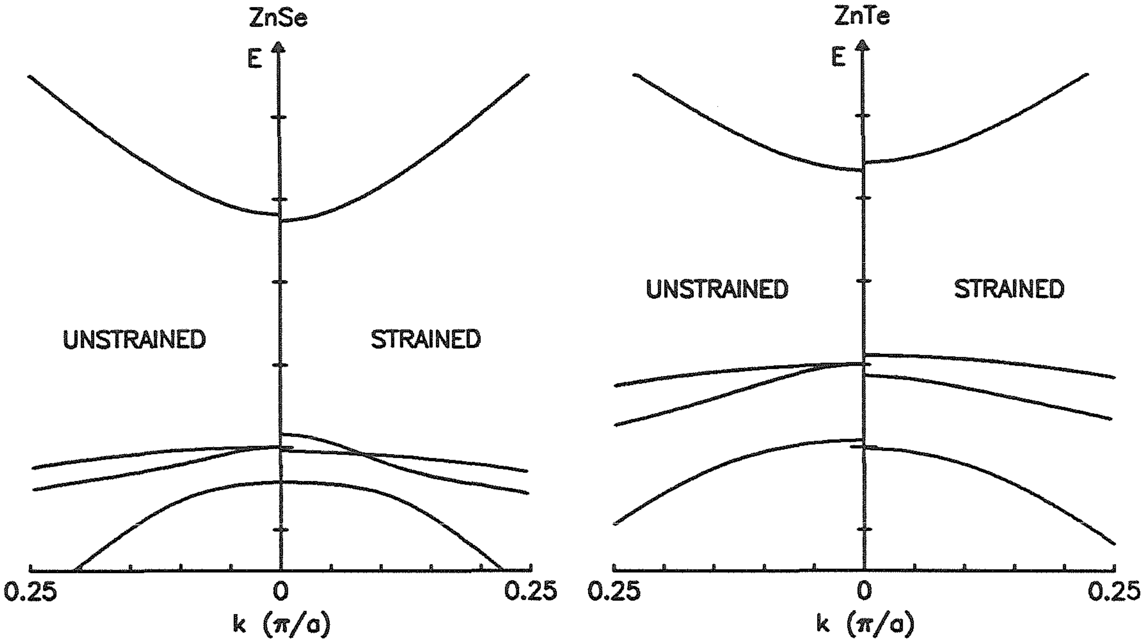

Figure 1.6: Electronic band structure of bulk ZnSe and ZnTe for $\vec{k}_{||} = 0$ showing the effects of strain. A ZnSe/ZnTe valence band offset of 1eV was assumed in aligning the band structures of the two materials in the unstrained case.[32] The strained band structure was calculated assuming a biaxial $< 100 >$ strain chosen to minimize the elastic energy of a coherent structure composed of equal quantities of ZnSe and ZnTe. Spacing between tick marks on the ordinate is 1eV. (Adapted from Ref. 32.)

1.4.2 Defect formation

Overlayers poorly lattice-matched to a substrate have long been known to generate mismatch-accommodating structural defects under certain circumstances.[14,15,16,17] The appearance of these misfit dislocations is typically observed when the film is grown beyond a "critical thickness," below which growth is relatively defect-free. Determining these critical thicknesses and understanding the nature of dislocation formation, nucleation, and interaction have become increasingly important with the development of techniques for fabricating heteroepitaxial structures composed of highly dissimilar materials. Dislocations create electrically active deep levels[24] that act as alternate carrier decay channels and also provide mechanisms for the generation of point defects and defect complexes.[35] Degradation of light-emitting diodes (LED's) has been associated with dark line defects created during nonradiative recombinations at dislocation-related deep levels,[35] and misfit dislocations appear to limit the gain of $\mathrm{Ge}_x\mathrm{Si}_{1-x}$ HBT's.[36] Growing dislocation-free structures is clearly desirable for a wide variety of device applications.

There are two limiting cases for lattice-mismatched growth, depicted in Figs. 1.7 and 1.8. In the dislocation-free case the overlayer is in perfect registry with the underlying lattice, with the result that the strained layer distorts tetragonally according to a biaxial analogue of Poisson's ratio ($\varepsilon_{zz} = -2(C_{12}/C_{11})\varepsilon_{xx}$). Alternatively, the mismatch can be accommodated purely by misfit defects. In this case, dislocations are regularly spaced at an interval of $(b \sin\beta \cos\gamma)/f$, where b is the Burger's vector associated with the particular type of dislocation, f is the mismatch $|a_0 - a_1|/a_1$, β is the angle between the Burger's vector and the dislocation line, and γ is that between the interface and glide plane.[15]

Early attempts by Van der Merwe[14,15] to model critical thickness relied on estimating the thickness at which the limiting case of the completely unstrained lattice becomes energetically favored over the dislocation-free strained lattice. Ac-

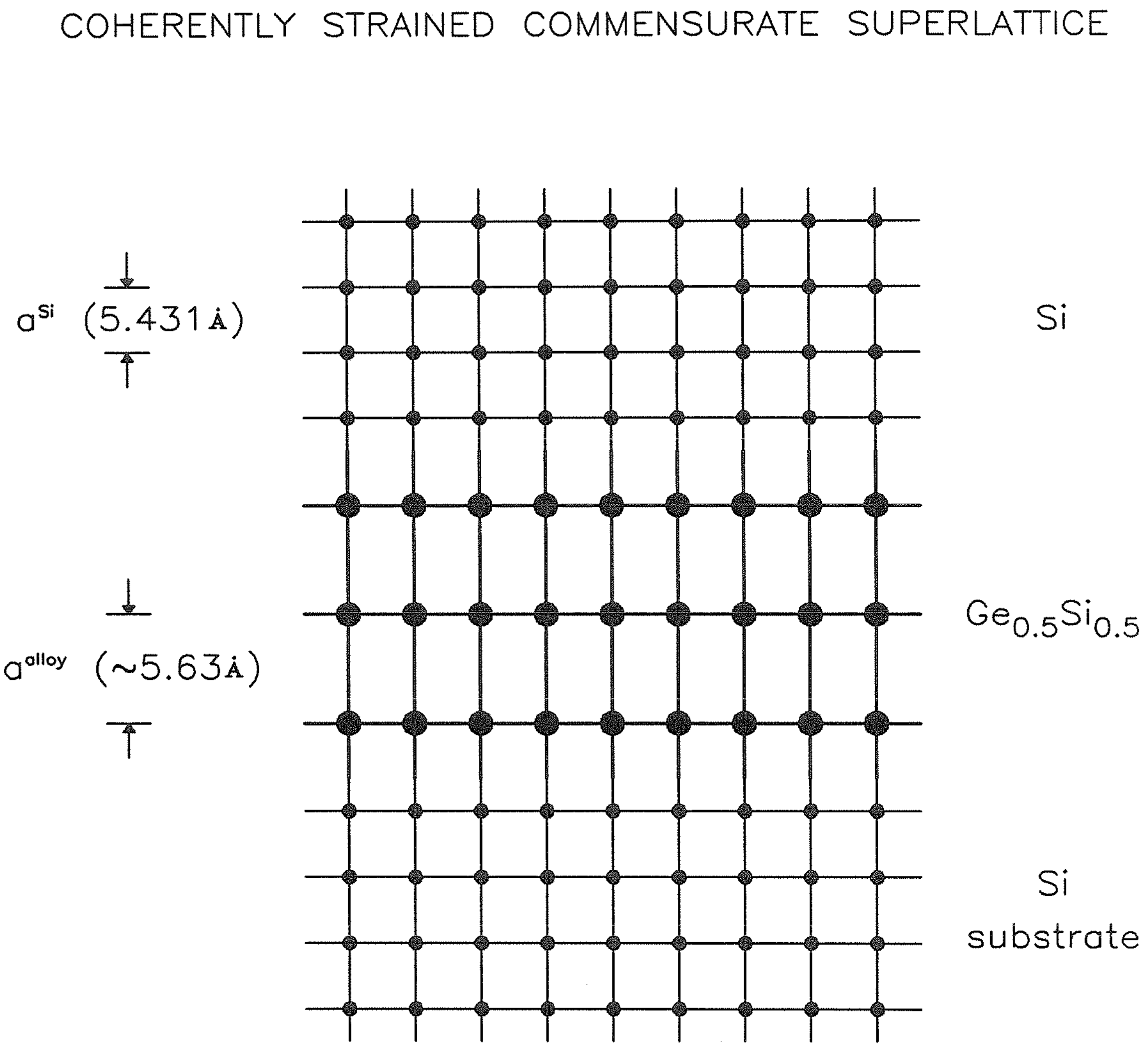

Figure 1.7: Schematic indicating the arrangement of unit cells in a coherently strained, commensurate superlattice. Atoms in the superlattice are in perfect registry with those in the substrate. In the case shown here all of the strain lies in the Ge_xSi_{1-x} layers, resulting in tetragonal distortion of these layers. The magnitude of the distortion has been exaggerated for clarity (the numerical lattice parameters are correct, however).

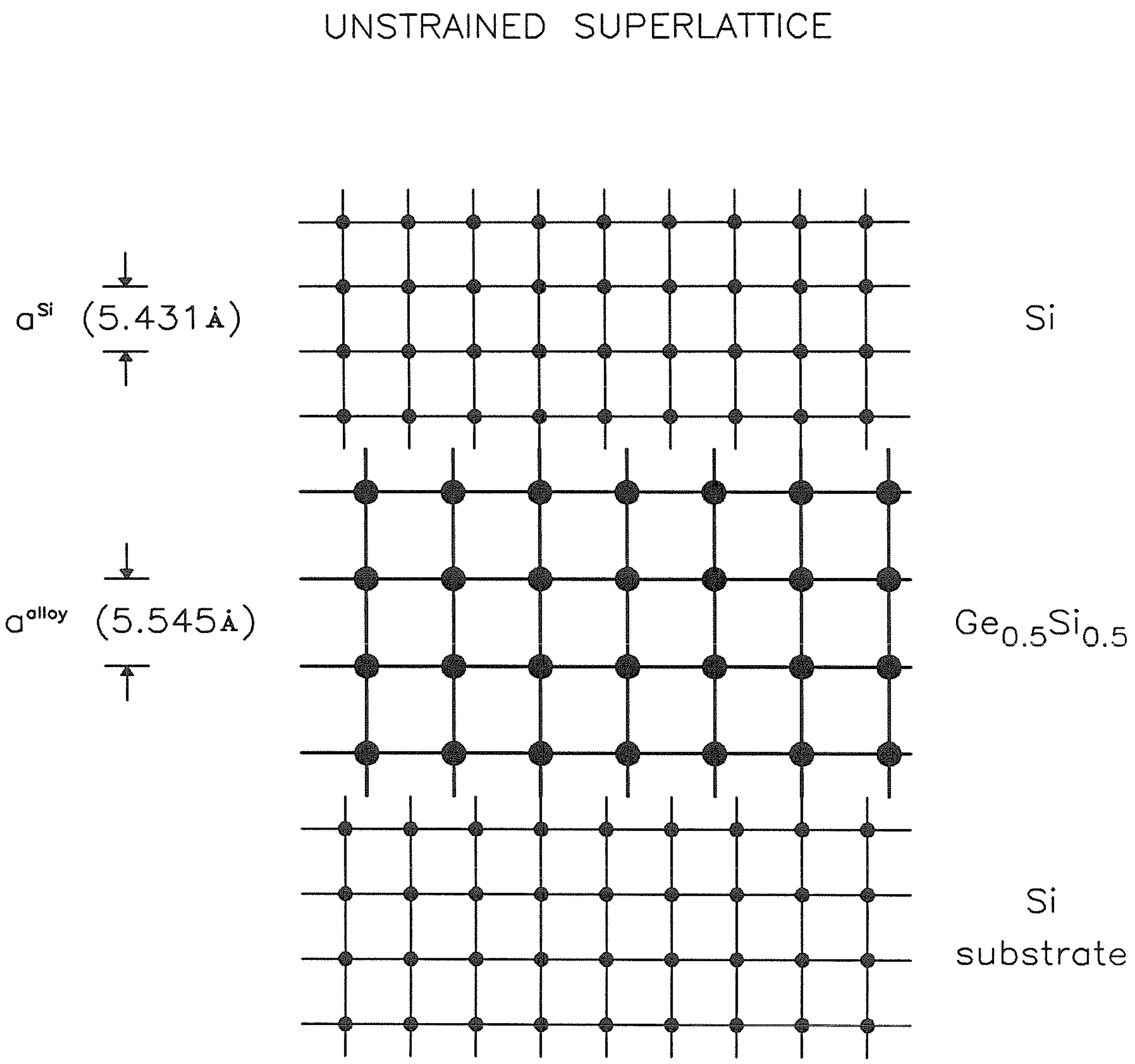

Figure 1.8: Schematic of the arrangement of unit cells in an unstrained superlattice. Lattice mismatch is accommodated by regularly spaced networks of misfit dislocations lying at the interfaces. The difference in bulk cubic lattice constants is exaggerated in the diagram, although the numerical values are correct.

cording to continuum elasticity theory, the areal strain energy E_S of an overlayer constrained to grow on a lattice-mismatched template increases linearly with film thickness,

$$E_S = 2\mu\frac{(1+\nu)}{(1-\nu)}\varepsilon^2 l, \tag{1.4}$$

where μ indicates shear modulus and l indicates film thickness.[37] The areal energy density associated with a network of dislocations sufficiently dense to totally relieve strain is

$$E_D = \left(\frac{2f}{b\sin\beta\cos\gamma}\right)E_d\ , \tag{1.5}$$

where E_d is the energy per unit length of a single misfit dislocation. For a single misfit-accommodating dislocation this energy is

$$E_d = \frac{\mu b^2}{4\pi}\left(\frac{1-\nu\cos^2\beta}{1-\nu}\right)\log\left(\frac{\rho l}{b}\right), \tag{1.6}$$

where ν is Poisson's ratio and ρ determines the radius within the core of the dislocation at which the integration of energy begins (ρ is typically chosen to be 4).[37] Equating the strain-field and misfit-dislocation energy densities yields an implicit equation for critical thickness l_c:

$$f = \frac{b(1-\nu\cos^2\beta)}{4\pi l_c(1+\nu)\sin\beta\cos\gamma}\log\left(\frac{\rho l_c}{b}\right). \tag{1.7}$$

A critical thickness relation based on an early energy-balancing argument[14] is plotted in Fig. 1.9 for Burger's vectors appropriate to Si. Misfit-accommodating dislocations typically found in diamond or zinc blende structures are characterized by {111} slip planes, Burger's vectors of $(a/2) < 110 >$, and dislocation lines along $< 110 >$ directions in an $< 001 >$ interface.[16] In this case, $\gamma = 35.3^\circ$ and $\beta = 60^\circ$ for $< 100 >$-oriented growth. While some data are in agreement with the predictions of this early model,[38,14] many films have been observed to remain coherently strained well beyond this limit.[39]

Attempts to explain the discrepancies between observed and predicted critical thicknesses led to a force balancing argument by Matthews and Blakeslee.[16,17] The stress exerted on a dislocation line at a lattice-mismatched interface is proportional to the thickness of the overlayer,

$$S = 2\mu \cos\lambda \frac{(1+\nu)}{(1-\nu)} b\varepsilon l, \tag{1.8}$$

where λ is the angle between the direction of slip and the line in the interface that is perpendicular to the intersection of the slip plane and the interface. As there is a maximum tension beyond which a dislocation undergoes further slip, a thickness can be derived at which a grown-in threading dislocation will jump discontinuously at a strained interface. For a single thin film this thickness is described by

$$f = \frac{b(1-\nu\cos^2\alpha)}{8\pi\cos\lambda(1+\nu)l_c}\left[\log\left(\frac{l_c}{b}\right)+1\right], \tag{1.9}$$

where α is the angle between the Burger's vector and the dislocation line. This relation has been plotted for $\mathrm{Ge}_x\mathrm{Si}_{1-x}$ in Fig. 1.9. While this theory has seen some agreement with experiment, grown-in threading dislocations are rarely present in sufficient densities to provide significant relaxation of mismatch stresses. Force-balancing arguments have been applied to the nucleation of half loops, but the importance of these dislocations in relieving mismatch stresses remains unclear.[17]

Good agreement with experiment has been achieved with a recent adaptation of the old energy balancing arguments.[39] By terminating the strain field associated with a single dislocation at a radius $w/2$ (independent of misfit, f) and inserting the energy expression for a screw dislocation into the energy-balance equation, one obtains the relationship

$$f^2 = \frac{b^2(1-\nu)}{8\pi w(1+\nu)l_c}\log\left(\frac{l_c}{b}\right). \tag{1.10}$$

Choosing $w = 5b$ yields the plot in Fig. 1.9, which is in excellent agreement with experiment in the $\mathrm{Ge}_x\mathrm{Si}_{1-x}$ system. Unfortunately, the physical basis of this model

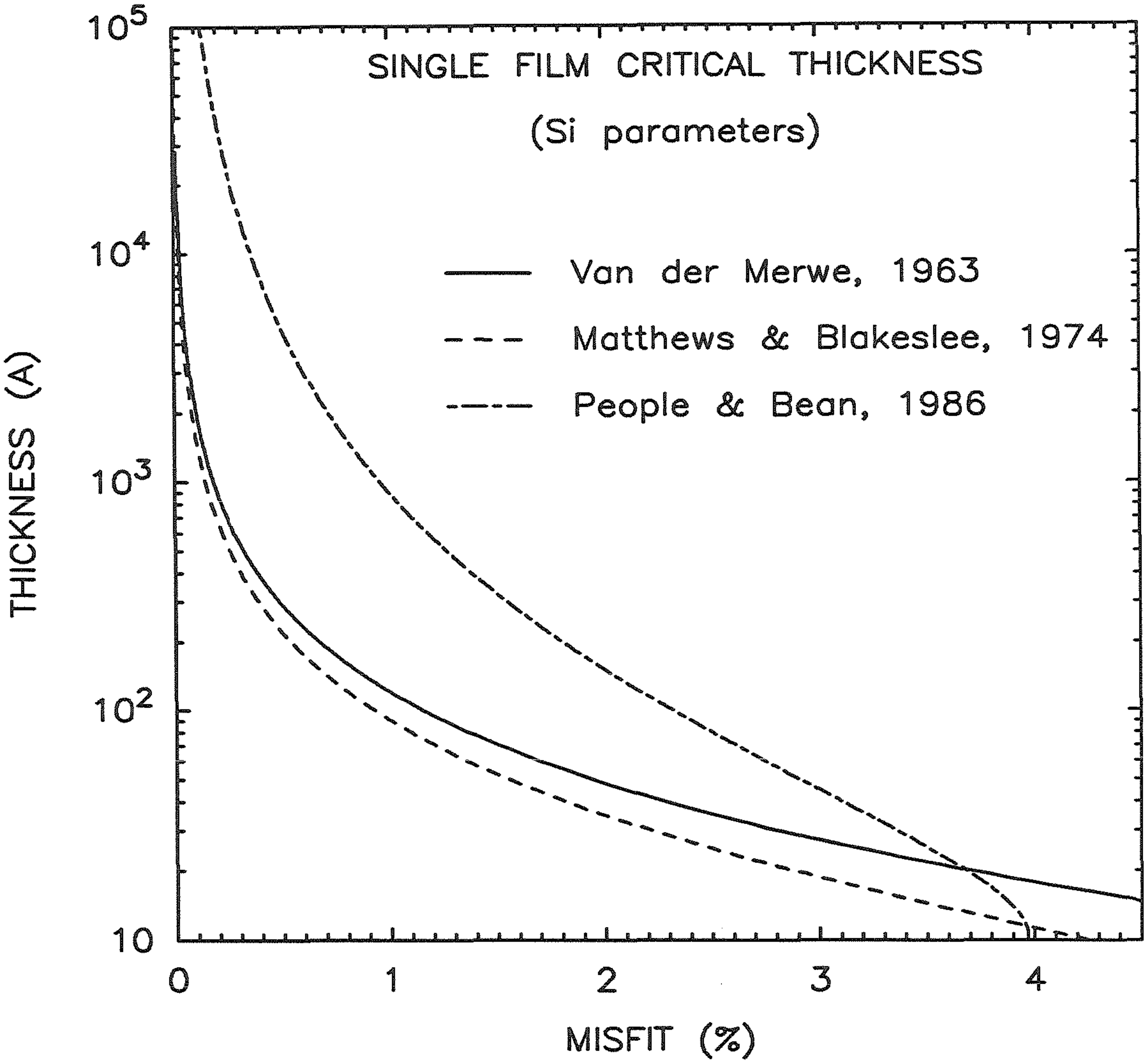

Figure 1.9: Theoretical predictions of critical thickness at which a thin film poorly lattice-matched to a substrate breaks away from that substrate with the formation of misfit dislocations. Calculations assumed dislocations appropriate to < 100 >-oriented growth of Si. The predictions can be extended to many zinc blende semiconductors by scaling thickness with the lattice constant of the material in question. The curve labeled Van der Merwe comes from an energy-balancing relation[14] similar to Eqn. 1.7; Matthews and Blakeslee is from Eqn. 1.9, Ref. 16; and People and Bean is from Eqn. 1.10, Ref. 39.

is doubtful. The validity of terminating the strain field is unclear, as is the assumption that w is independent of misfit. In addition, a screw dislocation corresponds to a lateral displacement of atoms across a half-plane cut, which does not involve the addition or removal of atoms. Thus, unlike an edge-type dislocation, a screw dislocation does not relieve lattice mismatch. TEM studies[35] have confirmed that mismatch-relieving dislocations nucleated at the critical thickness are not screw-type. It is probable that the agreement between this theory and experiment comes primarily from the addition of a free parameter, w, in the problem. Note that neither the original force– nor energy-balancing arguments included such a parameter.

Although each of these theories is concerned with the critical thickness of a single film, there are simple prescriptions for extending the predictions to strained-layer superlattices. The energy-balancing arguments are readily seen to form two criteria: one for the stability of the individual layers, and one for the stability of the superlattice as a whole. The individual layer and overall superlattice strain energies can be thought of as AC and DC components of the strain field in the superlattice;[40] stability of the structure requires that neither component grow too large. The prediction of coherence of the individual layers is identical to that for the single film case. The superlattice as a whole has an elastic strain energy that is approximately equal to that of an alloy of the same overall composition and thickness. Thus, if the equivalent alloy lies beyond the predicted critical thickness, the superlattice should also lie beyond this thickness. It has recently been shown that this can give rise to the configuration depicted in Fig. 1.10,[9,40] in which the superlattice has broken away from the substrate. In this "free-standing" configuration lattice mismatch within the superlattice is accommodated purely by elastic strain, with a large biaxial compression of the Ge_xSi_{1-x} layers converted into lesser expansions and contractions of adjacent Si and Ge_xSi_{1-x} layers.

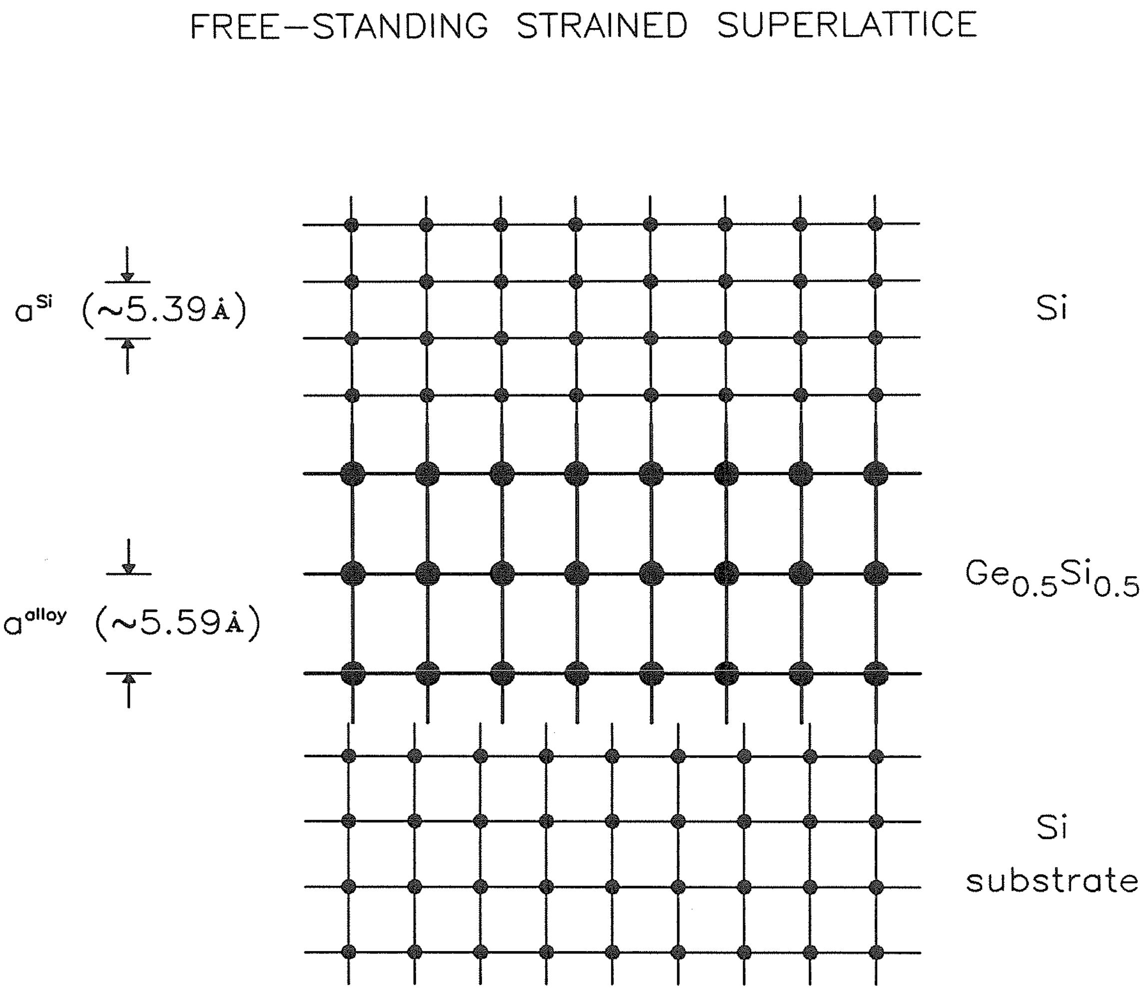

Figure 1.10: Arrangement of unit cells in a free-standing superlattice. A network of dislocations at the superlattice/buffer-layer interface relieves the overall strain between the superlattice and buffer. Lattice-mismatch is accommodated elastically within the superlattice, with strain divided between the layers to minimize the elastic energy of the structure. Tetragonal distortions within the superlattice are exaggerated for clarity, but the numerical lattice constants are correct.

While it should be possible to extend force-balancing arguments similarly for multilayer structures, to date this has been done for only a few cases.[16] It is worth noting that in the case of a multilayer structure the lattice mismatch associated with a given critical thickness is claimed to be *twice* that of the single film case, owing to the creation of two misfit dislocation lines (one each at the top and bottom of a single layer).

Recent experiments have suggested that certain strained-layer structures are metastable and hence are not appropriately described by the classical critical-thickness theories.[41,42,43] It has become clear that the critical thickness displayed by a particular sample is dependent on more than bulk material parameters. Rather than satisfy zero-temperature energy minimization requirements, strained structures have been shown to display activation barriers against the nucleation and glide of dislocations. These barriers enable highly strained layers to be grown far beyond the energy-balancing critical thicknesses.[42] This is the subject of Chapter 4.

1.5 Summary of thesis

1.5.1 Luminescence from CdTe/ZnTe superlattices

Chapter 2 presents a photoluminescence study of CdTe/ZnTe superlattices and a $Cd_xZn_{1-x}Te$ alloy and a comparison of experimentally observed superlattice band gaps with those calculated using $\vec{k} \cdot \vec{p}$ theory. Attempts to observe stimulated emission by optically pumping small cleaved cavities were also made. The work was motivated by several factors. The II-VI semiconductors having large direct band gaps are of technological interest as visible light emitters and detectors. Doping considerations make the CdTe/ZnTe system particularly attractive; high-mobility p-type ZnTe is easily grown, and, unlike many of the II-VI semiconductors, CdTe is readily doped p- and n-type. The enormous lattice mismatch between CdTe and ZnTe ($f = 6\%$) raised questions as to the effects of strain on the optical properties of the superlattice as well as the ability of such a structure to accommodate large stresses.

The results can be summarized as follows. Each of the superlattices emitted visible photoluminescence several orders of magnitude more intense than that from a $Cd_xZn_{1-x}Te$ alloy. Spectra were dominated by a single Gaussian line probably due to an exciton. The choice of topmost buffer layer was not systematically related to photoluminescent intensity or peak position, in contrast to results obtained from systems of smaller lattice mismatch. Energy band gaps calculated using a $\vec{k} \cdot \vec{p}$ model incorporating effects arising from strain were in disagreement with experiment when strain was assumed to be derived from a CdTe buffer layer. Excellent agreement was obtained when it was assumed that the superlattices had broken away from this buffer to adopt a strained configuration that minimized the elastic energy of the superlattice. In view of calculated critical thicknesses, this was proposed as a viable configuration for such a structure. However, these experiments alone were insufficient to establish the free-standing configuration as that of our samples; band gaps calculated under the assumption of entirely unstrained superlattices (*i.e.*, with dislocation networks at every interface in the superlattice) were also in agreement with experiment. Based on the band structure calculations, predictions of transitions between type-I and type-II band alignments were made for coherently strained superlattices. Attempts to obtain stimulated emission from an optically pumped sample have been unsuccessful to date; this is the subject of on-going work.

1.5.2 Structural properties of CdTe/ZnTe superlattices

X-ray diffraction, *in situ* reflection high-energy electron diffraction (RHEED), and TEM studies of CdTe/ZnTe superlattices are the subject of Chapter 3. The purpose of the work was to examine the distribution of elastic strain in a highly lattice-mismatched superlattice. In addition, these samples provided a test of predictions for single-layer critical thicknesses and their extrapolation to superlattices.

It was concluded that each of the samples had been grown beyond the critical thickness for creation of misfit defects. Defect densities were seen to drop dramatically away from the superlattice/buffer-layer interface, however, with structures approaching a free-standing configuration. Substantial free-standing superlattice strains were observed in all but one of the samples. The most highly defective superlattice was below the critical thicknesses predicted for the individual layers and for the superlattice as a whole, unlike a number of more highly strained samples. This result was attributed to slight variations in sample-to-sample growth conditions. The work suggested that the critical thickness of a particular sample is dependent on the thermal history of the sample, in addition to the material system and lattice mismatch.

1.5.3 Dislocation formation in $Ge_{0.5}Si_{0.5}$/Si superlattices

Chapter 4 presents a study of dislocation formation in $Ge_{0.5}Si_{0.5}$/Si superlattices by channeled Rutherford Backscattering Spectroscopy (RBS), x-ray diffraction, *in situ* RHEED, and cross-sectional and plan-view TEM. The dependence of dislocation formation on growth temperature was examined to investigate the equilibrium assumptions behind the critical thickness theories and to try to account for discrepancies in critical thicknesses reported in the literature. Ge/Si structures are particularly well suited to this study as they are readily grown over a wide range of temperatures (approximately 300 °C to 850 °C for single-crystal growth). Accommodation of lattice mismatch in this system is of particular interest as the success of proposed Ge_xSi_{1-x} HBT's and light emitters and modulators will in part be dependent upon maintaining high levels of coherent strain.

The density of misfit-accommodating dislocations was found to be strongly dependent on growth temperature. Dislocation densities dropped from $1.5 \times 10^5 \mathrm{cm}^{-1}$ at a growth temperature of 530 °C to $< 10^5 \mathrm{cm}^{-2}$ at 365 °C. Dislocation networks were most dense near the superlattice/buffer-layer interface; several structures adopted an almost defect-free configuration near the free-standing limit. The results have been taken as evidence of an activation barrier against the nucleation or glide of dislocations. While the equilibrium critical thickness of a sample may still be regarded as dependent only on bulk material properties, the appearance of misfit defects in a particular sample is clearly dependent on thermodynamic factors which may effectively freeze a sample in a highly strained, metastable state. Our data are in support of a plastic-flow model of defect formation currently being developed.[44]

References

1. G. C. Osbourn, *Phys. Rev. B* **27**, 5126 (1983).
2. L. Esaki and R. Tsu, *IBM J. Res. Develop.* **14**, 61 (1970).
3. S. R. Hetzler, Ph.D. Thesis, California Institute of Technology, 1986.
4. G. H. Döhler, *Physica Scripta* **24**, 430 (1981).
5. S. R. Kurtz, G. C. Osbourn, R. M. Biefeld, L. R. Dawson, and H. J. Stein, *Appl. Phys. Lett.* **52**, 831 (1988).
6. G. Bastard, *Phys. Rev. B* **24**, 5693 (1981).
7. T. C. McGill, R. H. Miles, and G. Y. Wu, *Mater. Res. Soc. Symp. Proc.* **90**, 143 (1987).
8. R. H. Miles, G. Y. Wu, T. C. McGill, J. P. Faurie, and S. Sivananthan, *Appl. Phys. Lett.* **48**, 1383 (1986).
9. R. H. Miles, T. C. McGill, S. Sivananthan, X. Chu, and J. P. Faurie, *J. Vac. Sci. Technol. B* **5**, 1263 (1987).
10. H. Jung, A. Fischer, and K. Ploog, *Appl. Phys. A* **33**, 97 (1984).
11. P. M. Petroff, C. Weisbuch, R. Dingle, A. C. Gossard, and W. Wiegmann, *J. Vac. Sci. Technol.* **19**, 571 (1981).

12. R. N. Bicknell, N. C. Giles-Taylor, D. K. Blanks, R. W. Yanka, E. L. Buckland, and J. F. Schetzina, *J. Vac. Sci. Technol. B* **3**, 709 (1985).

13. D. L. Smith, private communication.

14. J. H. Van der Merwe, *J. Appl. Phys.* **34**, 123 (1963).

15. C. A. B. Ball and J. H. Van der Merwe, in *Dislocations in Solids, Volume 6*, edited by F. R. N. Nabarro (North Holland, Amsterdam, 1983), p. 122.

16. J. W. Matthews and A. E. Blakeslee, *J. Cryst. Growth* **27** 118 (1974); **29** 273 (1975); **32** 265 (1976).

17. J. W. Matthews, in *Epitaxial Growth, Part B*, edited by J. W. Matthews (Academic, New York, 1968).

18. S. M. Sze, *Physics of Semiconductor Devices* (Wiley, New York, 1981).

19. W. L. Roth, in *Physics and Chemistry of II-VI Compounds*, edited by M. Aven and J. S. Prener (Wiley, New York, 1967), p. 119.

20. S. S. Devlin, in *Physics and Chemistry of II-VI Compounds*, edited by M. Aven and J. S. Prener (Wiley, New York, 1967), p. 551.

21. G. D. Studtmann, R. L. Gunshor, L. A. Kolodziejski, M. R. Melloch, J. A. Cooper, Jr., R. F. Pierret, D. P. Munich, C. Choi, and N. Otsuka, *Appl. Phys. Lett.* **52**, 1249 (1988).

22. P. Voisin, *Surf. Sci.* **168**, 546 (1986).

23. P. L. Gourley, T. J. Drummond, and B. L. Doyle, *Appl. Phys. Lett.* **49**, 1101 (1986).

24. J. I. Pankove, *Optical Processes in Semiconductors* (Dover, New York, 1975).

25. G. L. Bir and G. E. Pikus, *Symmetry and Strain-Induced Effects in Semiconductors* (Keter, Jerusalem, 1974).

26. D. L. Camphausen, G. A. N. Connell, and W. Paul, *Phys. Rev. Lett.* **26**, 184 (1971).

27. C. G. Van de Walle and R. M. Martin, *Phys. Rev. B* **35**, 8154 (1987).

28. A. A. Kaplyanskii and L. G. Suslina, *Soviet Physics - Solid State* **7**, 1881 (1966).

29. D. G. Thomas, *J. Appl. Phys. Suppl.* **32**, 2298 (1961).

30. D. W. Langer, R. N. Euwema, K. Era, and T. Koda, *Phys. Rev. B* **2**, 4005 (1970).

31. A. Gavini and M. Cardona, *Phys. Rev. B* **1**, 627 (1970).

32. Y. Rajakarunanayake, R. H. Miles, G. Y. Wu, and T. C. McGill, *Phys. Rev. B*, to be published.

33. S. Froyen, D. M. Wood, and A. Zunger, *Proc. Mater. Res. Soc.*, to be published.

34. J. N. Schulman and Y.-C. Chang, *Phys. Rev. B* **24**, 4445 (1981).

35. P. M. Petroff, in *Semiconductors and Semimetals, Vol. 22, Part A*, edited by W. T. Tsang (Academic, Orlando, 1985).

36. T. Tatsumi, H. Hirayama, and N. Aizaki, *Appl. Phys. Lett.* **52**, 895 (1988).

37. F. R. N. Nabarro, *Theory of Crystal Dislocations* (Dover, New York, 1987).

38. G. J. Whaley and P. I. Cohen, *J. Vac. Sci. Technol.* B, to be published.

39. R. People and J. C. Bean, *Appl. Phys. Lett.* **47**, 322 (1985); **49**, 229(E) (1986).

40. R. Hull, J. C. Bean, F. Cerdeira, A. T. Fiory, and J. M. Gibson, *Appl. Phys. Lett.* **48**, 56 (1986).

41. A. T. Fiory, J. C. Bean, R. Hull, and S. Nakahara, *Phys. Rev. B* **31**, 4063 (1985).

42. R. H. Miles, P. P. Chow, D. C. Johnson, R. J. Hauenstein, C. W. Nieh, M. D. Strathman, and T. C. McGill, *Appl. Phys. Lett.* **52**, 916 (1988).

43. B. W. Dodson, J. Y. Tsao, and P. A. Taylor, *Proceedings of the Third International Conference on Superlattices, Microstructures, and Microdevices*, to be published.

44. B. W. Dodson and J. Y. Tsao, *Appl. Phys. Lett.* **51**, 1325 (1987).

Chapter 2

Luminescence from CdTe/ZnTe Superlattices

2.1 Introduction

2.1.1 Background

The wide band gap II-VI semiconductors have attracted attention for some time as possible visible light emitters or detectors.[1] With direct band gaps ranging from 3300 Å to 7800 Å, the II-VI's span the visible region of the spectrum. However, the introduction of these materials within devices has been hindered by difficulties associated with doping, primarily because of autocompensation during growth and processing. In addition, the band-gap tunability offered by ternary alloys has been difficult to realize experimentally, as the material is often of poor uniformity and structural quality.[2] Each of these problems may now be surmountable with recent developments in II-VI molecular-beam epitaxy (MBE) and metalorganic chemical vapor deposition (MOCVD).

While the problem of doping II-VI thin films is beginning to be reassessed,*

---

*Results such as the recent demonstration of 9×10^{17} p-type ZnSe are particularly noteworthy.[3]

doping was not a major concern in this study. The ease with which CdTe is doped p- or n-type has brought attention to $Cd_xZn_{1-x}Te$ for application in p-n structures for some time. The near-band-gap emission of such a device would be in the green to deep-red portion of the spectrum; CdTe has a band gap of 1.60eV (7750 Å) at 4K, and ZnTe has a gap of 2.38eV (5210 Å) at this temperature.

The structural quality and uniformity of ternary II-VI alloys have been demonstrated to be serious problems in both CVD- and MBE-grown films. $Cd_xZn_{1-x}Te$ in particular has been shown to phase-separate for many alloy compositions.[4] Although avoiding the problems intrinsic to alloys, superlattices consisting of layers of CdTe alternating with layers of ZnTe present additional problems associated with the large lattice mismatch between the two materials. CdTe has a bulk lattice constant of 6.481 Å, while that of ZnTe is 6.104 Å, resulting in a 6% mismatch. The manner in which this mismatch is accommodated was of interest in this study, as was the effect on the optical properties of the strain field and/or dislocations arising from this mismatch.

The CdTe/ZnTe superlattices examined here were the first wide band gap II-VI superlattices studied. More recent work has demonstrated the successful growth and excellent optical properties of ZnS/ZnSe[5] and ZnSe/ZnTe[6] superlattices. Our study was also one of the first in a system with a large lattice mismatch. Although several highly strained III-V structures had been examined prior to this CdTe/ZnTe work (notably in the $In_xGa_{1-x}As$ system[7]), it was unclear that the effects of strain and dislocations on the optical properties would be similar.

2.1.2 Results of this work

Photoluminescence from CdTe/ZnTe superlattices has been observed for the first time. Superlattices with individual CdTe and ZnTe layer thicknesses between approximately 20 Å and 50 Å have been compared with a $Cd_{0.37}Zn_{0.63}Te$ alloy. Each of the superlattices displays intense, visible luminescence at substantially lower energies than expected from corresponding $Cd_xZn_{1-x}Te$ alloys. Temperature and pump-power dependences suggest that the dominant luminescent peaks are due to excitonic recombinations. Experimental gaps based on this identification have been compared with gaps calculated by a second-order $\vec{k} \cdot \vec{p}$ model including effects that are due to strain. These calculations show that superlattices grown on CdTe buffer layers are not strained according to the template set by this topmost buffer. Calculated band gaps are in excellent agreement with experiment when the strain distribution is assumed to conform to a minimum elastic-strain-energy condition within the superlattice (*i.e.*, a *free-standing* configuration). This configuration is argued to be stable for these superlattices, based on classical critical-thickness calculations, and is shown to be plausible based on the slow relaxation of stresses once the critical thickness for nucleation of misfit defects is exceeded. Conversely, strains set by topmost CdTe or ZnTe buffer layers are shown to lie far beyond the accepted limits to defect-free growth for superlattice thicknesses comparable to ours. Calculated gaps are also shown to be in good agreement with experiment when strain effects are neglected. The unstrained configuration is unlikely, however, since the densities of dislocations necessary to reduce strains substantially should open strong non-radiative decay channels, a result that is inconsistent with the intense luminescence observed. Although the nearly free-standing nature of the strain field in these superlattices has subsequently been verified by the structural characterizations described in Chapter 3, the two cases of free-standing and unstrained growth could not be distinguished solely on the basis of band gaps.

Based on the agreement between theory and experiment, band gaps have been calculated for a grid of CdTe/ZnTe superlattices for the two cases of free-standing strained growth and unstrained growth. Strain that is due to lattice mismatch is shown to have a dramatic effect on the band-edge positions and on the energies of the superlattice ground states. Transitions between type-I and type-II band alignments are predicted based on these calculations.

Attempts to observe laser oscillation in a cleaved CdTe/ZnTe superlattice cavity have proven unsuccessful to date. However, $Cd_{0.25}Zn_{0.75}Te$/ZnTe superlattices have been recently reported to lase.[8]

2.1.3 Outline of chapter

The samples examined in this study are described in Section 2.2. A study of the photoluminescence spectra from these samples is presented in Section 2.3. Luminescent intensities and peak positions of the superlattices and alloy are compared, and the primary peaks are identified to establish approximate values of the sample band gaps. Section 2.4 describes calculations of the electronic band structure of CdTe/ZnTe superlattices. Two- and eight-band $\vec{k} \cdot \vec{p}$ models are briefly outlined, as is the incorporation of strain within these models. Experimental gaps are compared with those calculated assuming a variety of strains. Critical thickness arguments are used to argue for the free-standing configuration, which is found to give the best agreement between theory and experiment. Results of band-gap calculations for a grid of superlattices are also presented. Section 2.5 describes attempts to observe lasing in a CdTe/ZnTe structure. The conclusions are summarized in Section 2.6.

2.2 Samples

The $Cd_xZn_{1-x}Te$ samples used in this study were grown in a Riber 2300 MBE machine. Each superlattice was grown on buffer layers deposited upon a (100)-oriented GaAs substrate. Although $Cd_xZn_{1-x}Te$ sometimes adopts a (111) orientation on (100) GaAs,[9] the initial buffer layers used in this study were chosen to establish (100) epitaxy. Topmost buffers were either CdTe, ZnTe or a $Cd_xZn_{1-x}Te$

alloy. The superlattices were grown at approximately 180 °C. Individual CdTe and ZnTe layers within the superlattices ranged in thickness between approximately 20 Å and 50 Å, as indicated in Table 2.1. Superlattices consisted of several hundred repeats; total superlattice thicknesses were roughly a micron. The buffer layers for samples 4 and 8 were grown directly on GaAs substrates. Samples 1, 2, and 3 were each grown on step-graded $Cd_xZn_{1-x}Te$ buffer layers, starting with ZnTe on a (100) GaAs substrate and increasing Cd content in discrete increments as growth proceeded. The $Cd_xZn_{1-x}Te$ buffer layer of sample 6 was grown on a 30 Å/30 Å CdTe/ZnTe superlattice, whereas that of sample 7 was grown on three superlattices of increasing Cd content.

Superlattice compositions and layer thicknesses were determined by a variety of means. *In situ* growth-monitoring techniques were of limited use in determining sample characteristics as these were amongst the first such films grown. The average thickness of individual superlattice periods was determined by x-ray diffraction (see Section 3.2.1). Relative ratios of Cd to Zn were determined for each sample through energy dispersive spectroscopy (EDS). This was a source of potential error, however, as the volume sampled by this technique is comparable in depth to the thickness of the superlattices. Signal from the substrate was minimized by reducing the energy of the impinging electron beam and by tilting the sample with respect to this beam. The accuracy of the compositions determined by EDS was checked by analyzing x-ray diffraction spectra from intentionally alloyed pieces of samples 2, 3, and 4. Compositions determined by applying Vegard's Law (*i.e.*, linear change of alloy lattice constant with composition) to these data are in reasonable agreement with results derived from EDS.

CdTe and ZnTe layer thicknesses quoted in Table 2.1 were calculated from the measured superlattice compositions and periodicities based on the assumption of negligible interdiffusion. Layer thicknesses determined by TEM for sample 8 are

Table 2.1: CdTe/ZnTe superlattice samples.

Sample	Superlattice CdTe/ZnTe (Å)	Periods	Top buffer	(Reference No.)
1	26/32	200	CdTe	(199 35)
2	31/23	200	CdTe	(197 33)
3	56/50	150	CdTe	(194 32)
4	27/30	200	ZnTe	(198 34)
5	24/30	200	$Cd_{0.5}Zn_{0.5}Te$	(201 36)
6	27/30	200	$Cd_{0.5}Zn_{0.5}Te$	(206 40)
7	35/32	200	$Cd_{0.5}Zn_{0.5}Te$	(207 41)
8	21/20	400	$Cd_{0.5}Zn_{0.5}Te$	(120 17)
9	29/35	250	$Cd_{0.5}Zn_{0.5}Te$	(122 18)

in agreement with the calculated values. The assumption of minimal interdiffusion is borne out by photoluminescence and TEM data from these samples, but this is not true of all CdTe/ZnTe superlattices; interdiffusion has been shown to be significant in this system at higher growth temperatures.[10]

A $Cd_{0.37}Zn_{0.63}Te$ sample was grown for comparison with the superlattices. Composition of the film was determined by EDS and has been confirmed by photoluminescence. The alloy was grown to a thickness of 4.1 μm on a (100)-oriented GaAs substrate.

2.3 Photoluminescence

2.3.1 Theory

Light resulting from the radiative decay of an electron-hole pair subsequent to optical excitation is referred to as photoluminescence. Analysis of this luminescence can yield a variety of information pertaining to the static and dynamic electronic properties of a material. Photoluminescence is usually a nondestructive experiment, and as a consequence it has become popular to parlay spectra into a variety of diagnostic information (pertaining to alloy compositions, impurity concentrations, or strain distributions, for example).

A typical photoluminescence process is depicted schematically in Fig. 2.1. An incoming photon with an energy exceeding the band gap of the material is absorbed to create an excited electron-hole pair. In an indirect-gap material this process can require the emission or absorption of a phonon, but in direct-gap semiconductors such as CdTe and ZnTe the dominant process is absorption without the involvement of phonons. For the purposes of the experiments described here, the electrons and holes can be described as dropping rapidly to the band extrema through the emission of phonons. This process usually takes place on a subnanosecond time scale.[11] In reality, the dynamics of this process can be quite complicated, with electron-electron interactions bringing the carriers into a quasi-thermal distribution on a 100psec time scale. This distribution may couple only weakly to the lattice, with the phonon temperature reaching equilibrium with that of the carriers on a somewhat longer time scale. Carriers relaxing to the conduction and valence band extrema may recombine radiatively, giving up a photon of energy approximately equal to the band gap E_g of the material, or may form bound electron-hole pairs (excitons) with ground-state binding energies on the order of several meV ($E_{\mathrm{ex}} = m_r^* e^4/2h^2\epsilon^2$, where $1/m_r^* = 1/m_e^* + 1/m_h^*$ for electron and hole effective masses m_e^*

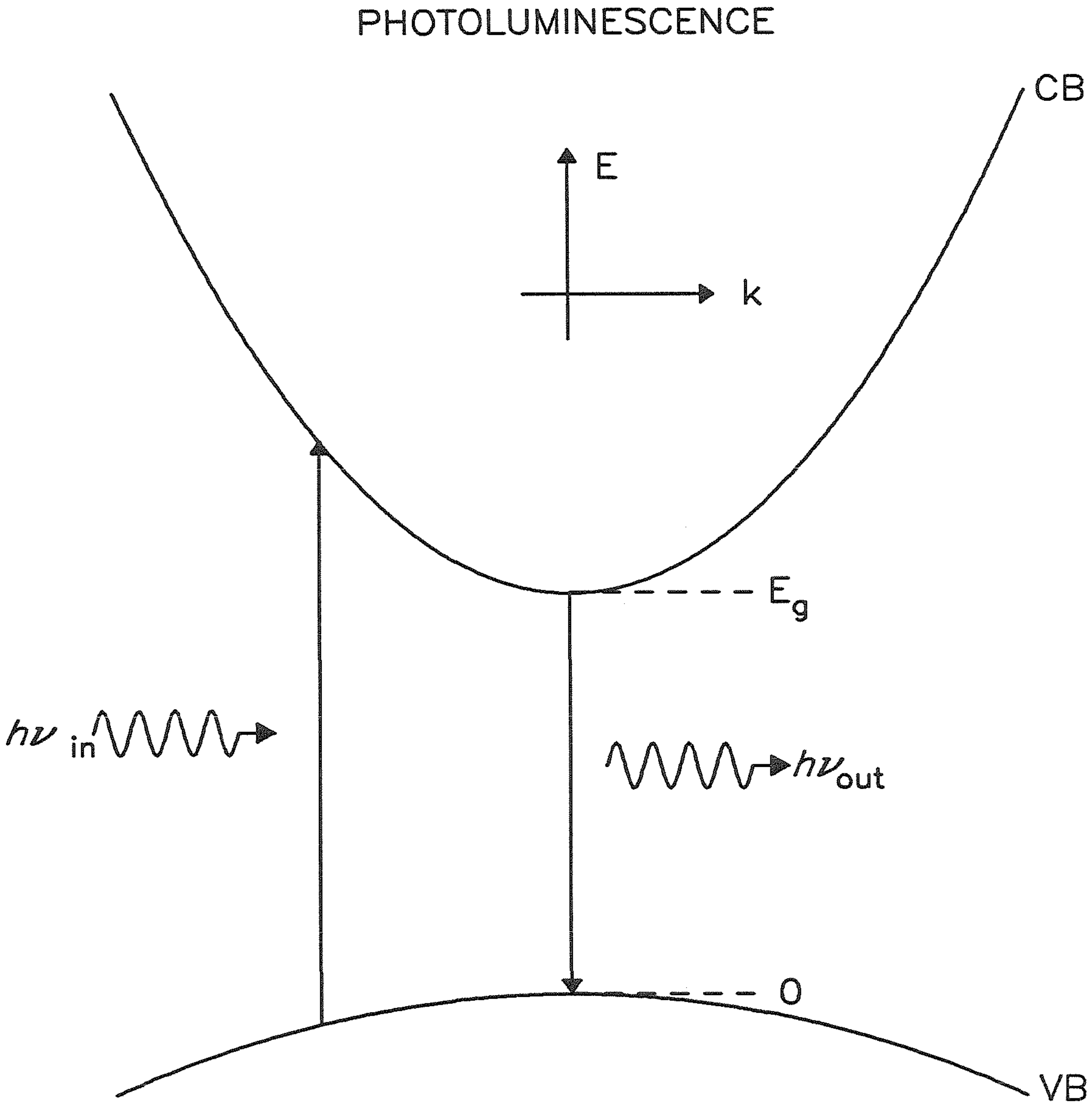

Figure 2.1: A typical photoluminescence process, with absorption of a photon with energy $\hbar\omega_{\rm in}$ and emission of a photon with energy close to the band gap of the semiconductor $\hbar\omega_{\rm out} \simeq E_g$. The case illustrated is for a direct-gap semiconductor, in which the valence and conduction band extrema lie at the same point in $\vec{k}$-space. Momentum conservation requires emission or absorption of a phonon for recombination near an indirect band gap.

and m_h^*, respectively).[12] Subsequent radiative decay of these excitons occurs at an energy $E_{\text{out}} \simeq E_g - E_{\text{ex}}$. The ratio of band-to-band versus excitonic luminescence is strongly dependent upon the binding energy of the exciton and the temperature of the sample.

Effects such as nonradiative recombinations and radiative decays associated with impurities or defects greatly complicate the nature of the luminescence from many samples. Impurities introduce electronic levels at well-defined energies within a material, with the result that the energy of band-to-impurity recombinations can yield information pertaining to the doping of a particular sample. Nonradiative decays are by nature less difficult to isolate, but are known to result from surfaces or structural defects in addition to higher-order scattering (Auger or multiphonon) events.

Luminescence features can often be identified by observing the temperature and pump-power dependences of the lines or by time-resolved techniques. The decay of a particular line with increasing temperature gives an approximate measure of the binding energy of that feature. Extrinsic lines can often be distinguished from intrinsic by the power levels at which the features saturate. In addition, excitonic or band-to-band features display different power dependences from impurity-to-band lines, which in turn differ from lines associated with impurity-to-impurity transitions. In practice, the impurity associated with a particular line is usually identified by intentionally changing the concentration of various impurities from sample to sample.[13] There are, however, methods such as selective excitation luminescence which can yield excited state information unique to a particular impurity.[14]

Numerous schemes have been employed to spatially resolve photoluminescence across the surface of a wafer and as a function of depth. The absorption of light within a semiconductor is governed by the joint density of states separated by the energy of the incoming photon $\hbar\omega$, weighted by an occupation factor and a probability associated with the transition. For the case of a direct-gap semiconductor in which the probability of valence-to-conduction-band transitions is largely independent of $\vec{k}$, the absorption coefficient is

$$\alpha = A^*(\hbar\omega - E_g)^{\frac{1}{2}}; \qquad A^* \simeq \frac{e^2}{nch^2 m_e^*}\left(2\frac{m_h^* m_e^*}{m_h^* + m_e^*}\right)^{\frac{3}{2}}, \tag{2.1}$$

where E_g is the energy gap of the semiconductor and n is the index of refraction. This dependence on the energy of the incoming light means that by changing the wavelength of the exciting beam it is possible to probe different regions in a sample. This technique is particularly useful in direct-gap semiconductors, as MBE-grown film thicknesses are of approximately the same magnitude as typical absorption lengths (roughly $1\,\mu$m). Networks of structural defects have been isolated using this technique.[15]

2.3.2 Experimental setup

The photoluminescence setup used in these experiments is depicted in Fig. 2.2. Optical excitation of the samples was provided by a Coherent CR-3000K krypton laser and a Coherent Innova 20 argon ion laser. Kr violet lines at 4131 Å and 4154 Å and an Ar green line at 5145 Å were chosen to pump the samples at energies greater than the band gaps. The lasers were operated in a continuous wave (cw) mode with typical power levels of 1mW, obtained by lowering the current through the laser tube and by attenuating the output beam with neutral density filters. A Spex Lasermate was sometimes used between the laser and sample to monochromate the beam. Notch filters reduced background noise that was due to plasma lines when the Lasermate was not in place. The beam was focused to a spot roughly 1mm^2 in area at the sample. Samples were cooled to temperatures between $2 - 77$K in a Janis Model DT-8 liquid He immersion dewar.

Luminescence from the samples was focused by collection optics onto the front

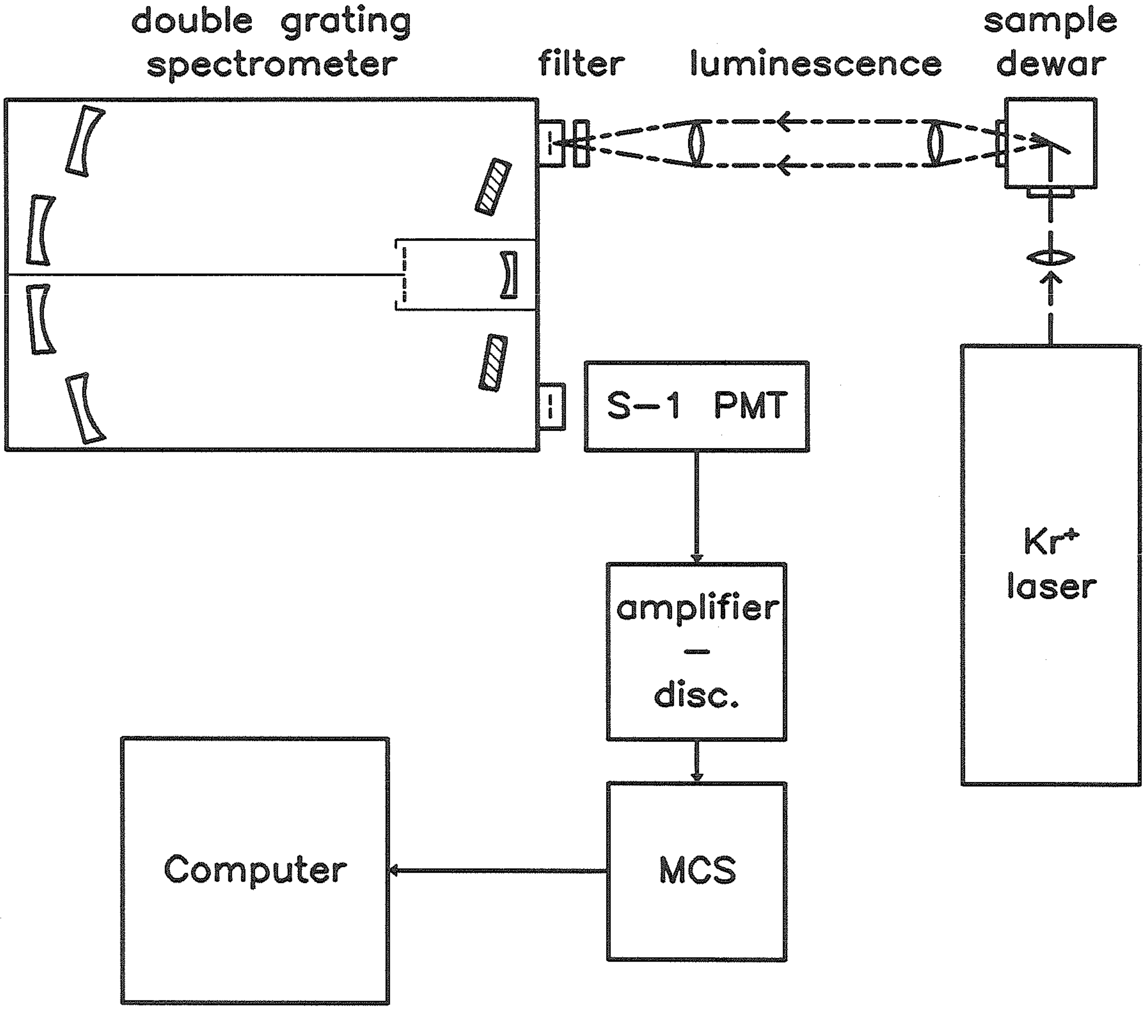

Figure 2.2: Schematic of the apparatus used in the photoluminescence experiments. Adapted from Ref. 16.

slit of a Spex 1404 double-grating spectrometer. Gratings blazed at 1.6 μm were used in second order to maximize spectrometer throughput around 8000 Å. Cutoff filters were placed in front of the spectrometer to attenuate light out of the spectral range of interest (if allowed to pass through a grating spectrometer, this light can diffract in a different order and appear superimposed upon the spectra under study). Luminescence passing through the spectrometer was detected by an S-1 photomultiplier tube (PMT) cooled to 77K. Signal from the PMT was amplified, passed through a discriminator, and triggered a time-to-pulse-height converter, which outputs uniform pulses. The length of these pulses (5 μsec) inserted a dead time into the system, which limited useful count rates to less than 100kHz. (The PMT recovery time of $\simeq$ 30nsec was not a limiting factor.) Pulses were binned by a multichannel scaler (MCS). Data were subsequently transferred to computers for analysis.

2.3.3 Results

Typical CdTe/ZnTe superlattice luminescence is compared with that from a $Cd_{0.37}Zn_{0.63}Te$ alloy sample in Fig. 2.3. The alloy luminescence is characterized by a weak, broad feature with a high-energy cutoff of 2.02eV at 5K. The observed luminescence is in excellent agreement with that obtained in previous $Cd_xZn_{1-x}Te$ alloy studies,[17] and is approximately two orders of magnitude less intense than that from the superlattices under the pump conditions described here. Photoluminescence from the superlattices is dominated by intense lines at the high-energy end of the spectrum. Sample 3 displays two such peaks and sample 8 displays four. All other superlattices display a single peak. The full width at half maximum of these intense peaks varies between $20-30$meV from sample to sample. Additional luminescence is observed in each sample at lower energies and substantially lower intensities than the primary lines. Luminescence at the primary peaks increases

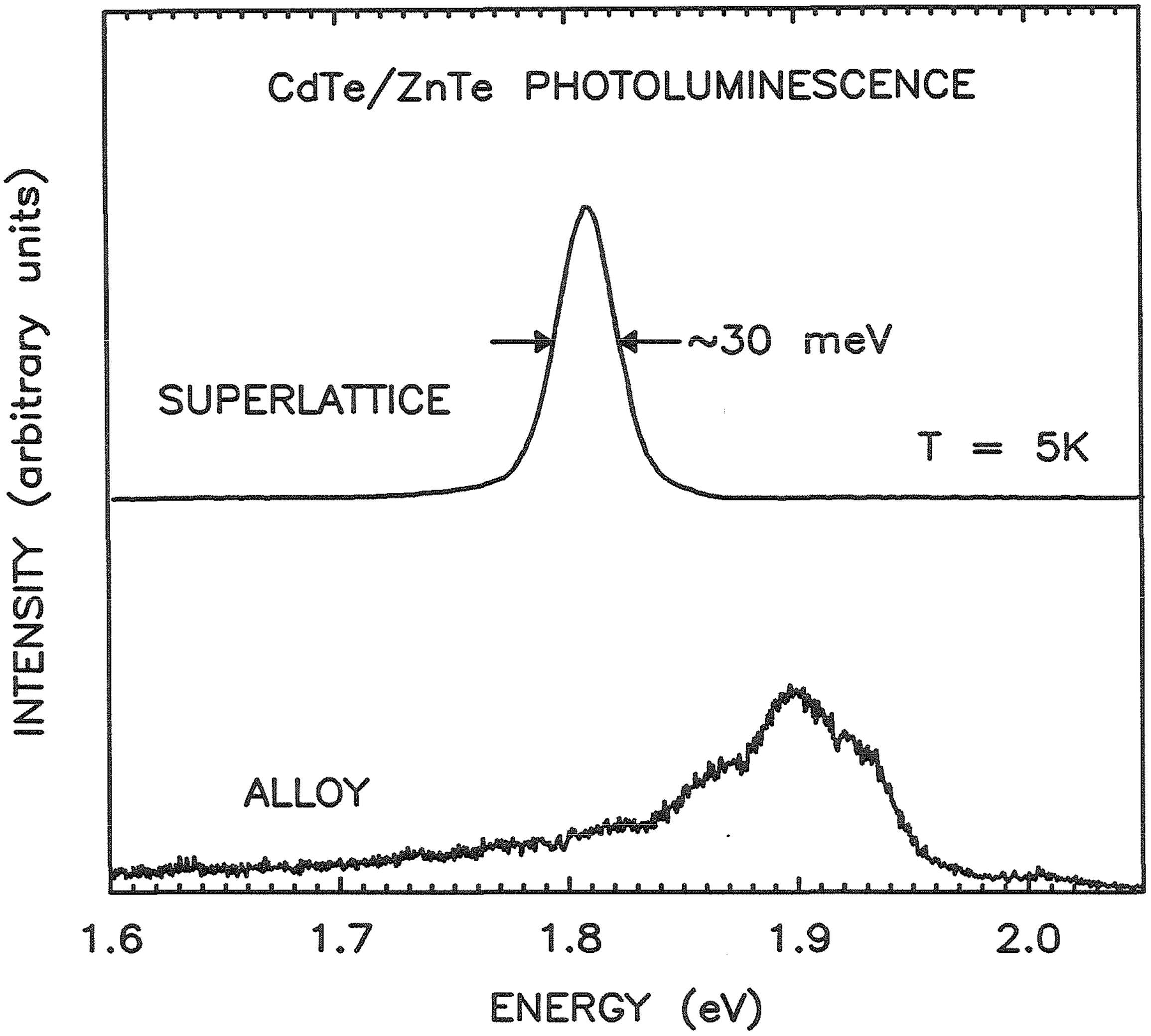

Figure 2.3: Photoluminescence spectra for CdTe/ZnTe superlattice sample 2 and a $Cd_{0.37}Zn_{0.63}Te$ alloy at 5K. Luminescent intensity is plotted against emitted photon energy. Spectra are plotted on different vertical scales.

superlinearly with pump power at a rate greater than that of the lower energy lines.

The intense luminescence features observed from the superlattices appear to be associated with excitonic recombinations. The absence of any appreciable luminescence at energies greater than the cutoff suggests that the observed line is very near the sample band gap. Both the superlinear power dependences of the lines and the absence of noticeable saturation at the pump powers used here suggest that the lines are not associated with impurities. The lines decay rapidly with increasing temperature; typical luminescent intensities at 30K are down by a factor of 2-3 from the 5K intensity, and at 65K the features have almost disappeared. This temperature dependence is consistent with a weakly bound feature, and would not usually be expected for band-to-band luminescence, which typically becomes more prominent as previously bound carriers are thermally excited into the bands. As shown in Fig. 2.4, the lines are fit by Gaussians. This line shape is suggestive of a random variation within the samples, in this case in layer thickness. Note that the line shape cannot be used to argue for excitonic versus band-to-band luminescence, as self-absorption should not play a major role in determining the line shape near the band edges over energies of a few tens of meV. The inset of Fig. 2.4 compares the Gaussian fit to the luminescence line to that expected from band-to-band recombinations across the same Gaussian distribution of band gaps, assuming self-absorption calculated from Eqn. 2.1. The inset shows almost identical spectra with and without self-absorption from the band edges; line shape cannot be used to distinguish above- and below-band-gap luminescence in this case.

Two of the superlattices display several intense lines. Luminescence from sample 8 is characterized by four such lines, and sample 3 by two. The temperature dependence of the photoluminescence from sample 8 is shown in Fig. 2.5. The scans shown in this figure were taken under identical pump conditions. Spectra taken at

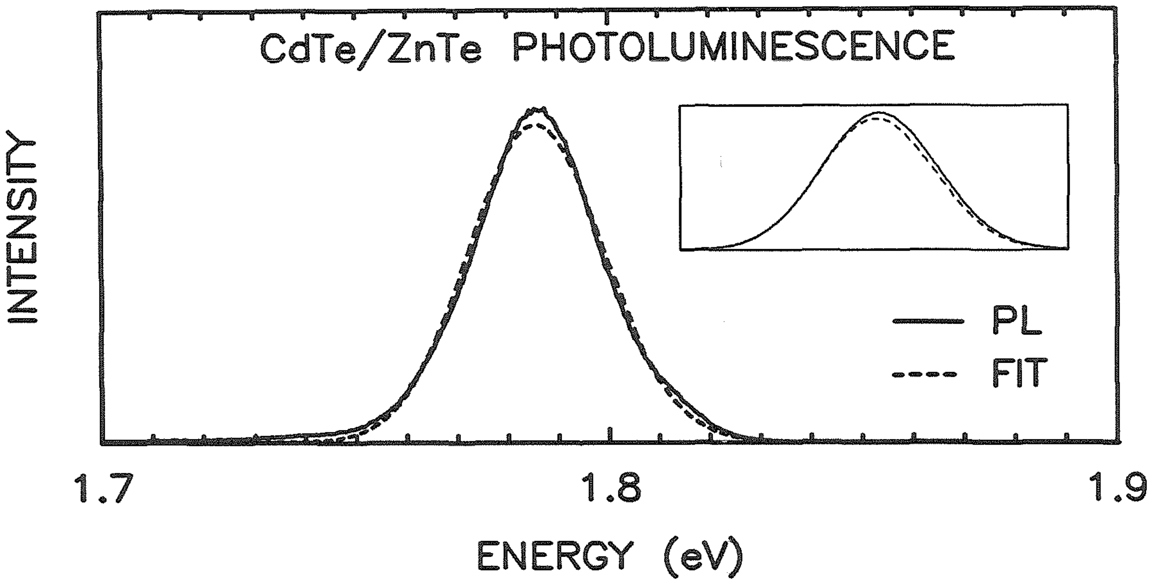

Figure 2.4: Intense photoluminescence line from CdTe/ZnTe superlattice sample 5. The line shape is nearly Gaussian, probably resulting from a random variation within the sample (in layer thickness, in this case). The inset compares the fit with that calculated from a Gaussian distribution of band-to-band recombinations, including effects that are due to self-absorption. The line shapes are almost identical; the luminescence cannot be positively identified as band-to-band or excitonic simply on the basis of line shape.

20K, 35K, and 50K come from the same part of the sample; the 5K luminescence comes from an area just to the side of that probed in the other scans. Luminescence below 1.7eV is seen to be almost independent of temperature. These features can be related to an underlying $Cd_{0.5}Zn_{0.5}Te$ buffer layer. Features at higher energies show strong temperature dependences and appear to be coming from the superlattice. The intensities of these lines show nearly identical superlinear dependences on incident pump power. The similarity of the temperature and

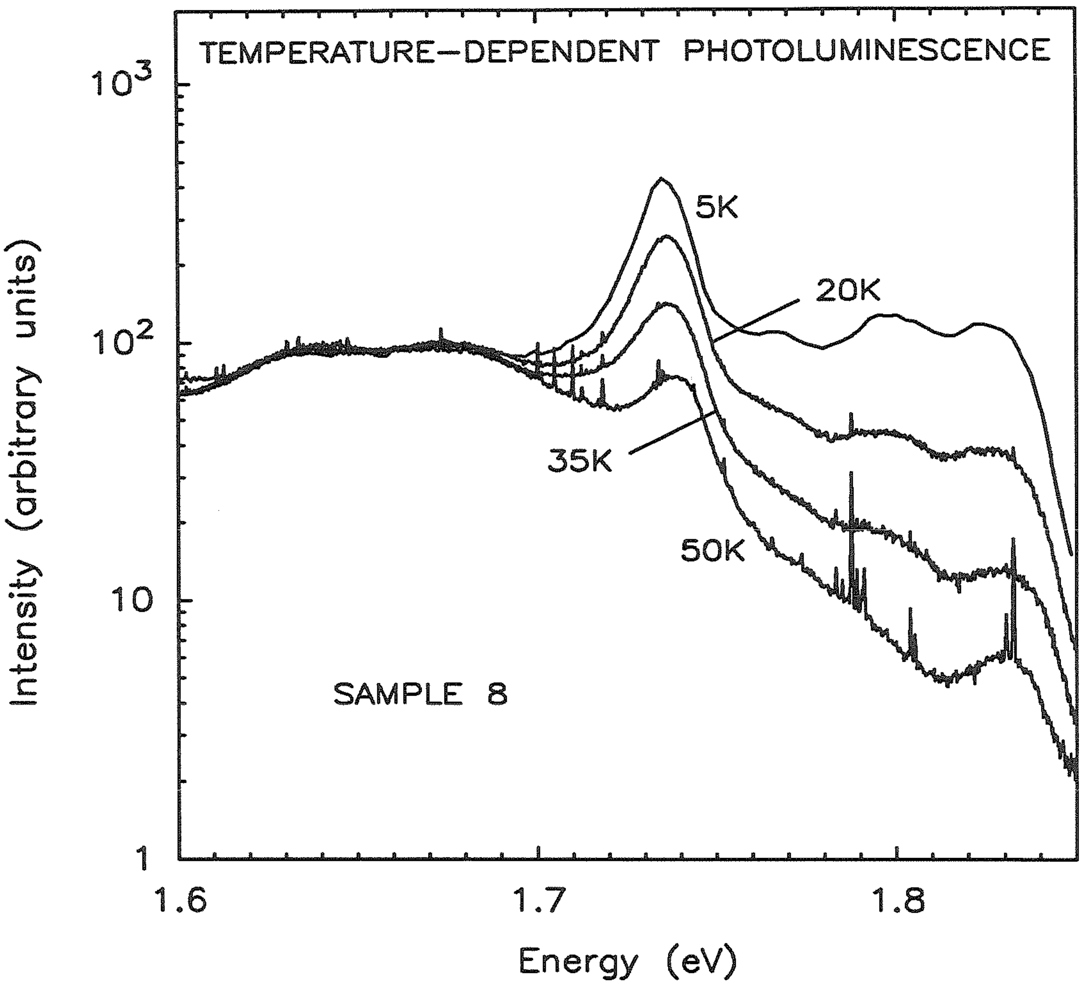

Figure 2.5: Photoluminescence spectra for CdTe/ZnTe superlattice sample 8 at 5K, 20K, 35K, and 50K under constant pump conditions. Luminescent intensity is plotted against emitted photon energy. Each of the four distinct luminescence peaks from the superlattice (above 1.7eV) shows a strong temperature dependence, whereas luminescence from the $Cd_{0.5}Zn_{0.5}$ buffer (below 1.7eV) shows almost none. The regular 30meV spacing and the similarity of the temperature and pump-power dependences of the superlattice peaks suggest that they originate from the same basic recombination process but are associated with quantum wells that differ in width by a single monolayer of CdTe. Narrow spikes on the spectra are due to plasma lines from the pump laser.

pump-power dependences strongly suggest that the lines are associated with the same basic recombination process. The four discernible peaks are regularly spaced at an interval of approximately 30meV. This is the shift in band gap expected from a fluctuation in CdTe layer thickness of one monolayer ($\simeq$ 3 Å) around a mean thickness of 20 Å. Thus, the features are probably due to a single recombination process taking place in layers that fluctuate in thickness over a range of $2a_0$. The presence of distinct peaks, rather than a single broad feature, is evidence of islanding with a characteristic dimension at least as large as the exciton within this sample. The Bohr radius of an exciton in bulk CdTe is $\simeq$ 60 Å.[18] Confinement in one dimension can be expected to increase this radius slightly.

Sample 8 is unique in displaying similar distinct peaks and in showing superlattice luminescence over such a broad range of energies. While it is not certain why sample 8 alone displays these peaks, growth kinetics presents a plausible explanation. Small changes in growth conditions are known to play a large role in determining growth modes; mobilities of atoms deposited upon a surface must be high enough to establish epitaxy but not so great as to tip the balance between two-dimensional and three-dimensional (island) growth.[19] While the growth conditions were nominally identical for all of the superlattices, a small change (in growth temperature, for example) could clearly affect the mobilities of surface atoms sufficiently to stimulate two-dimensional clustering. While the evidence that sample 8 was grown at a higher temperature than the other superlattices is not conclusive, this is a plausible explanation for the islanding that results in the regularly spaced photoluminescence peaks observed from this sample. Regardless of the exact reason for the change in growth mode, it is clear that this sample alone displays two-dimensional clustering on a scale of $\geq$ 100 Å.

The origin of the two intense lines observed in the luminescence from sample 3 is less clear. Each of the two peaks displays a strong temperature dependence, but the binding energies of the two features appear to be substantially different. Based on this observation, it is unlikely that the two lines arise from the same recombination process. As shown in Section 2.4, band structure calculations have suggested that the lines could be due to recombinations related to the heavy-hole and light-hole ground states (confined in the CdTe and ZnTe layers, respectively). These levels are predicted to differ in energy by only 16meV in this sample, in excellent agreement with the observed 28meV separation between the lines. Attributing the lines to light- and heavy-hole excitonic recombinations is also consistent with the differing temperature dependences we observe, as excitons associated with the two hole states would not be expected to have the same binding energies.

Each of the superlattices displays luminescence of low intensity at energies lower than those of the intense peaks. The observed lines can be systematically related to the $Cd_xZn_{1-x}Te$ buffer layers and GaAs substrates. Although luminescence at energies substantially less than the band gap is to be expected from each of the superlattices, the background signal from underlying layers makes this difficult to isolate. As the strain-shifted band gaps of the superlattices were of primary interest in this study and could be inferred from the intense peaks, the luminescence at lower energies was not examined in detail.

We have chosen to associate the sample band gaps with the high-energy cutoffs of the intense luminescence peaks, typically approximately 40meV higher in energy than the peak. This may have introduced a systematic error into our experimental band gaps, but the magnitude of this error is unlikely to be more than 30meV. Luminescence that is due to a free exciton would appear at an energy $E = E_g - E_{\text{ex}}$, where the binding energy E_{ex} is 10meV in bulk CdTe or ZnTe[20] and would be less than 40meV after 2-dimensional confinement.[21] There is some evidence that the observed excitons drop into slightly lower energy states resulting from fluctuations within individual layers.[18] This would have the effect of further removing the

Table 2.2: CdTe/ZnTe superlattice and alloy band gaps. Energies are in eV.

Sample	Observed Gap	Alloy Gap
1	1.87	1.99
2	1.81	1.89
3	1.67	1.93
4	1.81	1.97
5	1.83	1.99
6	1.82	1.97
7	1.74	1.99
9	1.78	1.98
$Cd_{0.37}Zn_{0.63}Te$	2.02	2.04

observed luminescence line from the sample band gap, by an energy in the range of 20meV.[18] In view of the uncertainties involved, the assignment of sample band gaps to the high-energy luminescence edges seems a good one, within a systematic error of less than 30meV.

The band gap of $Cd_{(1-y)}Zn_yTe$ at 12K has been measured to be[17]

$$E_g(\text{eV}) = (1.598 \pm 0.005) + (0.614 \pm 0.010)y + (0.166 \pm 0.010)y^2 \tag{2.2}$$

for Zn fraction y. As shown in Table 2.2, observed superlattice band gaps are substantially smaller than those calculated for equivalent alloys. This shift to lower energy is in general agreement with theory; superlattices typically display band gaps that are lower in energy than those of alloys with the same composition.

2.4 Calculations of electronic band structure

The electronic band structure of strained II-VI superlattices has been calculated using Bastard[22] and $\vec{k}\cdot\vec{p}$[23,24,25,26] models which incorporate effects that are due to strain. The calculations were performed to infer strain distributions in CdTe/ZnTe superlattices from observed band gaps. Independent experiments reveal the strain distributions to be in excellent agreement with those predicted by this method (see Chapter 3). The success of the two-band model in describing CdTe/ZnTe band gaps and the ease of computation have stimulated predictions of band gaps for a wide range of strained II-VI superlattices (included in the Appendix). These calculations demonstrate the sensitivity of superlattice band gaps to valence band offsets and suggest that photoluminescence experiments may be able to resolve long-standing uncertainties over II-VI band offsets.

2.4.1 Bastard and $\vec{k}\cdot\vec{p}$ models

The $\vec{k}\cdot\vec{p}$ model used to calculate CdTe/ZnTe superlattice band gaps has been described extensively elsewhere.[23,24,25,26] The method is a perturbation technique that allows bulk band structure to be calculated around a point for which the eigenvalues of the system are known. Superlattice band structure is derived by imposing the conditions of wave-function continuity and conservation of current at the interfaces, as well as invariance of the Bloch functions under lattice vector translations. Ours is a second-order perturbation calculation with spin-orbit and strain effects included. The basis set consists of the two bottom (s-like) conduction bands and six highest (p-like) valence bands. Effects that are due to bands not included in the basis set are added through Luttinger valence-band parameters.[27]

Our basis set is described by the band gap at the $\Gamma-$point E_0; the spin-orbit splitting Δ_0 at this point; and E_p, which is related to the square of the momentum matrix element between s and p states. These and the Luttinger parameters q, γ_2, and γ_3 were taken from Lawaetz.[28] We set q to zero and γ_2 and γ_3 equal to the average of γ_2 and γ_3. This approximation simplifies computations and is consistent with characteristics of isotropic bulk bands. We assume a zero valence band offset between ZnTe and CdTe. Although the value of the valence band offset is uncertain, it is thought to be small; Duc and Faurie[29] report an experimental CdTe/ZnTe offset of 100meV, whereas Katnani and Margaritondo[30] find an offset of -100meV. Calculations suggest that the offset is approximately zero.[31] We use 4K band gaps of 1.606eV for CdTe and 2.38eV for ZnTe.[28]

Strain effects are included through a four-parameter deformation potential. We follow Bir and Pikus[32] in defining the three independent strain parameters a, b, and d. Hydrostatic shifts in energy bands originating from p-like orbitals are described by a, whereas parameters b and d characterize shifts arising from (100)- and (111)-oriented uniaxial strains, respectively. In addition, a parameter c is introduced to describe hydrostatic shifts in s-like energy bands. For ZnTe we take $b = -1.78\,\text{eV}$ and $d = -4.58\,\text{eV}$, from Kaplyanskii and Suslina.[33] For CdTe, $b = -1.18\,\text{eV}$ and $d = -4.83\,\text{eV}$, in accordance with Thomas.[34] Pressure coefficients yield $a = 1.35\,\text{eV}$, $c = -2.70\,\text{eV}$ for ZnTe and $a = 1.23\,\text{eV}$, $c = -2.20\,\text{eV}$ for CdTe.[35] Elastic constants were taken from McSkimin and Thomas[36] for CdTe and from Berlincourt *et al.*[37] for ZnTe.

A first-order $\vec{k} \cdot \vec{p}$ theory has been used to calculate band gaps of a variety of II-VI superlattices. The method is essentially one that is due to Bastard,[22] with the addition of strain effects. Although this method does not include the higher-order corrections to the Hamiltonian incorporated in the second-order theory, it yields a simple analytical expression for the zone-center band gaps.

The Bastard model gives solutions for the slowly varying envelope functions that modulate the Bloch functions to form the superlattice wave function,

$$\psi_{n\vec{k}}^{A,B} = \left(\alpha^{A,B}(z)e^{i\vec{k}\cdot\vec{r}} + \beta^{A,B}(z)e^{-i\vec{k}\cdot\vec{r}}\right)u_{n\vec{k}}. \tag{2.3}$$

The superlattice wave function is constrained to be continuous and to conserve current at the interfaces (*i.e.*, ψ, $\frac{1}{m^*}(\frac{d\psi}{dz})$ continuous). Inserting this wave function into the Schrodinger equation yields an implicit equation for the dispersion $q(E)$ of the electronic valence and conduction bands:[22]

$$\cos[q(l_A + l_B)] = \cos(k_A l_A)\cos(k_B l_B) - \frac{1}{2}\left(x + \frac{1}{x}\right)\sin(k_A l_A)\sin(k_B l_B), \tag{2.4}$$

where

$$x = \frac{\Delta E_{AB} - E}{E}\frac{k_B}{k_A} \tag{2.5}$$

in the light particle case and

$$x = \frac{m_A k_B}{m_B k_A} \tag{2.6}$$

for the heavy-hole bands. In these equations, q denotes the superlattice wave vector, l_i is the thickness of layers of material i within the superlattice, k_i describes electronic motion along the superlattice axis in layer i, and ΔE_{AB} is the energy offset between the bulk bands (*i.e.*, the height of the quantum well).

Strain effects are easily incorporated within this model for calculations of zone center band gaps. The shifts are readily calculated according to Eqn. 1.3 and are incorporated as modifications to the input band-edge positions. Correct treatment of the coupling between light- and heavy-hole states requires additional terms in the Hamiltonian for $\vec{k} \neq 0$, but the approach used here is correct for the zone center.[38] The strains $\varepsilon^{(i)}$ within material i are determined by the in-plane lattice constants $a_{\|}^{(i)}$ within the superlattice. For the case of (100)-oriented growth these are given by

$$\varepsilon_{xx}^{(i)} = \varepsilon_{yy}^{(i)} = \frac{a_0^{(i)} - a_{\|}^{(i)}}{a_0^{(i)}} \tag{2.7}$$

$$\varepsilon_{zz}^{(i)} = -2\frac{C_{12}^{(i)}}{C_{11}^{(i)}}\varepsilon_{xx}, \tag{2.8}$$

where the C's are bulk elastic constants. All other ε_{ij}'s are zero in this case.

One case of particular interest is that of the free-standing superlattice, in which the elastic energy of the structure has been minimized with respect to a single in-plane lattice constant.* The elastic energy density of a cubic crystal reduces to

$$U = C_{11}(\varepsilon_{xx}^2 + \frac{1}{2}\varepsilon_{zz}^2) + C_{12}(2\varepsilon_{xx}\varepsilon_{zz} + \varepsilon_{xx}^2) \tag{2.9}$$

for (100)-oriented growth. Minimizing $l_A U^{(A)} + l_B U^{(B)}$ with respect to $a_{\|}$ yields

$$a_{\|} = \frac{l_A G^A a_0^{B^2} a_0^A + l_B G^B a_0^{A^2} a_0^B}{l_A G^A a_0^{B^2} + l_B G^B a_0^{A^2}}, \tag{2.10}$$

where

$$G^i = C_{11}^{(i)} + C_{12}^{(i)} - 2\frac{C_{12}^{(i)^2}}{C_{11}^{(i)}}. \tag{2.11}$$

Inserting strains derived from these expressions into Eqn. 1.3 gives the shifts in bulk band edges within a free-standing superlattice.

2.4.2 Results

Measured CdTe/ZnTe superlattice band gaps are compared with those calculated from second-order $\vec{k}\cdot\vec{p}$ theory in Table 2.3. Band gaps have been calculated for the three cases of growth strained according to the template set by the topmost buffer layer, free-standing strained growth, and unstrained growth. As is apparent from the table, agreement between $\vec{k}\cdot\vec{p}$ calculations and experiment is good when the in-plane lattice constants are assumed to be those of the free-standing superlattices. Calculations based on these lattice constants are in all cases within

---

*Physically, this is achieved by a network of misfit dislocations lying at the superlattice/buffer layer interface. However, the superlattice itself is dislocation-free in this configuration.

Table 2.3: CdTe/ZnTe experimental and calculated superlattice band gaps. Energies are in eV.

		$\vec{k}\cdot\vec{p}$ with strain		$\vec{k}\cdot\vec{p}$
Sample	Experiment	($a_0^{\text{free-standing}}$)	($a_0^{\text{substrate}}$)	(unstrained)
1	1.87	1.81	1.55	1.83
2	1.81	1.76	1.56	1.78
3	1.67	1.66	1.38	1.69
4	1.81	1.80	1.78	1.82
5	1.83	1.83	1.79	1.85
6	1.82	1.80	1.78	1.82
7	1.74	1.74	1.72	1.76
9	1.78	1.78	1.74	1.80

60 meV of the observed band gaps. By contrast, calculations that assume superlattice lattice constants equal to that of pure CdTe top buffer layers yield band gaps that are 250 to 320 meV lower than observed. Calculations based on a strain distribution derived from the topmost buffer layer are in better agreement with experiment when the layer is ZnTe or $\mathrm{Cd}_x\mathrm{Zn}_{1-x}\mathrm{Te}$, but the agreement is best when the superlattice is assumed to be free-standing.

Agreement between the free-standing calculations and experiment is as good as could be hoped, given the uncertainties in deformation potentials, experimental band gaps, and precise sample compositions. It is probable that samples 1-3, grown on CdTe buffer layers, are actually less CdTe-rich than suggested by EDS, owing to the volume probed by this technique (which extends slightly into the buffer layer).

This error is unlikely to be more than $\simeq 5\%$, which would raise the calculated gaps by a few tens of meV, bringing them into closer agreement with experiment. However, the magnitude of this and other errors is not sufficient to explain the discrepancies between experiment and theory when the superlattice is assumed to be commensurate with the CdTe buffer; strain in these samples is clearly not set by this layer. The same can probably be said of the strain field in sample 4, grown on a pure ZnTe buffer, but by chance the calculated gaps are too close to allow such a conclusion from consideration of band gaps alone.

Consideration of strain energies and critical thicknesses in the CdTe/ZnTe system suggests that the free-standing configuration is plausible. As shown in Eqn. 2.9, the elastic energy is quadratic in strain ε. Dividing a 6% strain in one set of layers into two 3% strains alternating between tension and compression clearly lowers the elastic energy considerably. For the superlattices considered here, this energy difference more than offsets the energy necessary to create a network of mismatch-relieving dislocations at the superlattice/buffer-layer interface (see Eqns. 1.4 and 1.5); the free-standing case is truly a lower energy state than the case of a structure strained to a pure CdTe or ZnTe buffer for the superlattices considered here.

Predictions of the critical thickness for the nucleation of misfit defects in $\mathrm{Cd}_x\mathrm{Zn}_{1-x}\mathrm{Te}$ films are plotted in Fig. 2.6. Also included are the thicknesses and net mismatches of the superlattices examined here. Note that each sample contributes several points, connected by lines for purposes of identification, corresponding to the thicknesses and misfits of the individual CdTe and ZnTe layers and of the alloy equivalent in composition and thickness to the superlattice as a whole. Sample 8, for example, gives a point at $(0.07\%, 1.64\,\mu\mathrm{m})$, since this superlattice is $1.64\,\mu$m thick with a 51% CdTe, 49% ZnTe volume-averaged composition, grown on a $\mathrm{Cd}_{.50}\mathrm{Zn}_{.50}\mathrm{Te}$ buffer layer ($a_{\mathrm{Cd}_{0.51}\mathrm{Zn}_{0.49}\mathrm{Te}}/a_{\mathrm{Cd}_{0.5}\mathrm{Zn}_{0.5}\mathrm{Te}} = 0.07\%$ misfit). This point

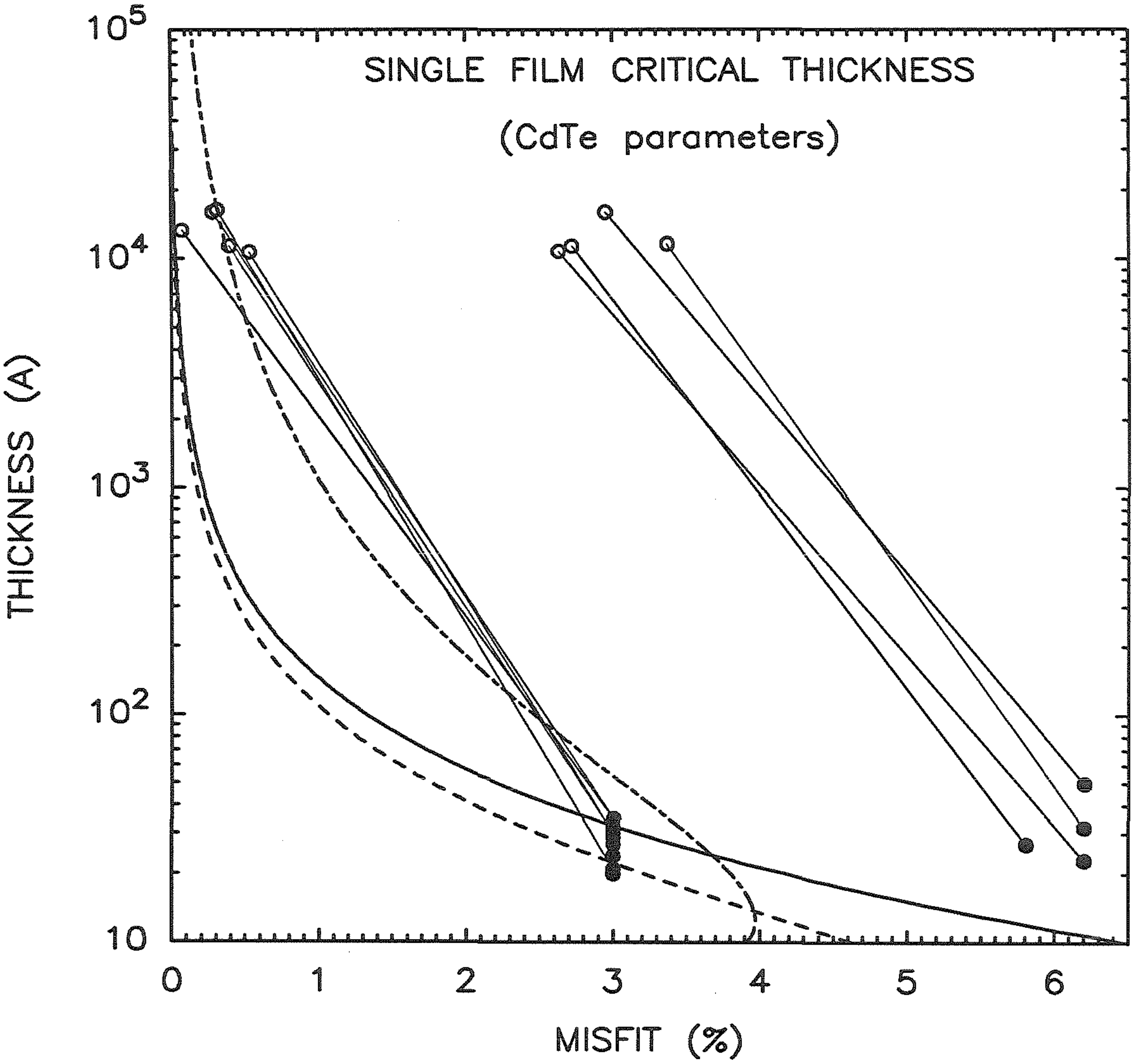
SINGLE FILM CRITICAL THICKNESS
(CdTe parameters)
THICKNESS (A)
MISFIT (%)
10^5
10^4
10^3
10^2
10
0
1
2
3
4
5
6

Figure 2.6:

Figure 2.6: Theoretical predictions of critical thickness at which a thin $Cd_xZn_{1-x}Te$ film poorly lattice-matched to a substrate breaks away from that substrate with the formation of misfit dislocations. Calculations assumed dislocations appropriate to (100)-oriented growth of CdTe. The solid curve comes from an energy-balancing argument[39] similar to that of Eqn. 1.7; the dashed curve below it is from Eqn. 1.9, Ref. 40; and the last is from Eqn. 1.10, Ref. 41. Also included are points corresponding to sample thicknesses and misfits. Each sample contributed several points, connected by lines for purposes of identification, appropriate to the thicknesses and misfits of the individual layers in the superlattice (filled circles) and of the alloy of identical composition and thickness to the overall superlattice (unfilled circles). Sample 2, for example, gives a point at $(2.47\%, 1.08\,\mu m)$ since this is a $1.08\,\mu m$−thick superlattice with a composition equivalent to a $Cd_{0.57}Zn_{0.43}Te$ alloy, grown on a CdTe buffer layer (2.47% mismatch). This point is connected to one at $(5.8\%, 23\,\text{Å})$ appropriate to the 23 Å ZnTe layers grown on the CdTe buffer. The point derived from the individual CdTe layers, $(0\%, 31\,\text{Å})$, has not been plotted since the zero mismatch places no constraints on CdTe layer thickness. Theory clearly predicts that this particular superlattice should exceed the critical thickness. This agrees with experiment.

is connected to others at (3.0%, 21 Å) and (3.0%, 20 Å) appropriate to the thicknesses and misfits of the individual CdTe and ZnTe layers, respectively. (Note that samples grown on pure CdTe or ZnTe contribute only two points as there is no critical thickness requirement for the individual CdTe or ZnTe layers, respectively, in these structures.) The superlattices grown on pure CdTe or ZnTe buffer layers exceed both of the critical thickness requirements outlined in Section 1.4.2. As shown in the figure, the individual ZnTe or CdTe layers within these superlattices lie well beyond the limits for defect-free growth. In addition, the superlattices are of sufficient overall thickness to substantially exceed the critical thickness for the creation of mismatch-accommodating dislocations at the superlattice/buffer-layer interface.

While several of the superlattices appear to exceed the limits of dislocation-free growth, allowing the superlattices to break away from the topmost buffer layer to assume a free-standing configuration puts them below the critical thicknesses predicted by the empirical model of People and Bean.[41]. Their calculations suggest that individual CdTe and ZnTe layers with a 3% strain can be grown beyond a thickness of 50 Å. Note that the overall superlattice thickness does not impose a critical thickness constraint as the DC component of the strain field is zero in this configuration.

As shown in Fig. 2.7, the relaxation of mismatch stresses can be sufficiently gradual beyond the critical thickness to allow a large strain to be divided into lesser expansions and contractions. In the limit of very thick individual superlattice layers, dislocation networks could form at every interface in sufficient densities to totally relieve the strain within the structure. This does not appear to be the case in our samples. Such dislocation-filled structures would not be expected to luminesce efficiently, in contrast to our observations from these CdTe/ZnTe superlattices. Although the electronic band structure of an unstrained superlattice should be

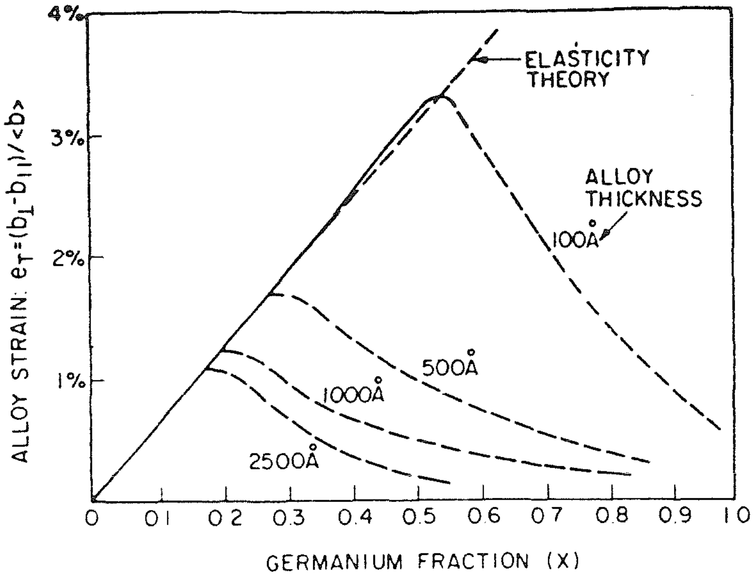

Figure 2.7: Strain relaxation beyond the critical thickness in the Ge_xSi_{1-x} system. From Ref. 42.

very different from that of a free-standing structure, we were unable to distinguish the two cases simply on the basis of observed band gaps. For these samples, valence band shifts arising from uniaxial strains approximately cancel the band gap dilations expected from hydrostatic strain. This coincidence arises solely from our choice of superlattice compositions; there should be a sizable difference in band gaps of free-standing and unstrained superlattices in structures substantially CdTe- or ZnTe-rich.

To summarize, comparison of observed and calculated band gaps shows that superlattices grown on CdTe buffer layers are not strained to fit this template. Based on calculations of strain effects, it is proposed that the superlattices may be in a nearly free-standing configuration, with a dislocation network at the superlattice/buffer-layer interface dividing the strain between adjacent layers to minimize the elastic energy of the structure. This is a plausible configuration for our samples, as the gradual relaxation of strain observed in the Ge_xSi_{1-x} system beyond the critical thickness demonstrates that initial CdTe or ZnTe superlattice layers might experience only partial relaxation. Consideration of critical thicknesses shows that our superlattices could be grown defect-free if the strain were distributed in a manner close to the free-standing limit. Although the free-standing configuration cannot be distinguished from the case of an unstrained lattice simply on the basis of observed band gaps, the unstrained limit is highly improbable in view of the high luminescent efficiencies observed from these structures.

Theoretical superlattice band gaps for samples with 1 to 30 CdTe or ZnTe layers per superlattice period are shown in Figs. 2.8 and 2.9. Fig. 2.8 shows the superlattice band gap at 5 K as calculated from a Bastard model,[22] neglecting effects that are due to strain. Fig. 2.9 displays results of the same calculation when strain effects appropriate to a free-standing superlattice are included. Second-order corrections described by Luttinger valence band parameters have been neglected in our Bastard model calculations, resulting in band gaps consistently 10 to 20 meV lower than predicted by the eight-band $\vec{k} \cdot \vec{p}$ calculations. The Bastard model was chosen for these plots as it reduced computation time and differed from the $\vec{k} \cdot \vec{p}$ calculations only by this uniform 10 to 20 meV shift.

The unstrained band structure in Fig. 2.8 shows band gaps which vary between the bulk CdTe and ZnTe gaps of 1.6 and 2.38eV. Given the assumption of zero valence band offset between the constituent materials, the layer thickness dependences apparent in the figure are determined solely by the conduction band states. The path of the contours agrees with that expected from the basic periodic quantum-well problem (*i.e.*, Kronig-Penney model[43]). Increasing the ZnTe barrier thickness beyond $\simeq$ 10 monolayers has almost no effect on the band gap, as the quantum wells are virtually uncoupled in this limit.* Increasing the width of the

---

*Structures in which the coupling between adjacent wells is negligible are commonly referred to

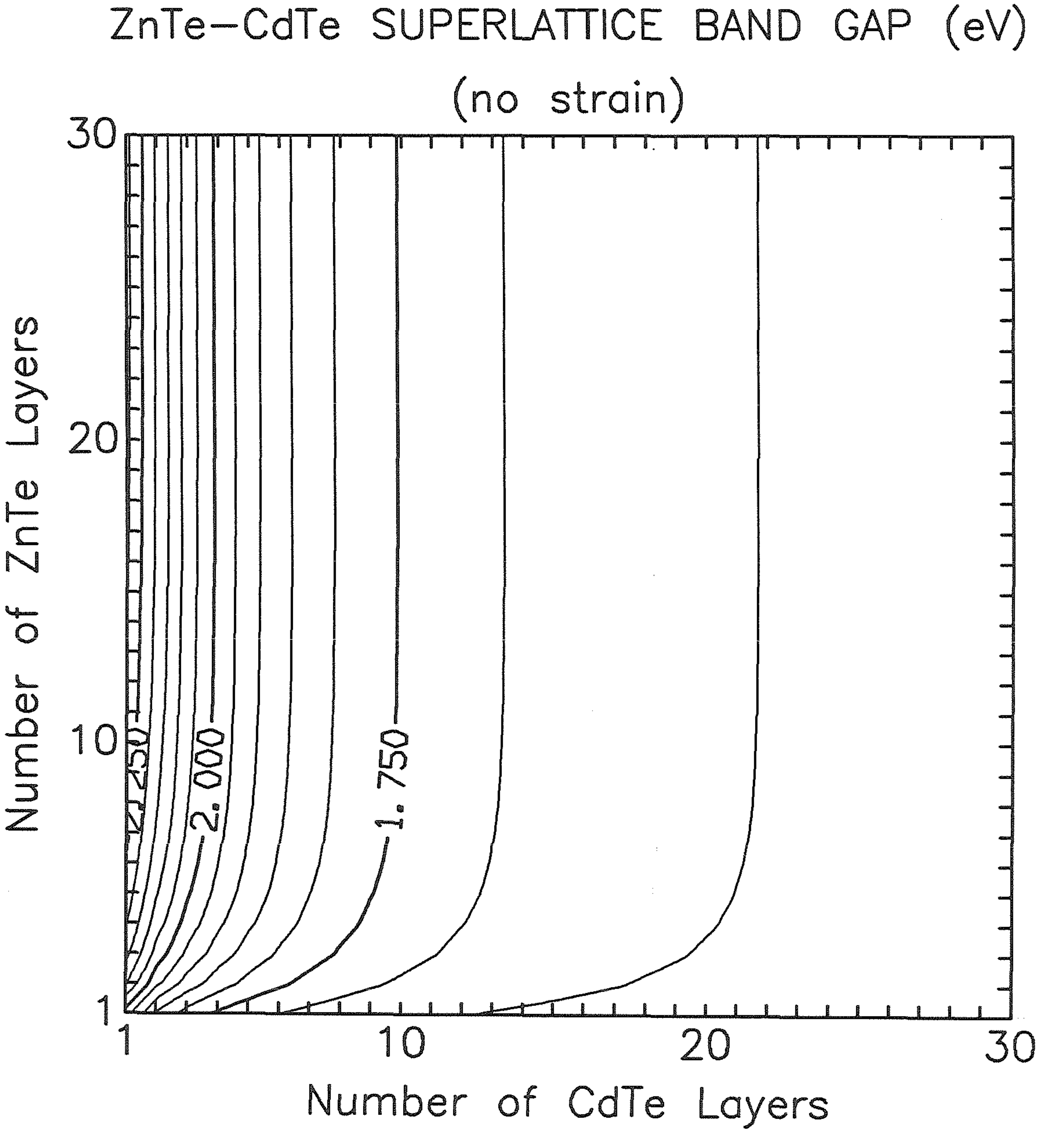

Figure 2.8: Theoretical CdTe/ZnTe superlattice band gaps at 5 K as a function of number of monatomic layers per superlattice period. Contour interval is 50 meV. Calculations are based on a Bastard model, neglecting effects that are due to strain.

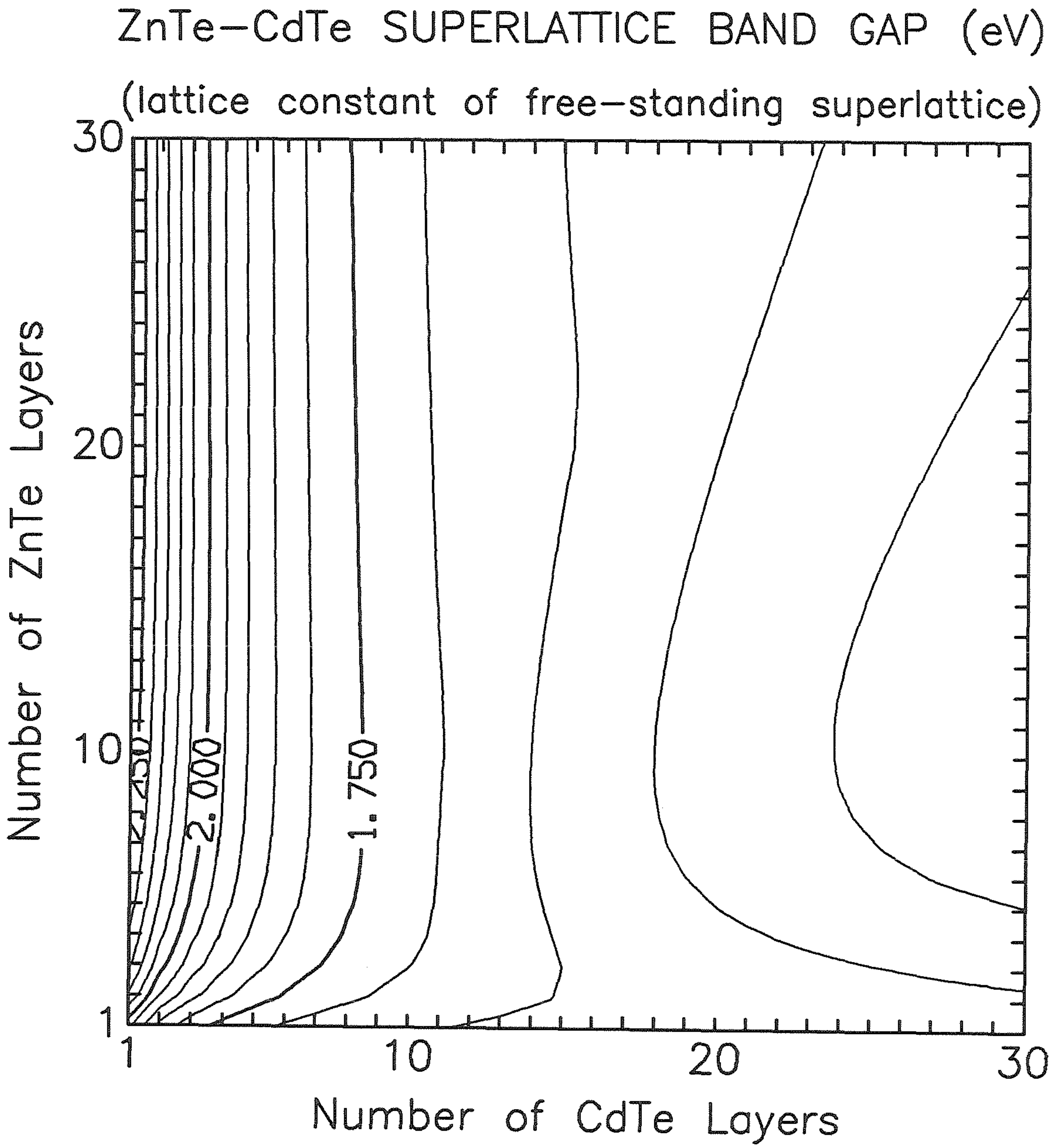

Figure 2.9: Calculated CdTe/ZnTe superlattice band gaps with strain effects included. Contour interval is 50 meV. Calculations assume in-plane lattice constants appropriate to free-standing superlattices.

CdTe wells draws the superlattice band gap asymptotically closer to that of CdTe, regardless of the ZnTe layer thickness.

Fig. 2.9 illustrates the role of strain in changing the superlattice band gap as CdTe or ZnTe layer thickness is modulated. For thick CdTe layers (more than about 15 monolayers), increasing the width of the ZnTe layers *lowers* the band gap over certain ranges of ZnTe thicknesses. This arises from the type-II character of the superlattices (in which carriers associated with conduction and valence band extrema are localized in different layers), depicted in Fig. 2.10. In both CdTe and ZnTe the light-hole band is pushed above the heavy hole for uniaxial compressional strain and below for uniaxial dilational strain. Hence, in our system the CdTe valence-band maximum is defined by the heavy-hole band edge, whereas the light-hole band maximum determines the ZnTe energy gap. Near the CdTe axis the ZnTe layers are heavily strained, pushing the ZnTe light-hole band above the CdTe bands and resulting in a light-hole to conduction-band energy gap for the superlattice. As the width of the ZnTe layer is increased, the superlattice valence-band edge approaches the ZnTe light-hole edge. This causes the band gap to decrease. However, as ZnTe concentration increases, the strain in the ZnTe layers is lowered, pulling the ZnTe light-hole band down. This effect starts to dominate at higher ZnTe concentrations, where the band gap starts to increase with greater ZnTe layer thicknesses. For high ZnTe-to-CdTe ratios, the ZnTe light-hole band drops sufficiently that the band gap is defined by the heavy-hole band. The transition between type-I and type-II band alignments is indicated in Fig. 2.11. Points in this figure correspond to the superlattices examined in this study. Note that of the samples we examined, only sample 3 should display a type-II band alignment, in agreement with photoluminescence.

It is worth noting that the accuracy of calculated superlattice band gaps is

---

as multiquantum well structures, rather than superlattices.

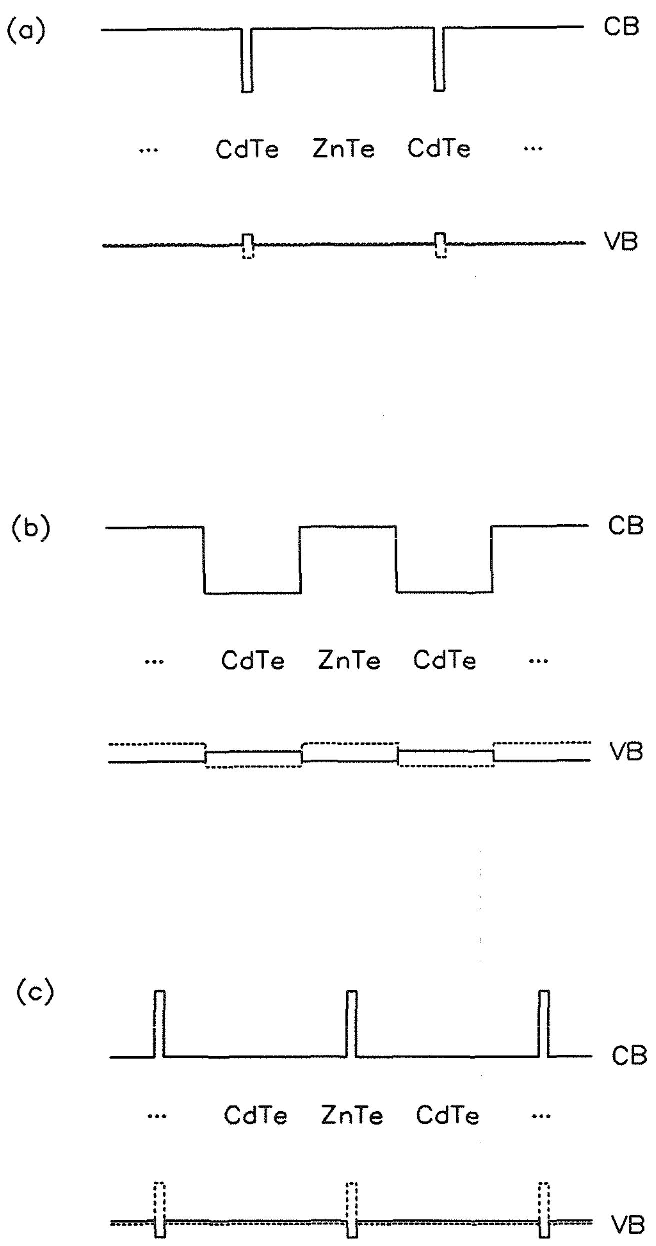

Figure 2.10: Calculated alignments of CdTe and ZnTe band edges with strain effects included. Three cases are shown: (a) ZnTe-rich superlattice, (b) equal CdTe and ZnTe layer thicknesses, and (c) CdTe-rich superlattice. Calculations assume strains appropriate to free-standing superlattices. Strain splits the valence band; heavy-hole valence-band edges are indicated by solid lines and light-hole edges by broken lines.

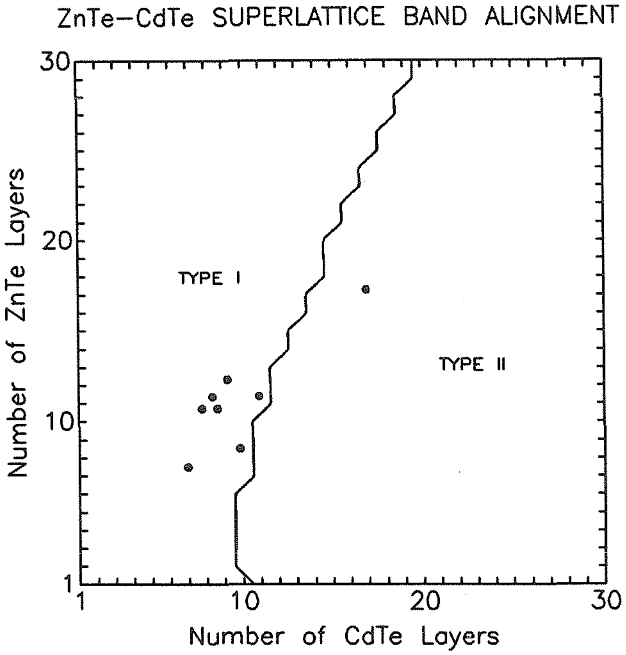

Figure 2.11: Band alignments for CdTe/ZnTe superlattices. In a type-I band alignment, carriers associated with valence- and conduction-band extrema lie in the same layers. Type-II alignments localize electrons and holes in different layers within the superlattice. Superlattices examined here are labeled by points. Only sample 3 is predicted to be type-II.

dependent upon the estimate of the valence band offset between the constituent materials. This dependence means that it is sometimes possible to infer a band offset by comparing experimental band gaps with those calculated from theory. While cumulative errors in theoretical and experimental band gaps translate into larger errors in valence band offset, uncertainties in offsets are sometimes large enough that this method can still be used to advantage. In the case of CdTe/ZnTe, our assumption of a zero valence band offset between CdTe and ZnTe yields gaps that are in good agreement with experiment. However, errors in deformation potentials, superlattice characteristics, and experimental band gaps could also place the offset at ±100meV, as suggested by other work.[29,30] ZnSe/ZnTe is an example of a system in which the offsets are less well known. Predictions[44,45] place this offset anywhere from 0.28eV to 1.20eV. Comparison of experimental and theoretical gaps suggests that $\Delta E_v = 1.0 \pm 0.1$eV in this system.[46]

2.5 Stimulated Emission

Attempts have been made to observe laser oscillation in a CdTe/ZnTe superlattice. As much of the interest in CdTe/ZnTe structures arises from the possibility of fabricating efficient light-emitting diodes with emission in the visible region of the spectrum, the demonstration of lasing in these superlattices is of practical interest. The intensity of the luminescence observed from our samples at 5K suggests that nonradiative or deep-level loss mechanisms may not preclude lasing. However, the stability of heavily strained structures under high pump power conditions is uncertain, as is the effect dislocations would have on the luminescence.[47] Although previous experiments on $\mathrm{In}_x\mathrm{Ga}_{1-x}\mathrm{As}_{1-y}\mathrm{P}_y$ structures with strains $\leq 1.25\%$ have demonstrated a catastrophic loss of luminescence after short periods of intense stimulated emission,[48] it is unclear that these results can be translated to $\mathrm{Cd}_x\mathrm{Zn}_{1-x}\mathrm{Te}$ structures. The elastic properties of II-VI semiconductors are substantially different from those of III-V's, as are the effects of dislocations on luminescent efficiency.

Stimulated emission refers to the creation of a photon of energy $\hbar\omega$ as a consequence of the decay of an excited electron-hole pair through interactions with another photon of energy $\hbar\omega$. When gain that is due to stimulated emission equals or exceeds losses arising from absorption in a given medium, light passing through the medium experiences a net amplification. Placing this amplifying medium inside a resonant cavity establishes laser oscillation when, for a single round-trip through the cavity, the gains equal or exceed the losses (arising, for example, from absorption and cavity reflection coefficients). For a cavity of length l, absorption coefficient α, and mirror reflectivities r_1 and r_2, the threshold gain condition is[49]

$$\gamma_t = \alpha - \frac{1}{l}\ln r_1 r_2. \tag{2.12}$$

Equating this threshold gain with that from stimulated emission in an excited two-level system yields an expression for the electron population inversion necessary to establish lasing in a particular structure. Above the excitation threshold necessary to establish lasing, the output power in a laser mode increases linearly with input power at a rate substantially in excess of that below threshold. This "knee" in output efficiency makes the threshold easy to identify experimentally.

In our experiment, inversion of the electron population was attempted by above-band-gap optical excitation, provided by the 5145 Å line of an Ar^+ ion laser. The laser was operated in a cavity-dumped mode with 12nsec pulses at repetition rates of 2.7kHz to 1.1MHz (chosen to keep the power at the sample low to reduce heating and possible damage effects). Peak pump powers were varied below 3W, providing incident powers on the order of $\mathrm{kW/cm^2}$ after focussing. This is in the range expected for semiconductor lasing thresholds.[50]

With the exception of the pump laser, the experimental setup is identical to that described in Section 2.3.2 for the cw photoluminescence experiments. Spectra were accumulated at temperatures of $5-8$K. Only sample 4 has been examined to date. This sample was chosen because of the ZnTe buffer layer on which it was grown, which helps to confine the superlattice luminescence within the active region. Two cavities were cleaved, approximately $120\,\mu$m × $450\,\mu$m in size. Luminescence from the edge and front surface of these samples was compared with that from a large piece of sample 4 accumulated under identical conditions.

As shown in Fig. 2.12, the cleaved cavities exhibit a catastrophic loss of luminescence after intense pumping ($\simeq 1\mathrm{kW/cm^2}$), while the uncleaved sample continues

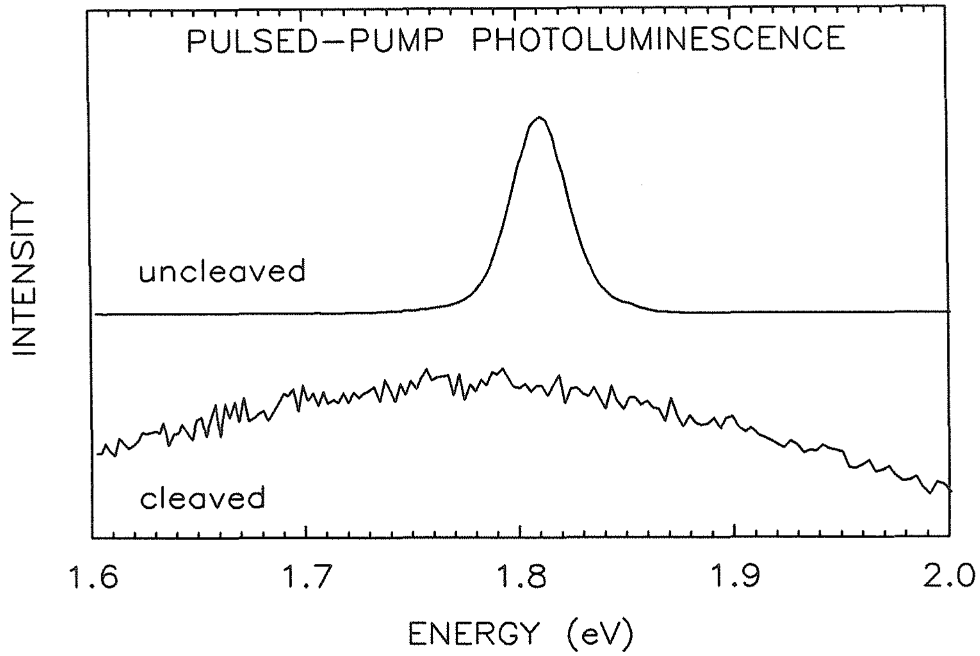

Figure 2.12: Photoluminescence at 8K from cleaved and uncleaved pieces of sample 4 under a pulsed Ar^+ pump with a peak power of $\simeq$ 1kW/cm^2. The intense excitonic peak has disappeared from the spectrum coming from the cleaved cavity, leaving only a weak, broad feature. The spectra are plotted on different vertical scales; luminescence from the uncleaved sample was more than two orders of magnitude more intense than that from the cleaved cavity.

to display a strong excitonic line. This loss occurred prior to the observation of Fabry Perot modes on the spectrum, although it should be noted that the samples were illuminated for several minutes before a complete photoluminescence spectrum was accumulated. Whether this loss of luminescence is intrinsic to heavily strained CdTe/ZnTe superlattices is unclear at this time. The recent observation of lasing in an InAs/GaAs multiquantum well structure[51] with a 7.4% lattice mismatch demonstrates that large strain fields can be accommodated during stimulated emission. By tailoring CdTe/ZnTe superlattices during growth, it may be possible to inhibit the mechanisms responsible for the degradation of luminescence under intense pump conditions. This is the subject of ongoing work.

Despite the failure to obtain laser oscillation in superlattices with layers composed of pure CdTe and ZnTe, it should be noted that $Cd_{0.25}Zn_{0.75}Te/ZnTe$ superlattices have recently been shown to lase.[8] These structures appear to be less susceptible to structural damage owing to the smaller lattice mismatch between adjacent layers. In addition, the Zn-rich composition results in higher-energy primary emission, in the yellow-orange region of the spectrum. These superlattices have been observed to lase without noticable degradation at room temperature,* providing optimism for future device applications.

2.6 Conclusions

We have examined optical properties of CdTe/ZnTe superlattices grown on a variety of $Cd_xZn_{1-x}Te$ buffer layers. Photoluminescence from the superlattices is several orders of magnitude more intense than from a $Cd_{0.37}Zn_{0.63}Te$ alloy under the conditions examined here. Spectra are dominated by broad lines probably associated with excitons. The 30meV width of these lines suggests that superlattice layer thicknesses were controlled to approximately one monolayer. Identifying the superlattice band gaps as the high-energy edges of the observed excitonic luminescence yields sample band gaps substantially lower than expected for alloys. Observed gaps are in excellent agreement with those calculated from a $\vec{k} \cdot \vec{p}$ model, assuming strain appropriate to a free-standing structure. This configuration is one in which dislocations at the superlattice/buffer-layer interface have redistributed strain within an otherwise dislocation-free superlattice in a manner which minimizes the elastic strain energy within the structure. The free-standing configu-

---

*These are believed to be the first II-VI superlattices to lase at room temperature.

ration is plausible in view of calculated critical thicknesses and strain relaxation rates. We have made calculations of the effects of a free-standing strain on the superlattice valence and conduction band edges. Strain is shown to reduce band gaps by up to 100meV over the range studied, and to result in transitions from type-I to type-II band alignments. Attempts to observe laser oscillation in CdTe/ZnTe superlattice structures have proven unsuccessful to date, but this is the subject of further work; the intensity of the luminescence observed from these superlattices suggests that they may ultimately find application as visible light emitters.

References

1. See, for example, *Physics and Chemistry of II-VI Compounds*, edited by M. Aven and J. S. Prener (Wiley, New York, 1967).
2. F. F. Morehead, in *Physics and Chemistry of II-VI Compounds*, edited by M. Aven and J. S. Prener (Wiley, New York, 1967), p. 613.
3. T. Yasuda, I. Mitsuishi, and H. Kukimoto, *Appl. Phys. Lett.* **52**, 57 (1987).
4. R. D. Feldman, R. F. Austin, P. H. Fuoss, A. H. Dayem, E. H. Westerwick, S. Nakahara, T. Boone, J. Menendez, A. Pinczuk, J. P. Valladares, and S. Brennan, *J. Vac. Sci. Technol. B* **5**, 690 (1987).
5. T. Yokogawa, M. Ogura, and T. Kajiwara, *Appl. Phys. Lett.* **49**, 1702 (1986).
6. M. Kobayashi, R. Kimura, M. Konagai, and K. Takahashi, *J. Cryst. Growth* **81**, 495 (1987).
7. G. C. Osbourn, *Phys. Rev. B* **27**, 5126 (1983).
8. A. M. Glass, K. Tai, R. B. Bylsma, R. D. Feldman, D. H. Olson, and R. F. Austin, unpublished.
9. J. P. Faurie, talk presented at the Defense Advanced Research Projects Agency Focal Plane Array Materials Devices and Processing Conference, McLean, Virginia, April 1985.

10. D. W. Kisker, P. H. Fuoss, J. J. Krajewski, P. M. Armirtharaj, S. Nakahara, and J. Menendez, *J. Cryst. Growth* **86**, 210 (1988).

11. W. H. Knox, C. Hirlimann, D. A. B. Miller, J. Shah, D. S. Chemla, and C. V. Shank, *Phys. Rev. Lett.* **56**, 1191 (1986).

12. J. I. Pankove, *Optical Processes in Semiconductors* (Dover, New York, 1975).

13. M. Tajima, *Jpn. J. Appl. Phys. Suppl.* **21**, 113 (1982).

14. A. T. Hunter and T. C. McGill, *Appl. Phys. Lett.* **40**, 169 (1982).

15. P. L. Gourley, T. J. Drummond, and B. L. Doyle, *Appl. Phys. Lett.* **49**, 1101 (1986).

16. S. R. Hetzler, Ph.D. Thesis, California Institute of Technology, 1986.

17. D. J. Olego, J. P. Faurie, S. Sivananthan, and P. M. Raccah, *Appl. Phys. Lett.* **47**, 1172 (1985).

18. Y. Hefetz, D. Lee, A. V. Nurmikko, S. Sivananthan, X. Chu, and J.-P. Faurie, *Phys. Rev. B* **34**, 4423 (1986).

19. R. Ludeke, *J. Vac. Sci. Technol. B* **2**, 400 (1984).

20. B. Segall and D. T. F. Marple, in *Physics and Chemistry of II-VI Compounds*, edited by M. Aven and J. S. Prener (Wiley, New York, 1967), p. 319.

21. D. S. Chemla, *Helvetica Physica Acta* **56**, 607 (1983).

22. G. Bastard, *Phys. Rev. B* **24**, 5693 (1981); **25**, 7584 (1982).

23. E. O. Kane, in *Semiconductors and Semimetals*, edited by R. K. Willardson and A. C. Beer (Academic, New York, 1966), Vol. 1, p. 75.

24. D. L. Smith and C. Mailhiot, *Phys. Rev. B* **33**, 8345 (1986).

25. G. Y. Wu, Ph.D. Thesis, California Institute of Technology, 1988.

26. C. Mailhiot, Ph.D. Thesis, California Institute of Technology, 1984.

27. J. M. Luttinger, *Phys. Rev.* **102**, 1030 (1956).

28. P. Lawaetz, *Phys. Rev. B* **4**, 3460 (1971).

29. T. M. Duc and J.-P. Faurie, *Phys. Rev. Lett.* **58**, 1127 (1987).

30. A. D. Katnani and G. Margaritondo, *J. Appl. Phys.* **54**, 2522 (1983).

31. A. D. Katnani and G. Margaritondo, *Phys. Rev. B* **28**, 1944 (1983).

32. G. L. Bir and G. E. Pikus, *Symmetry and Strain-Induced Effects in Semiconductors* (Keter, Jerusalem, 1974).

33. A. A. Kaplyanskii and L. G. Suslina, *Soviet Physics - Solid State* **7**, 1881 (1966).

34. D. G. Thomas, *J. Appl. Phys. Suppl.* **32**, 2298 (1961).

35. D. L. Camphausen, G. A. N. Connell, and W. Paul, *Phys. Rev. Lett.* **26**, 184 (1971).

36. H. J. McSkimin and D. G. Thomas, *J. Appl. Phys.* **33**, 56 (1962).

37. D. A. Berlincourt, H. Jaffe, and L. R. Shiozawa, *Phys. Rev.* **129**, 1009 (1963).

38. P. Voisin, *Surf. Sci.* **168**, 546 (1986).

39. J. H. Van der Merwe, *J. Appl. Phys.* **34**, 123 (1963).

40. J. W. Matthews and A. E. Blakeslee, *J. Cryst. Growth* **27** 118 (1974); **29** 273 (1975); **32** 265 (1976).

41. R. People and J. C. Bean, *Appl. Phys. Lett.* **47**, 322 (1985); **49**, 229(E) (1986).

42. R. People, *IEEE J. Quant. Elect.* **QE-22**, 1696 (1986).

43. R. de L. Kronig and W. G. Penney, *Proc. Roy. Soc. (London) A* **130**, 499 (1931).

44. W. A. Harrison and J. Tersoff, *J. Vac. Sci. Technol. B* **4**, 1068 (1986).

45. C. G. Van der Walle, *J. Vac. Sci. Technol. B*, to be published.

46. Y. Rajakarunanayake, R. H. Miles, G. Y. Wu, and T. C. McGill, *Phys. Rev. B*, to be published; *J. Vac. Sci. Technol. B*, to be published.

47. B. W. Hakki and T. L. Paoli, *J. Appl. Phys.* **44**, 4113 (1973).

48. M. D. Camras, J. M. Brown, N. Holonyak, Jr., M. A. Nixon, R. W. Kaliski, M. J. Ludowise, W. T. Dietze, and C. R. Lewis, *J. Appl. Phys.* **54**, 6183 (1983).

49. A. Yariv, *Quantum Electronics* (Wiley, New York, 1975), p. 179.

50. R. J. Phelan, Jr., and R. H. Rediker, *Appl. Phys. Lett.* **6**, 70 (1965).

51. M. A. Tischler, N. G. Anderson, R. M. Kolbas, and S. M. Bedair, *Appl. Phys. Lett.* **50**, 1266 (1987).

Chapter 3

Structural Properties of CdTe/ZnTe Superlattices

3.1 Introduction

3.1.1 Background

The structural studies described here represent an extension of the CdTe/ZnTe work described in Chapter 2. Although the photoluminescence study in the previous chapter revealed that CdTe/ZnTe superlattices grown on CdTe buffers do not maintain the in-plane lattice constant of CdTe, it was not possible to distinguish the case of free-standing growth from that in which lattice mismatch is wholly accommodated by dislocations.

As dislocations are known to affect the durability and performance of a lattice-mismatched device,[1,2] determining the levels of elastic strain in these superlattices is of practical interest. However, in addition to the particular interest of accommodating lattice mismatch in a material system of technological interest, these samples provide a test of the traditional single-film critical thickness theories and their extrapolation to superlattices. Although the x-ray diffraction experiment presented here reproduced data obtained in a previous study,[3] our interpretation of the data yields conclusions substantially at variance with those drawn from application of Vegard's Law in the previous study.

3.1.2 Results of this work

X-ray diffraction shows that each of the CdTe/ZnTe superlattices examined here lies beyond the critical thickness for creation of misfit defects. However, TEM and *in-situ* RHEED results show that defect densities drop dramatically away from the superlattice/buffer-layer interface. Substantial free-standing superlattice strains are observed in all but one of the samples. The most highly defective superlattice is below the critical thicknesses predicted for the individual layers and for the superlattice as a whole, unlike a number of more highly strained samples. Photoluminescence data suggest that this relaxation may be attributable to a slight variation in sample-to-sample growth conditions. Our results demonstrate that the critical thickness of a particular sample may be dependent upon the thermal history of the sample, in addition to the material system and lattice mismatch.

3.1.3 Outline of chapter

Section 3.2.1 describes the application of x-ray diffraction to the determination of strain in a superlattice. A kinematical model of x-ray diffraction is also presented in this section. Section 3.2.2 summarizes results of x-ray diffraction experiments on the CdTe/ZnTe superlattices described in Chapter 2. Observed diffraction is compared with that calculated for the three limiting cases of unstrained, free-standing strained, and commensurate structures. Results from x-ray diffraction are compared with conclusions drawn from the photoluminescence experiments and critical thickness calculations described in Chapter 2. TEM and *in-situ* RHEED results are outlined in Section 3.3. The conclusions are summarized in Section 3.4.

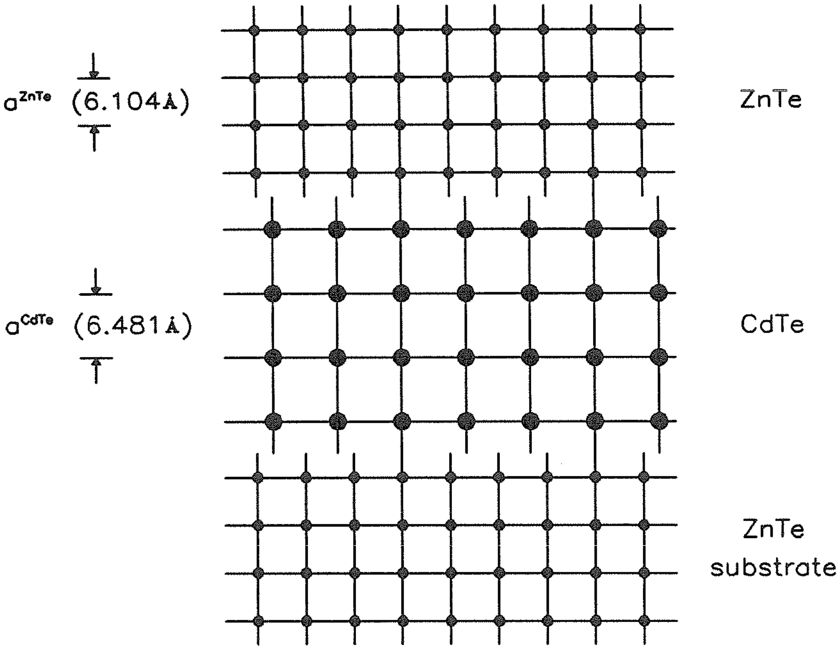

Figure 3.1: Arrangement of cubic unit cells in an unstrained CdTe/ZnTe superlattice.

3.2 X-ray diffraction

3.2.1 Theory

By revealing the structure and lattice constants of a crystal, x-ray diffraction provides a means of identifying the three limiting cases of unstrained, commensurate strained, and free-standing strained growth (depicted in Figs. 3.1 and 3.2). Assuming (100)-oriented epitaxy and applicability of linear elasticity theory, the degree to which lattice mismatch has been accommodated by elastic strain can be determined by a single measurement of the growth-direction lattice constants within a superlattice. As shown in Section 2.4.1, growth-direction strains ε_{zz} are

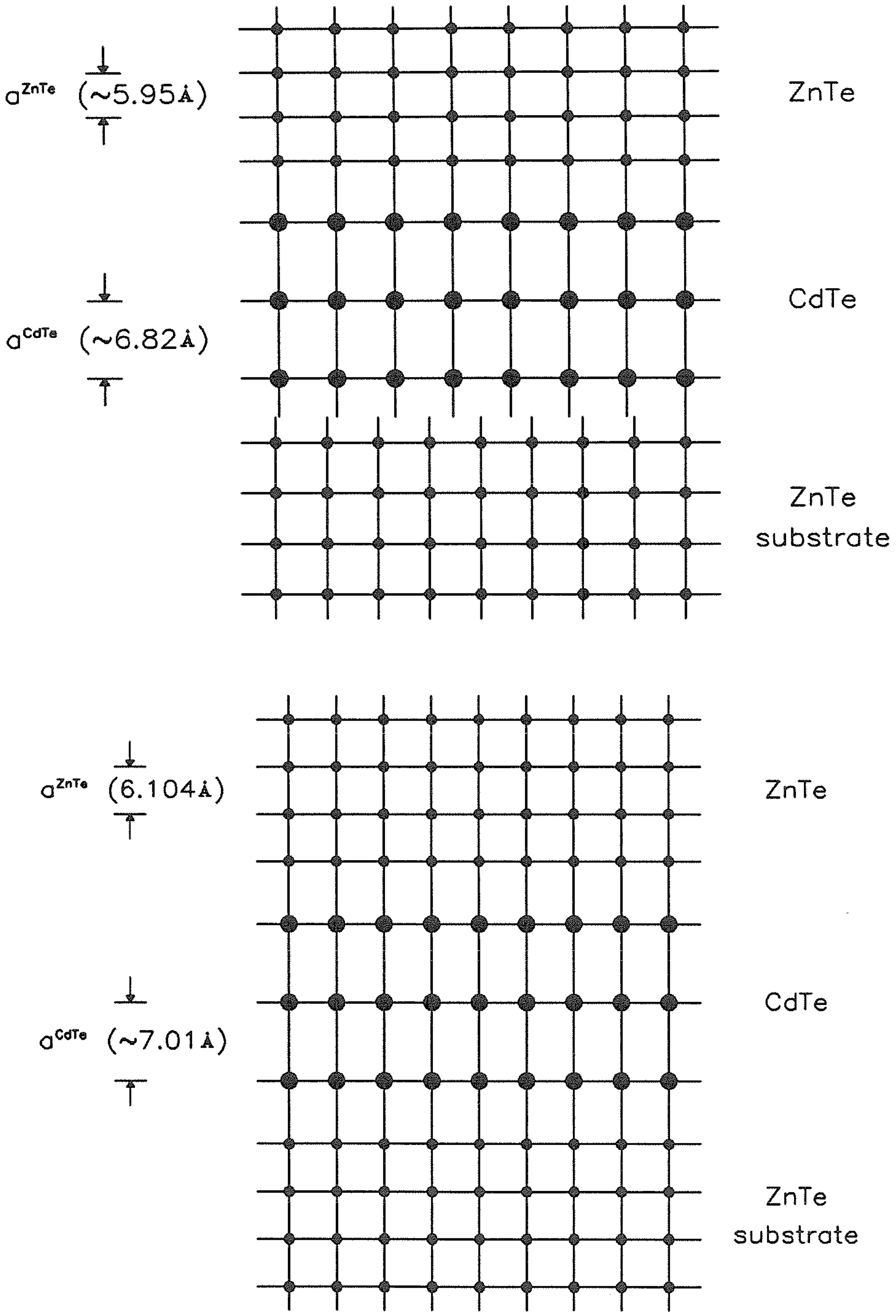

Figure 3.2: Tetragonal distortion in strained CdTe/ZnTe superlattices. (a) Free-standing coherently strained superlattice. (b) Commensurate superlattice, strained to fit a ZnTe buffer layer.

related to in-plane strains ε_{xx} by

$$\varepsilon_{zz}^{A,B} = -2\frac{C_{12}^{A,B}}{C_{11}^{A,B}}\varepsilon_{xx}^{A,B} \tag{3.1}$$

for (100)-oriented superlattices. The growth-direction and in-plane lattice constants ($a_\perp$ and $a_\parallel$, respectively) can then be related to the bulk lattice constants through these strains by

$$a_\parallel^{A,B} = a_0^{A,B}(1 + \varepsilon_{xx}^{A,B}), \tag{3.2}$$

$$a_\perp^{A,B} = a_0^{A,B}(1 + \varepsilon_{zz}^{A,B}). \tag{3.3}$$

Thus, measurement of the growth-direction lattice constants yields the in-plane lattice constants.

If the in-plane lattice constants are identical in the two sets of layers comprising the superlattice, the structure is coherently strained. If a coherently strained superlattice has an in-plane lattice constant equal to that of the topmost buffer layer, the structure is described as commensurate. This is the case illustrated in Fig. 3.2(b). However, this is clearly not the only possible strained configuration. Another case of interest is that in which a superlattice assumes a single in-plane lattice constant that minimizes the elastic energy of the structure, depicted in Fig. 3.2(a). As shown in Section 2.4.1, the in-plane lattice constant that minimizes the elastic free energy of the structure is related to the thicknesses $l_{A,B}$ of the individual layers within the superlattice by

$$a_\parallel = \frac{l_A G^A a_0^{B^2} a_0^A + l_B G^B a_0^{A^2} a_0^B}{l_A G^A a_0^{B^2} + l_B G^B a_0^{A^2}}, \tag{3.4}$$

for bulk lattice constants a_0^A and a_0^B, where

$$G^{A,B} = C_{11}^{A,B} + C_{12}^{A,B} - 2\frac{C_{12}^{A,B^2}}{C_{11}^{A,B}}. \tag{3.5}$$

By revealing the in-plane lattice constants within a superlattice, x-ray diffraction allows the unstrained, free-standing, and commensurate strained cases to be distinguished.

We have chosen to simulate the x-ray diffraction from a superlattice through a kinematical model. This is a good approximation when x-ray penetration depths are long compared to the size of the crystal being analyzed, as is the case in our experiment. Our model neglects effects that are due to superlattice periods consisting of non-integral numbers of monolayers* and variations in superlattice periodicity, as well as effects such as extinction usually incorporated in dynamical models. While these effects have not been modeled simply to date, the dominant effect associated with discrete fluctuations is typically a slight increase in the width and decrease in intensity of observed superlattice x-ray lines. Intuitively, the diffraction expected from a typical imperfect superlattice can be viewed as an incoherent sum of diffraction from layered structures that are subsets of the total superlattice (this incoherent diffraction is characterized by sums in intensity from scattering crystallites, rather than sums in amplitude). This problem has been modeled in detail elsewhere.[4]

In the kinematical approximation, the structure of an x-ray diffraction pattern is calculated by summing contributions from a single unit cell across the extent of the crystal. For the case of growth-direction diffraction from a superlattice, in which each unit cell is composed of several layers of one material followed by several layers of another, the intensity of diffracted x-rays I can be expressed as

$$\begin{aligned} I &\propto \sum_{l} f_l e^{i\vec{k}\cdot\vec{r}^{\,l}} &(3.6)\\ &\propto \left|\left(\sum_{n}^{N} e^{iknL}\right)\left[\left(\sum_{m_A}^{M_A} e^{ikm_A a_A}\right)\left(\sum_{j_A}^{J_A} f_{j_A} e^{ikr_z^{j_A}}\right)+\left(\sum_{m_B}^{M_B} e^{ikm_B a_B}\right)\left(\sum_{j_B}^{J_B} f_{j_B} e^{ikr_z^{j_B}}\right)\right]\right|^2. &(3.7)\end{aligned}$$

In this equation, f_j are the atomic form factors, r_z^j are the growth-direction co-

---

*Superlattice periods not corresponding to integral numbers of monolayers are achieved by fractional layer coverages. Except in the growth technique of atomic-layer epitaxy, interfaces are always associated with partial layer coverages.

ordinates of the atoms in a single unit cell, $a_{A,B}$ are the growth-direction lattice constants of the constituent materials, and L is the length of the superlattice unit cell. The first sum extends over the number of superlattice unit cells N, the second describes a single superlattice cell as a sum over M constituent material unit cells, and the third describes atomic contributions to a standard bulk-like unit cell.

Equation 3.7 can be rewritten as

$$I \propto \frac{\sin^2(NkL/2)}{\sin^2(kL/2)}\left|\text{SUM OVER LAYER A} + \text{SUM OVER LAYER B}\right|^2 . \tag{3.8}$$

From this construction it is apparent that the structure will be dominated by sharp, closely spaced peaks described by $\sin^2(NkL/2)/\sin^2(kL/2)$, which result from the requirement that scattered waves maintain coherence between superlattice unit cells. For superlattices in which the period is short, the diffraction condition arising from a single superlattice unit cell is not a stringent one. In particular, this condition appears as a slow modulation in amplitude of these narrow peaks. The envelope modulating the closely spaced superlattice peaks is illustrated in Fig. 3.3, which compares calculated superlattice diffraction from a single superlattice period with that from a 200-period structure. It should be noted that the slow modulation coming from a single superlattice period (described by the $|\text{LAYER A} + \text{LAYER B}|^2$ term) provides the only information relating to the lattice constants within each layer. While the spacing between narrow peaks yields the period of the superlattice L, the size of the superlattice unit cell is typically unrelated to the lattice constants of the constituent materials. Thus, the positions of the narrow peaks defined by this periodicity carry no information pertaining to these parameters.

Growth-direction lattice constants in the two materials forming the superlattice are only readily deduced if the envelopes associated with diffraction from adjacent layers are separated sufficiently to be distinguished from each other. The widths

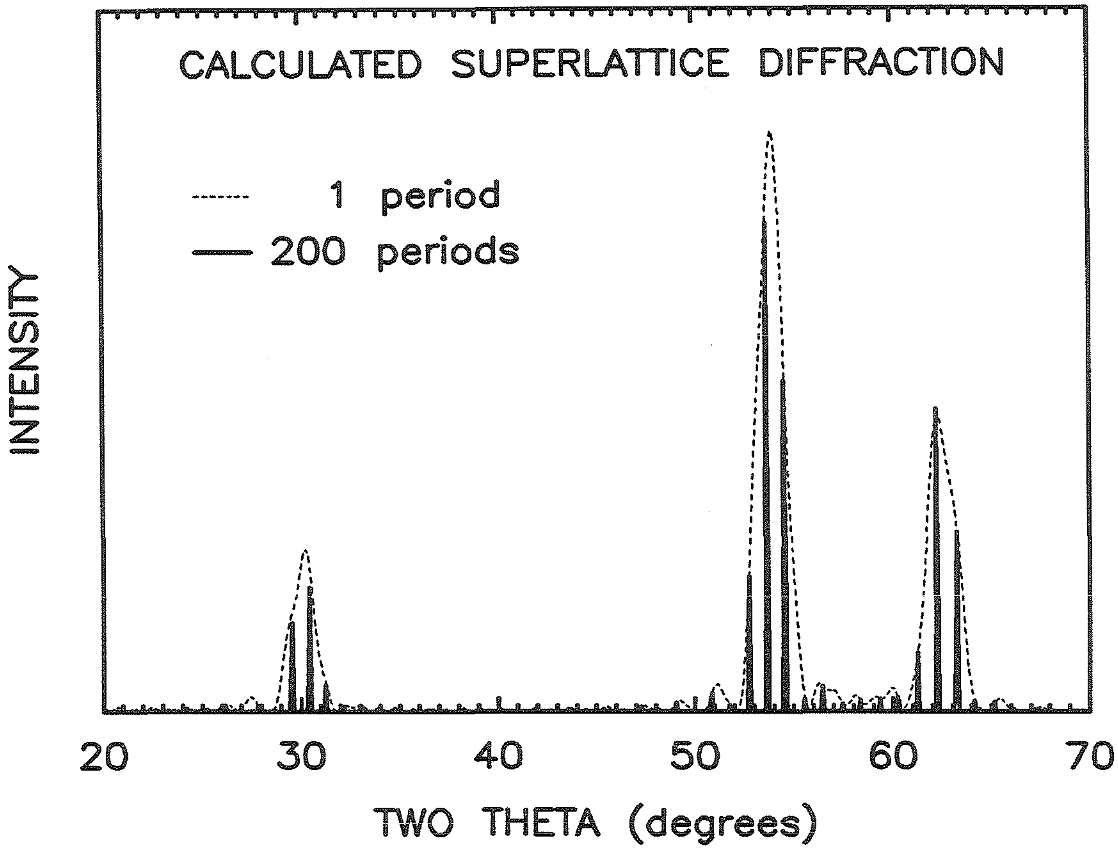

Figure 3.3: $\theta/2\theta$ x-ray diffraction calculated from a single superlattice period and from a 200-period superlattice. The calculation assumed parameters appropriate to a free-standing 56 Å CdTe / 50 Å ZnTe superlattice (*i.e.*, sample 3). Increasing the number of periods yields narrow peaks with amplitudes determined by the single-period diffraction envelope and positions determined by the periodicity of the superlattice.

of these envelopes can be approximated by Scherrer's formula,[5]

$$\theta_{\mathrm{FWHM}} \simeq 0.9\frac{\lambda}{L\cos\theta}, \tag{3.9}$$

where the thickness of each layer of material within a superlattice period is given by $L_{A,B} = M_{A,B}a_{A,B}$. Since positions of the two envelopes can be determined by Bragg's law, we find that constituent lattice constants can be separated only if

$$n\left|\frac{1}{a_A} - \frac{1}{a_B}\right| > 0.9\left(\frac{1}{L_A} + \frac{1}{L_B}\right). \tag{3.10}$$

For the bulk ZnTe and CdTe lattice constants of 6.104 Å and 6.481 Å, $(1/L_A + 1/L_B)^{-1}$ must exceed approximately 20 Å for the [400]-like diffraction peaks to be distinguished. This condition is satisfied only for sample 3; in the remainder of our samples the envelopes can be resolved only if the growth-direction lattice constants deviate substantially from bulk values. As illustrated in Fig. 3.2, such deviations are to be expected in heavily strained lattices.

Figure 3.4 shows calculated x-ray diffraction from a single period of sample 3 for the three cases of free-standing strained growth, growth strained to a CdTe buffer layer, and unstrained growth. Form factors used in these calculations have been taken from Ref. 6. Although the superlattice layers are sufficiently thick to allow two [400]-like envelopes to be distinguished in each case, the spacing of the envelopes increases greatly with the tetragonal distortions resulting from strain. A large offset in the absolute angle at which diffraction occurs distinguishes the free-standing superlattice from one strained to match the CdTe buffer layer.

3.2.2 Results

Diffraction of Cu Kα X rays was measured in a $\theta/2\theta$ arrangement. Since the geometry chosen was symmetric about each sample's growth axis, we were probing lattice constants only in the growth direction. Spectra were accumulated on a

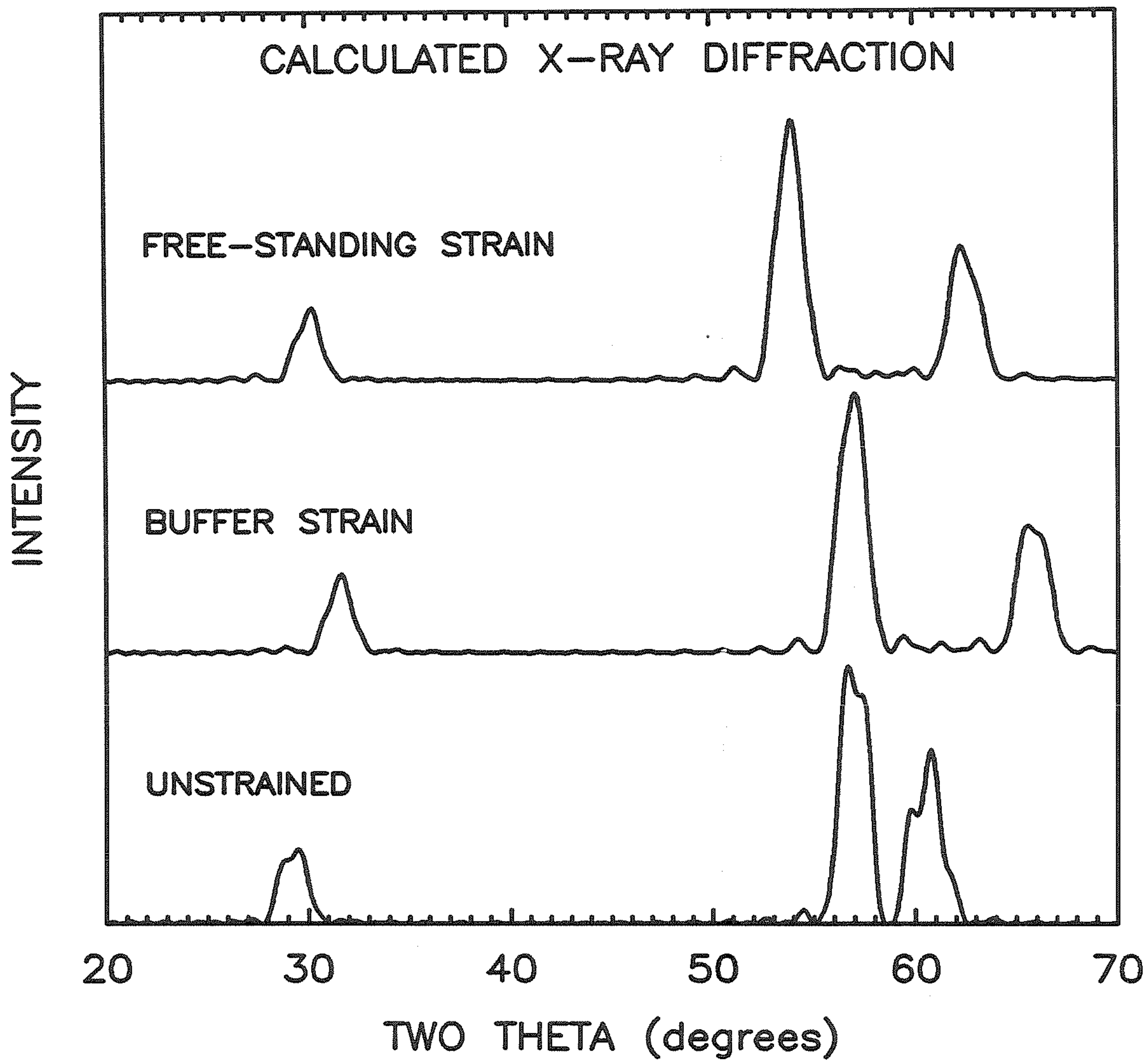

Figure 3.4: X-ray diffraction calculated for a single period of sample 3 under different strain conditions. The degree to which lattice mismatch is accommodated elastically within the superlattice can be inferred from the separation of [400]-like peaks, which increases with tetragonal distortion. Shifts in the absolute angles associated with diffraction distinguish the free-standing structure from the superlattice commensurate with the CdTe buffer layer.

Phillips diffractometer with a Cu source. A Ni foil placed between the sample and source reduced Kβ X rays while passing the Kα lines. Additional scans were gathered on a Siemens D500 Kristalloflex Diffractometer. Contributions from Cu Kβ were not filtered in this setup but were subsequently removed by applying a Rachinger correction[5] to the data.

$\theta/2\theta$ scans revealed [200]−like and [400]−like superlattice peaks (referred to the cubic CdTe or ZnTe unit cells), as well as single peaks attributable to $Cd_xZn_{1-x}Te$ buffer layers and to GaAs substrates. Experimental results have been compared with diffraction calculated from the kinematical model outlined in the previous section. Observed diffraction from CdTe/ZnTe superlattice sample 8, shown in Fig. 3.5, appears to be in excellent agreement with theory when the structure is assumed to be unstrained. The most intense [400]-like superlattice peak is enhanced by the superposition of diffraction from the buffer layer at this angle, but agreement with the unstrained limit is good nevertheless. Figures 3.6 and 3.7 show diffraction representative of the remaining samples. These samples show high levels of residual strain, as evidenced by the appearance of two [400]-like envelopes, but are not in perfect agreement with calculated diffraction appropriate to a coherently strained structure. The envelopes are not separated as much as would be expected for a perfectly strained structure; lattice mismatch appears to accommodated by a combination of misfit defects and elastic strain. However, diffraction envelopes are symmetrically placed about the average lattice constant expected in a free-standing structure; samples grown on CdTe or ZnTe show no evidence of being strained to fit this template, in agreement with the results from photoluminescence described in Chapter 2.

No attempt has been made to perform a quantitative fit to these experimental data by taking the growth direction lattice parameters as free variables. Such fits are of questionable significance once the existence of large defect densities has

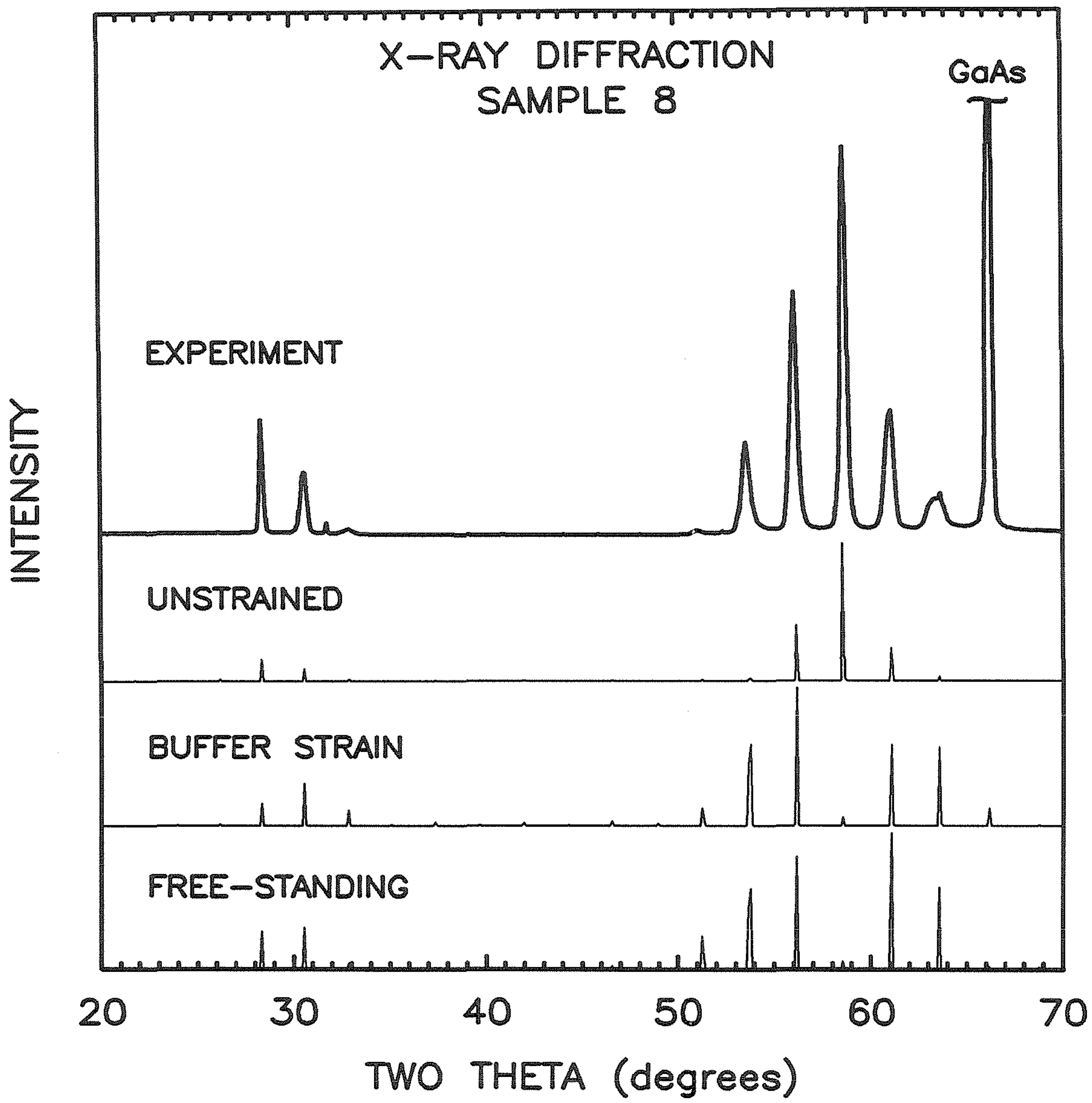

Figure 3.5: $\theta/2\theta$ x-ray diffraction from CdTe/ZnTe superlattice sample 8 showing [200]–like and [400]–like diffraction peaks. The sample was irradiated with Cu Kα X rays. Also shown are diffraction patterns calculated in the kinematical approximation for the cases of unstrained growth, free-standing strained growth, and strained growth commensurate with the $Cd_{0.5}Zn_{0.5}Te$ buffer layer. The truncated peak at 66.1° is due to the GaAs substrate.

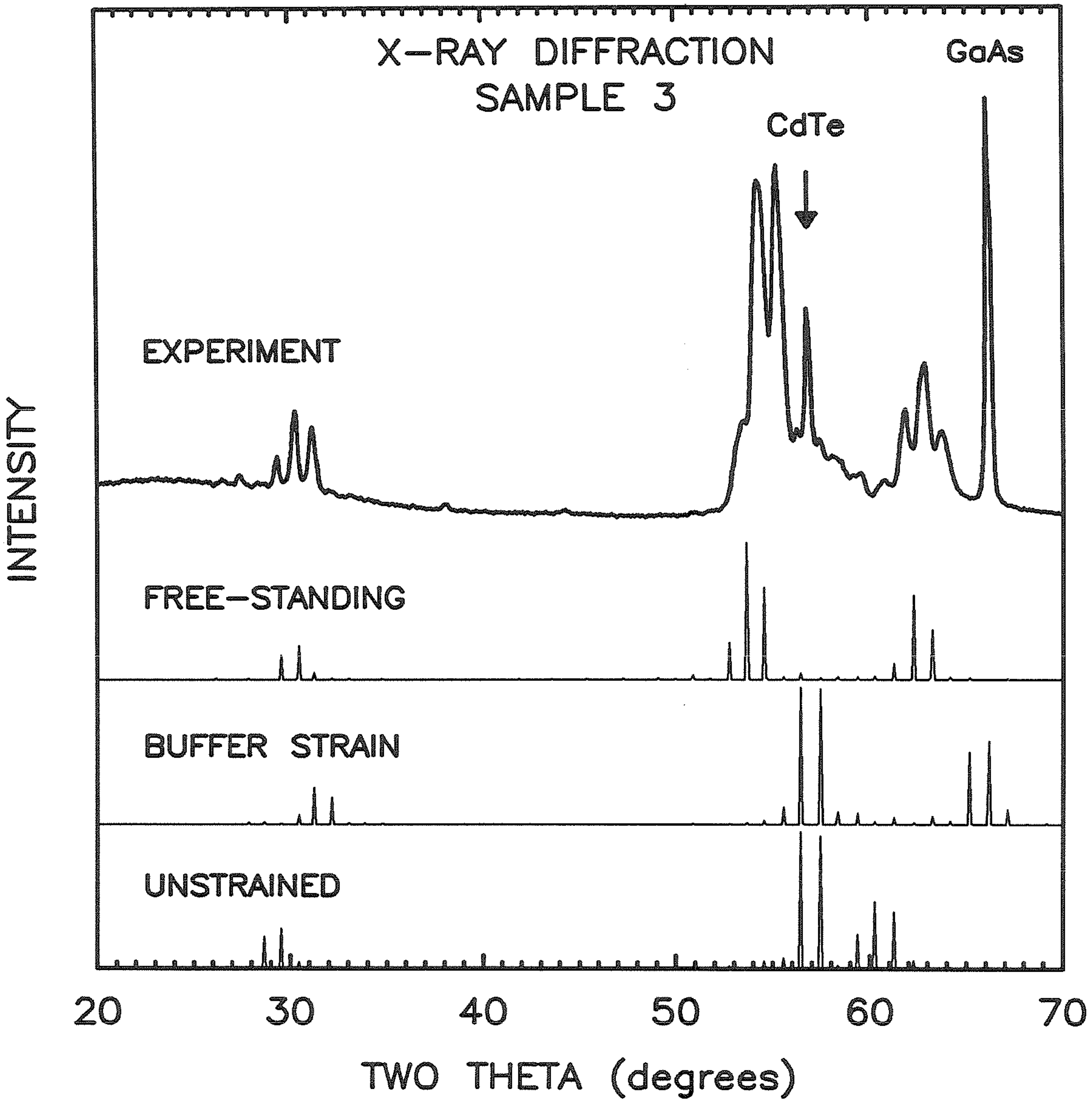

Figure 3.6: $\theta/2\theta$ x-ray diffraction from CdTe/ZnTe superlattice sample 3. [400]–like diffraction peaks are split into two envelopes around $\theta = 58^{\circ}$. Although the splitting is not as great as expected for a coherently strained structure, it indicates high levels of residual strain.

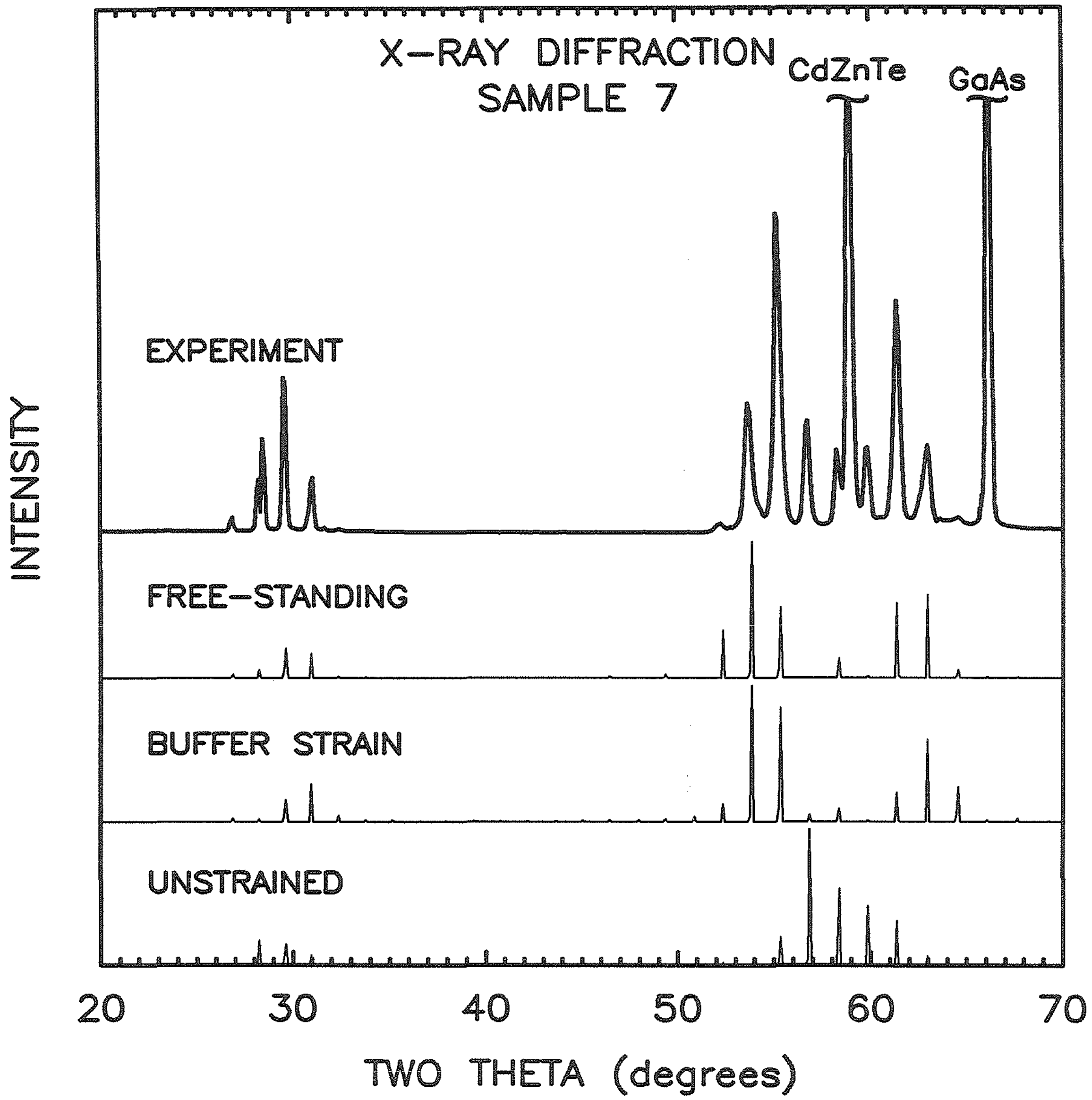

Figure 3.7: $\theta/2\theta$ x-ray diffraction from CdTe/ZnTe superlattice sample 7. Truncated peaks at 66.1° and 58.7° are associated with the GaAs substrate and $Cd_{0.5}Zn_{0.5}Te$ buffer, respectively.

been inferred; x-ray penetration depths are on the order of microns, resulting in diffraction that averages over the extent of the superlattice and over a variety of inhomogeneous strain fields. Although diffraction from defective structures can be modeled with contributions from differently strained crystallites, such a fit to the data is far from unique for a single x-ray diffraction scan.

The x-ray diffraction results can be summarized as follows. None of the samples shows x-ray diffraction expected from a commensurate, coherently strained structure. Diffraction from sample 8 is in good agreement with calculation for an unstrained structure, although contributions from a $Cd_{0.5}Zn_{0.5}Te$ buffer cannot be distinguished from the diffraction from this superlattice and thus improve the apparent fit. The remaining superlattices show evidence of large strain fields. Envelopes associated with diffraction from a single unit cell are placed symmetrically around the average lattice constant expected in a free-standing superlattice; structures grown on pure CdTe or ZnTe show no tendency to maintain the in-plane lattice constant of the buffer layer.

These results are not entirely consistent with expectations from the classical critical thickness theories,[7,8,9,10,11] plotted in Fig. 2.6. Although samples grown on pure CdTe or ZnTe buffer layers are defective, as predicted by the classical limits, superlattices grown on $Cd_{0.5}Zn_{0.5}Te$ buffer layers lie in a more uncertain regime. Sample 8, in particular, appears to satisfy both the individual layer and overall superlattice critical thickness requirements,[12,13,14] but is highly defective. Although the role of fluctuations (*e.g.*, in layer thicknesses) cannot be discounted in samples lying so close to the predicted limits, the discrepancy may be attributed to growth conditions. As shown in Chapter 2, sample 8 appears to have grown in a mode unique amongst the samples studied here. Photoluminescence data described in Section 2.3.3 show evidence of islanding at interfaces within the superlattice, characteristic of growth at slightly increased temperatures.* Regardless of the

---

*In support of this argument, it should be noted that samples 8 and 9 were among the first exact origin of this change, it is clear that factors influencing the growth mode of a superlattice are capable of greatly changing the density and type of defects observed in a particular structure. This observation provided some of the motivation for the $Ge_{0.5}Si_{0.5}/Si$ growth-temperature studies described in Chapter 4.

3.3 *In-situ* RHEED and TEM

Despite the agreement between conclusions drawn from photoluminescence and x-ray diffraction, it was not possible to fully characterize the strains in the superlattices from these experiments alone. Although the structures are clearly highly defective, x-ray diffraction probes large areas of the crystal and consequently is not readily applied to characterizing dislocation networks. TEM [15] and *in-situ* RHEED[16] experiments have been used to further examine the structural quality of CdTe/ZnTe superlattices.

Superlattice epitaxy has been studied during growth through *in-situ* reflection high-energy electron diffraction (RHEED) measurements performed on a single sample. Data were accumulated for a superlattice consisting of 200 repeats of 25 Å CdTe and 25 Å ZnTe grown on a CdTe buffer layer. Spotty RHEED patterns during the first half-micron of growth show that the first 100 superlattice periods grown were highly defective. At this point, however, the RHEED patterns rapidly assume the well-defined streaks characteristic of high-quality two-dimensional epitaxial growth.[16] This change is presumed to be associated with a substantial drop in dislocation density, as expected when strain set by a CdTe buffer is divided into lesser contractions and dilations of adjacent superlattice layers.

RHEED results are consistent with the substantial reduction of defect densities away from the superlattice/buffer-layer interface observed through transmission

---

samples grown, before standard growth conditions were established.

electron microscopy (TEM) of sample 8.[15] Misfit-accommodating 60° dislocations have been observed to drop in density from $10^{10} - 10^{11}\text{cm}^{-2}$ near the first interfaces to $\simeq 10^{8}\text{cm}^{-2}$ near the top surface of the sample. Although these densities are very high, it should be noted that this particular sample appears to be the least strained of the superlattices examined, as shown previously.

3.4 Conclusions

All of our samples have been observed to exceed the critical thickness for the nucleation of misfit-accommodating dislocations. Sample 8, which satisfies the critical thickness criteria imposed by a number of traditional models, appears to show the smallest degree of residual strain. Although layer thickness fluctuations could account for this discrepancy, it is probable that growth conditions played a role in distributing strain in these superlattices. In particular, sample 8 appears to have grown in a mode unique among the samples studied. A mechanism affecting a sample's growth mode could be expected to alter substantially the density and distribution of dislocations in the sample.

Previous experiments confirm the role of temperature in nucleating dislocations. Annealing studies of Ge_xSi_{1-x} superlattices have demonstrated the metastable nature of these structures.[17] In particular, annealing at temperatures higher than those typically used during MBE growth results in the formation of substantial numbers of defects in these structures. It should not be surprising that such a system might be sensitive even to small changes in growth conditions. Consideration of growth parameters should be important in predicting the critical thickness associated with a particular sample. While Van der Merwe's model[8] presents a plausible lowest-energy state for greatly strained structures, the degree to which a sample displays a critical thickness in agreement with this prediction depends on its ability to acquire the activation energy necessary to reach this state.

The structure of a number of CdTe-ZnTe superlattices has been examined. Each of the samples studied has been grown beyond the critical thickness for generation of misfit defects, in disagreement with predictions based on extrapolations from empirical single-film critical thicknesses to those of superlattices. Our data suggest that growth conditions play a role in determining the onset of defect formation, in contrast to the assumptions behind current critical-thickness models. Defect densities drop dramatically within a micron of the superlattice/buffer-layer interface, regardless of the buffer layer used. While the resulting epitaxy is far from defect-free, identifying the mechanisms responsible for inhibiting defect formation should be valuable for future device applications.

References

1. M. D. Camras, J. M. Brown, N. Holonyak, Jr., M. D. Nixon, R. W. Kaliski, M. J. Ludowise, W. T. Dietze, and C. R. Lewis, *J. Appl. Phys.* **54**, 6183 (1983).
2. H. Jung, A. Fischer, and K. Ploog, *Appl. Phys. A* **33**, 97 (1984).
3. G. Monfroy, S. Sivananthan, X. Chu, J. P. Faurie, R. D. Knox, and J. L. Staudenmann, *Appl. Phys. Lett.* **49**, 152 (1986).
4. B. M. Clemens and J. G. Gay, *Phys. Rev. B* **35**, 9337 (1987).
5. H. P. Klug and L. E. Alexander, *X-Ray Diffraction Procedures For Polycrystalline and Amorphous Materials* (Wiley, New York, 1974).
6. *International Tables for X-ray Crystallography*, edited by C. H. MacGillavry and G. D. Rieck (Kynoch, Birmingham, 1963).
7. R. People and J. C. Bean, *Appl. Phys. Lett.* **47**, 322 (1985); **49**, 229(E) (1986).
8. J. H. Van der Merwe, *J. Appl. Phys.* **34**, 123 (1963).
9. C. A. B. Ball and J. H. Van der Merwe, in *Dislocations in Solids, Volume 6*, edited by F. R. N. Nabarro (North Holland, Amsterdam, 1983), p. 122.
10. J. W. Matthews and A. E. Blakeslee, *J. Cryst. Growth* **27**, 118 (1974); **29**, 273 (1975); **32**, 265 (1976).

11. J. W. Matthews, in *Epitaxial Growth, Part B*, edited by J. W. Matthews (Academic, New York, 1968).
12. J. C. Bean, in *Silicon Molecular Beam Epitaxy*, edited by E. Kasper and J. C. Bean (Chemical Rubber, Boca Raton, FL, 1987).
13. M. Y. Yen, A. Madhukar, B. F. Lewis, R. Fernandez, L. Eng, and F. J. Grunthaner, *Surf. Sci.* **174**, 606 (1986).
14. T. C. Lee, M. Y. Yen, P. Chen, and A. Madhukar, *Surf. Sci.* **174**, 55 (1986).
15. P. M. Petroff, unpublished.
16. G. Monfroy, X. Chu, M. Lange, and J. P. Faurie, unpublished.
17. A. T. Fiory, J. C. Bean, R. Hull, and S. Nakahara, *Phys. Rev. B* **31**, 4063 (1985).

Chapter 4

Dislocation Formation in $Ge_{0.5}Si_{0.5}/Si$ Superlattices

4.1 Introduction

4.1.1 Background

This chapter describes studies of the effect of growth temperature on stress relaxation in lattice-mismatched superlattices. As discussed in Section 1.4.2, much work has been devoted to the prediction and measurement of the critical thickness beyond which a thin film breaks away from a substrate to which it is poorly lattice-matched. The importance of this limit has been recognized for some time; while coherent strain can be an effective parameter in tailoring the properties of a lattice-mismatched device,[1] structural defects associated with stress relaxation can seriously degrade device performance.[2] Traditional critical thickness theories are in poor agreement with each other, however, as illustrated in Fig. 1.9 for the case of $Ge_xSi_{1-x}$and in Fig. 2.6 for $Cd_xZn_{1-x}Te$. In addition, there is little agreement between experimentally determined critical thicknesses, although the traditional theories span a sufficiently large range that agreement with one of the models is usually claimed.

While some of the variation in reported critical thicknesses can be ascribed to the different sensitivities of various techniques to misfit dislocations, identical methods sometimes give substantially different results.[3] Discrepancies between observed critical thicknesses have been attributed to a number of factors. It has been suggested that different structures (*i.e.*, single films, quantum wells, superlattices, etc.) display different critical thicknesses. Structures composed of different materials with dissimilar elastic properties clearly display different limits. Recently, there have been suggestions that variations in the reported critical thicknesses might be a consequence of differences in growth conditions.[4,5,6,7] In this study we examine the role of growth conditions in relieving stresses that are due to lattice mismatch.

We have chosen to examine growth-temperature variations in $Ge_{0.5}Si_{0.5}/Si$ superlattices. Structures composed of Ge_xSi_{1-x} have recently attracted attention for use in a variety of applications. Heterojunction bipolar transistors (HBT's) fabricated from coherently strained layers have been shown to display current gains superior to those of traditional HBT's.[8,9,10] Improvements in speed and gain are related to strain-induced splitting of the conduction band, which reduces the effective mass for transport in the growth direction while also inhibiting intervalley scattering associated with phonons. Modulation-doped field-effect transistors (MODFET's) have also been shown to benefit from a high-mobility Ge_xSi_{1-x} channel.[11] In addition to the interest generated by Ge_xSi_{1-x} HBT's and MODFET's, optical effects have recently brought attention to Ge_xSi_{1-x} superlattices. The electronic band structure of superlattices is such that band extrema located away from the zone center for bulk material can, in certain cases, be folded into the Γ-point, yielding a "quasi-direct" band gap. Although the symmetries of the conduction- and valence-band states may still limit the oscillator strengths obtainable in such a superlattice, such a band structure allows radiative decays across the band gap without the involvement of phonons. The possibility of integrating Ge_xSi_{1-x} light emitters or modulators on a chip has stimulated a variety of experimental[12,13] and theoretical[14,15,16] studies into the optical properties of these structures. While no efficient light emission has been demonstrated to date, high photoconductive gains have brought attention to Ge_xSi_{1-x}/Si superlattices as long-wavelength photodetectors.[17]

In addition to being of technological interest, the Ge_xSi_{1-x} system is particularly well suited to a growth temperature study of strain. Unlike many compound semiconductors, Ge and Si can be grown epitaxially over a wide range of temperatures (single-crystal MBE growth temperatures range from approximately 300 °C to 1000 °C). Strain effects are large in this system; bulk Ge has a lattice constant of 5.658 Å, whereas that of Si is 5.431 Å, yielding a net mismatch of 4.2%. Much experimental work has been devoted to measuring the critical thicknesses imposed by this mismatch.[6,18,19]

4.1.2 Results of this work

We demonstrate the dependence of stress relaxation on growth temperature in a lattice-mismatched epitaxial system. Strains have been measured for $Ge_{0.5}Si_{0.5}/Si$ superlattices grown by MBE on (100)-Si substrates at temperatures between 330 °C and 530 °C. The accommodation of lattice mismatch by elastic strain has been determined through x-ray diffraction, channeled RBS, and TEM. Lattice mismatch is found to be accommodated elastically in a structure grown at 365 °C, with a dislocation density too low to be resolved by TEM ($< 10^5 cm^{-2}$). Samples grown at higher temperatures display greater numbers of misfit-accommodating dislocations, with the density of dislocations reaching $1.5 \times 10^5 cm^{-1}$ at a growth temperature of 530 °C. This growth-temperature dependence may account for inconsistencies in critical thickness data reported in the literature. Although equilibrium critical thicknesses may be adequately described by bulk material properties, these limits do not adequately describe films frozen in metastable states. Our results clearly demonstrate the need to account adequately for the kinetics of defect formation in the prediction of critical thicknesses.

4.1.3 Outline of chapter

The $Ge_{0.5}Si_{0.5}/Si$ superlattice samples used in this study are described in Section 4.2. Details pertaining to the growth of the samples are presented, as precise conditions appear to play a major role in the process of defect formation. Section 4.3 details the results of x-ray diffraction, TEM, and channeled RBS studies of the strain distributions within the superlattices. Attention is paid to the sensitivities of the various techniques to different densities of defects, as this has become a controversial issue in the measurement of critical thicknesses. Observed growth-temperature dependences are discussed in the context of models describing the onset of dislocation formation in Section 4.4. The results are summarized in Section 4.5.

4.2 Samples

Compositionally identical $Ge_{0.5}Si_{0.5}/Si$ samples were grown in a modified III-V Perkin-Elmer MBE machine at temperatures between 330 °C and 530 °C. Growth temperatures were inferred from optical pyrometer and thermocouple readings, calibrated with the aid of eutectic reactions observed *in situ*. We estimate our growth temperatures to be accurate to within 20 °C. (100)-oriented Si substrates were cleaned following a modified Shiraki procedure[20,21] consisting of repeated *ex situ* oxide growths and etches. This was followed by a final oxide desorption at 800 °C in the growth chamber under ultrahigh vacuum (UHV) conditions. The cleaning procedure was followed by growth of an epitaxial Si buffer layer (≈ 1000 Å in thickness), during which the growth temperature was lowered continuously from 700 °C. Superlattices fabricated at higher temperatures (530 °C) were grown without interruption on the Si buffer layers. Growth at temperatures lower than this required an interruption of less than 30 minutes after deposition of the buffer layer to allow the substrate to cool further. The superlattice layers were grown by codeposition of Si and Ge at feedback-stabilized deposition rates of 1 Å/sec, independent of the growth temperature.

In situ reflection high-energy electron diffraction (RHEED) patterns show that the growth becomes single-crystal at a temperature of 300 °C. TEM confirms the single-crystal nature of our superlattices. We did not observe any polycrystalline growth. Previous work had suggested "amorphous or disordered growth"[22] at 400 °C under certain circumstances and poor channeling yields under others. We saw no evidence of either of these in our films.* The reason for this discrepancy is not clear at this point, although it should be noted that the substrate cleaning procedure used here is substantially different from the sputter and anneal technique used in the previous study.[22]

Superlattice characteristics are listed in Table 4.1. Four samples were grown with identical layer thicknesses, compositions, and numbers of superlattice periods. Growth temperature alone was varied between these samples. Two other superlattices (SL 29 and SL 37) were grown, at temperatures of 330 °C and 530 °C. Although the defect densities observed in these samples are consistent with results obtained from the other four samples, the different number of periods makes it impossible to isolate growth temperature conclusively as the cause of observed differences. X-ray diffraction measurements have confirmed the superlattice periods

---

*Discrepancies such as these highlight the difficulties associated with comparisons of data taken from different sources. Although data exist for Ge_xSi_{1-x} critical thicknesses at growth temperatures of 550 °C[18] and 750 °C,[23] it is not clear that these data are comparable.

Table 4.1: $Ge_{0.5}Si_{0.5}/Si$ superlattice samples.

Sample	Layer Thicknesses $Ge_{0.5}Si_{0.5}/Si$ (Å)	Periods	Growth Temp. (°C)	(Reference No.)
SL 78	65/65	36	365	(SL 87.078)
SL 71	65/65	36	390	(SL 87.071)
SL 77	65/65	36	450	(SL 87.077)
SL 72	65/65	36	530	(SL 87.072)
SL 29	70/70	34	330	(SL 87.029)
SL 37	70/70	50	530	(SL 87.037)

to be within ±5 Å of the quoted values. Rutherford backscattering spectroscopy (RBS) shows a random variation in Ge content of $< 5\%$ from intended fractions.

4.3 Experimental

Numerous experimental methods are available for the measurement of strain or dislocation densities in a thin film. Sensitivity of the various methods to different levels of coherent strain has recently led to substantial debate over the accuracy of measured critical thicknesses.[24] The following is a short summary of some common techniques.

Methods commonly employed to measure dislocation densities are TEM, cathodoluminescence, photoluminescence, and etch-pit density measurements. TEM is the only one of these techniques capable of resolving densely packed grids of dislocations. However, the technique is of limited use at low dislocation densities (below approximately 10^5cm^{-2}), and sample preparation procedures are capable of introducing damage into the specimen under study.[25] The remaining methods have been applied exclusively at low dislocation densities ($< 10^5\text{cm}^{-2}$). The luminescence methods are preferable to the etch-pit density measurements in being relatively nondestructive, but rely on optically active dislocations.

Lattice distortions are commonly examined directly by high-resolution TEM, x-ray diffraction, and channeled RBS. Each of these methods is insensitive to low levels of dislocations but provides a measurement of the compressions and dilations associated with stresses that are due to lattice mismatch. Channeled RBS is particularly useful for identifying depths at which the lattice distortions change, whereas x-ray diffraction yields lattice parameters averaged over a substantial penetration depth (typically $\simeq 10\,\mu\text{m}$). Recently, RHEED oscillations have been shown to drop dramatically during growth of a strained film.[6,7] While the precise interpretation of this drop is not certain at this point, this method appears to promise an excellent *in situ* determination of changes in growth mode.

Miscellaneous methods that measure effects arising from strain include Raman scattering, spatially resolved absorption spectroscopy, and luminescence. Techniques relating to optical absorption and photoluminescence can be used to track changes in electronic band structure with strain (see Chapter 2). These shifts are then translated into strains through deformation potentials. Although typically suffering from low signal levels, the technique of Raman scattering benefits from displaying large relative shifts in phonon frequencies with changing strain.

We have chosen to measure strain distributions and dislocation densities within the superlattices by x-ray diffraction, channeled RBS, and TEM. The "low-resolution" techniques of x-ray diffraction and channeled RBS are particularly useful for tracking the relaxation of strains, whereas TEM has been used to identify densities and types of defects present in the superlattices. The results have been recently corroborated by Raman experiments, which have provided independent confirmation of sample compositions and strains.[26]

4.3.1 X-ray Diffraction

Growth-direction lattice constants $a_\perp^{\mathrm{Si}}$ and $a_\perp^{\mathrm{Ge_{0.5}Si_{0.5}}}$ of the Si and $\mathrm{Ge_{0.5}Si_{0.5}}$ layers within the superlattices have been inferred from x-ray diffraction. Since elasticity theory relates $a_\perp$ to the biaxial strain within a layer,[27] measurements of the growth-direction lattice constants reveal the degree to which lattice mismatch has been accommodated elastically within the superlattices.

X-ray diffraction scans were taken in a $\theta/2\theta$ geometry symmetric about the growth direction. Data were accumulated on a Siemens D500 Kristalloflex Diffractometer using a Cu source. A Rachinger correction[28] was used to isolate contributions from the Cu Kα lines by removing those that were due to Kβ. X-ray diffraction from samples SL 29 and SL 37 are compared in Fig. 4.1. With the exception of the single intense peak associated with the Si substrate, structure in the experimental curves is due to [400]-like diffraction from the superlattices (the [400] designation is referred to the standard Si or Ge cubic unit cells). The experimental diffraction consists of narrow peaks modulated by broad envelopes. In our scans, the widths of the narrow peaks are determined by instrumental resolution.

As shown in Chapter 3, the positions of the narrow peaks yield the period of the superlattice, while the growth-direction lattice constants within the structure are inferred from the broad envelopes modulating these peaks. The kinematical model described in Section 3.2.1 has been used to calculate the diffraction expected from a single period of a coherently strained superlattice. This calculated pattern is shown in Fig. 4.1 (indicated by dashed lines). Form factors used in the model were taken from Ref. 29. As can be seen from the figure, the observed diffraction is in excellent agreement with the envelope calculated under the assumption of coherent strain

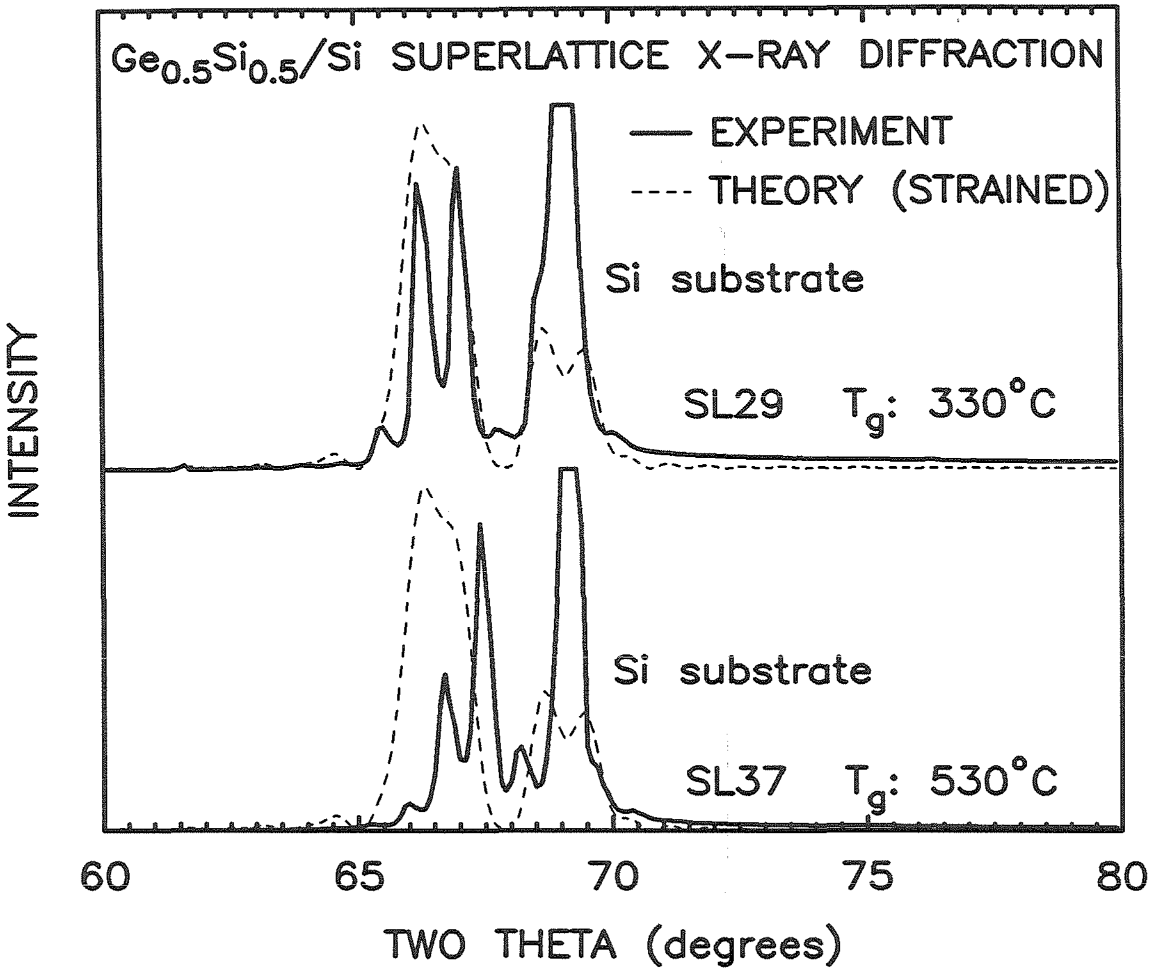

Figure 4.1: [400]-like x-ray diffraction from $Ge_{0.5}Si_{0.5}$/Si superlattice samples SL 29 and SL 35. Experimental (solid) curves are compared with theoretical (dashed) envelopes calculated under the assumption of coherent strain set by the Si substrate. Sample SL 35, grown at 530 °C, has clearly undergone substantial relaxation, whereas SL 29, grown at 330 °C, appears to be coherently strained (within the resolution limit of x-ray diffraction).

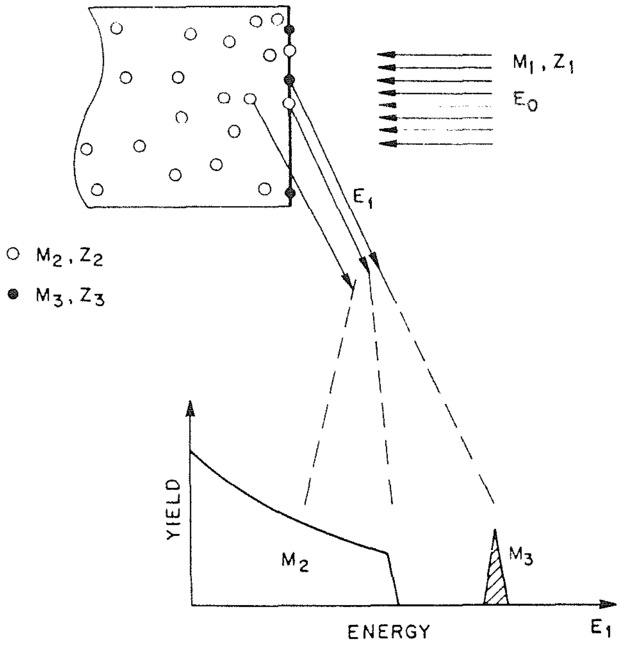

Figure 4.2: Basic Rutherford Backscattering process, in which ions from an incident beam are backscattered with energies characterizing the type and depth of atoms within a solid. From Ref. 30.

when the growth temperature is 330 °C. However, raising the growth temperature to 530 °C results in diffraction in poor agreement with these calculations. Whereas the sample grown at the higher temperature displays substantial strain relaxation, the superlattice grown at 330 °C appears to be coherently strained, to within the resolution of x-ray diffraction.

4.3.2 Channeled RBS

Rutherford Backscattering Spectroscopy is commonly applied in studies of depth-resolved composition and strain profiles of thin films.[30,31] The basic processes involved in the method are depicted in Figs. 4.2 and 4.3. Energetic (MeV)

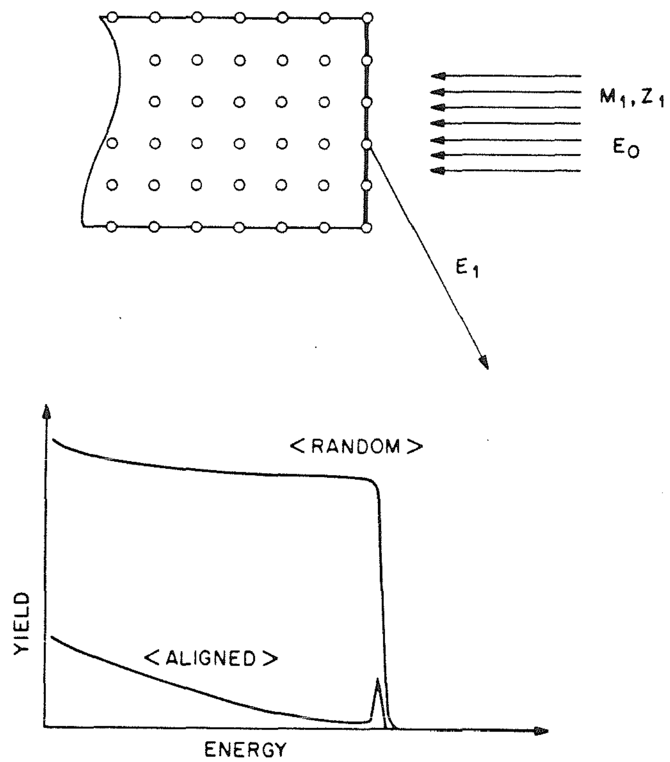

Figure 4.3: Comparison of a channeled RBS spectrum, accumulated for a beam incident along a high-symmetry crystallographic direction, and a spectrum accumulated along an arbitrary (random) direction. From Ref. 30.

ions incident upon a crystal occasionally scatter elastically off atomic nuclei ($\sigma_n \simeq 10^{-24}\mathrm{cm}^{-2}$), transferring an amount of energy that is determined by the scattering geometry, masses of the incoming and scattering particles, and energy of the incident beam. Since the amount of energy transferred is dependent upon the mass of the scattering nucleus, it is possible to identify the elements present in a film by monitoring the energies of ions backscattered at a particular angle from a monoenergetic incident beam. Depth profiling of the composition is also possible, since incident and scattered ions lose energy to high-cross-section ($\sigma_e \simeq 10^{-16}\mathrm{cm}^{-2}$)

electronic excitations as they pass through a sample. Structural information can be obtained by aligning the incident beam with a crystallographic "channel." Although some of the beam is scattered at the surface of the crystal, ions entering along high-symmetry crystallographic directions are effectively channeled, experiencing nuclear scattering events only occasionally if the crystal is of high quality.

Previous studies have made extensive use of channeled RBS for determining the crystalline quality and critical thicknesses of Ge_xSi_{1-x} films.[22,32] By independently monitoring Ge and Si backscattering rates while rocking a sample away from the growth direction, it is possible to identify differences in channeling directions within adjacent layers. These directions are determined by the alternating growth-direction compression and dilation within a strained film; identifying off-growth-axis minima associated with the elements in each set of layers reveals the degree of tetragonal distortion, and hence coherent strain, within the layers. The perfection of a particular sample can also be inferred by examining scattering from an incident beam aligned with the growth axis. In particular, the presence of misfit-accommodating dislocations can be expected to increase backscattering substantially.

Channeled RBS spectra have been obtained for each of our superlattices with an incident 2.275 MeV $^4He^{2+}$ beam aligned with the [100] growth direction. These have been compared with "random" spectra taken with the beam impinging upon samples rotating about the growth axis and tilted off the high-symmetry crystallographic directions. As illustrated in Fig. 4.4, the backscattered yield drops sharply as the growth temperature is lowered to 365 °C. The rapid rise in counts behind the Si surface peak (at $\simeq$1.25 MeV) for the samples grown at 450 °C and 530 °C is indicative of a large number of structural defects. Sample SL 71, grown at 390 °C, shows no great increase in backscattering yield until the interface with the Si buffer layer ($\simeq$ 1.05 MeV). The counts rise dramatically at this point, however, indicating

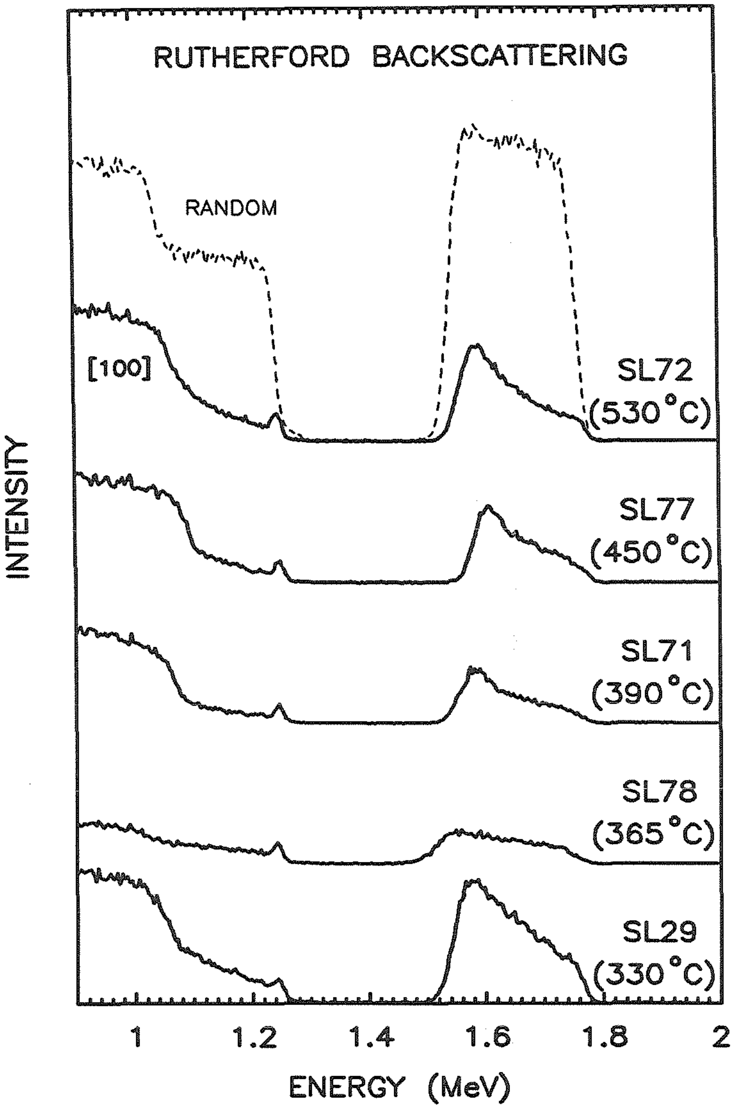

Figure 4.4: Channeled Rutherford Backscattering spectra (solid curves) for superlattice samples grown at temperatures between 330 °C and 530 °C. Spectra were accumulated at 168° with respect to the incident 2.275 MeV $^4He^{2+}$ beam, which was aligned with the [100] growth axis. Backscattered yield below the Si surface peak (around 1.25 MeV) rises substantially as the growth temperature is increased, indicating an increase in the density of structural defects. An unchanneled RBS spectrum for sample SL72 (dashed curve) is shown for comparison. Spectra are plotted on the same scale but are displaced vertically for clarity.

Table 4.2: $Ge_{0.5}Si_{0.5}/Si$ superlattice χ_{min}'s. Total scattering from the films is also shown, indicated as a percentage of backscattered yield from the rotating random scans over the same range of energies.

Sample	Growth Temperature	χ_{min} (%)	Film Scattering (%)
SL 29	330	13.8	29.4
SL 78	365	6.5	10.2
SL 71	390	4.9	14.5
SL 77	450	6.8	19.4
SL 72	530	8.8	25.4
SL 37	530	14.5	39.8

a great number of defects near this first superlattice interface. Superlattice SL 78, grown at 365 °C, is unique in showing a low backscattering yield throughout the film. The structure grown at 330 °C, although observed through x-ray diffraction to be highly strained, shows very poor channeling, indicative of a high number of defects incapable of relieving stresses arising from lattice mismatch.

Values of χ_{min} have been calculated for each of our superlattices by determining the ratio of counts in the channeled spectrum to counts in the unchanneled spectrum at an energy just behind the surface peak. Experimental values are listed in Table 4.2. For comparison, χ_{min} is expected to be approximately 3.5% in high-quality Si or Ge, with scattering resulting primarily from thermal motion of atoms.[32] With the exception of samples SL 29 and SL 78, our χ_{min}'s increase monotonically with growth temperature and sample thickness, as expected. The structure grown at 330 °C, although observed through x-ray diffraction to be highly strained, shows very poor channeling. These results are consistent with the observation from TEM of numerous dislocations threading through this film. The origin of the comparatively poor χ_{min} obtained for SL 78 is not apparent at this point, although total backscattered yield from this film is the lowest. Whether high levels of coherent strain can increase densities of localized defects (such as point defects) sufficiently to account for this high value of χ_{min} is unclear.

4.3.3 TEM

Several of our samples have been examined through cross-sectional and plan-view TEM to identify the types and densities of dislocations present in the superlattices. Figure 4.5 shows a dark-field plan-view image taken from SL 37, grown at 530 °C. A network of misfit-accommodating dislocations is clearly visible, at a density of approximately $1.5 \times 10^5 \mathrm{cm}^{-1}$. Etching away the top half of the superlattice has no significant effect on the dislocation density, which is consistent with the suggestion from channeling and from previous studies[4] that misfit defects are often confined to the first superlattice interfaces. Plan-view studies of SL 78, grown at 365 °C, reveals no such network of misfit dislocations, nor any appreciable number of threading dislocations. Considering the area examined, the misfit dislocation density in this sample is $< 10^5 \mathrm{cm}^{-2}$. Plan-view TEM of sample SL 29, grown at 330 °C, also reveals no network of misfit dislocations but shows poor surface morphology. A cross-sectional micrograph taken from this superlattice is shown in Fig. 4.6. Although the sample appears to be single-crystal, a large number of dislocations thread from the superlattice/buffer-layer interface to the surface of the sample. In addition, while the first superlattice layers appear to be quite planar, the morphology degrades higher in the superlattice, resulting in a poor top surface. This sample is unique in showing a high density of threading dislocations.

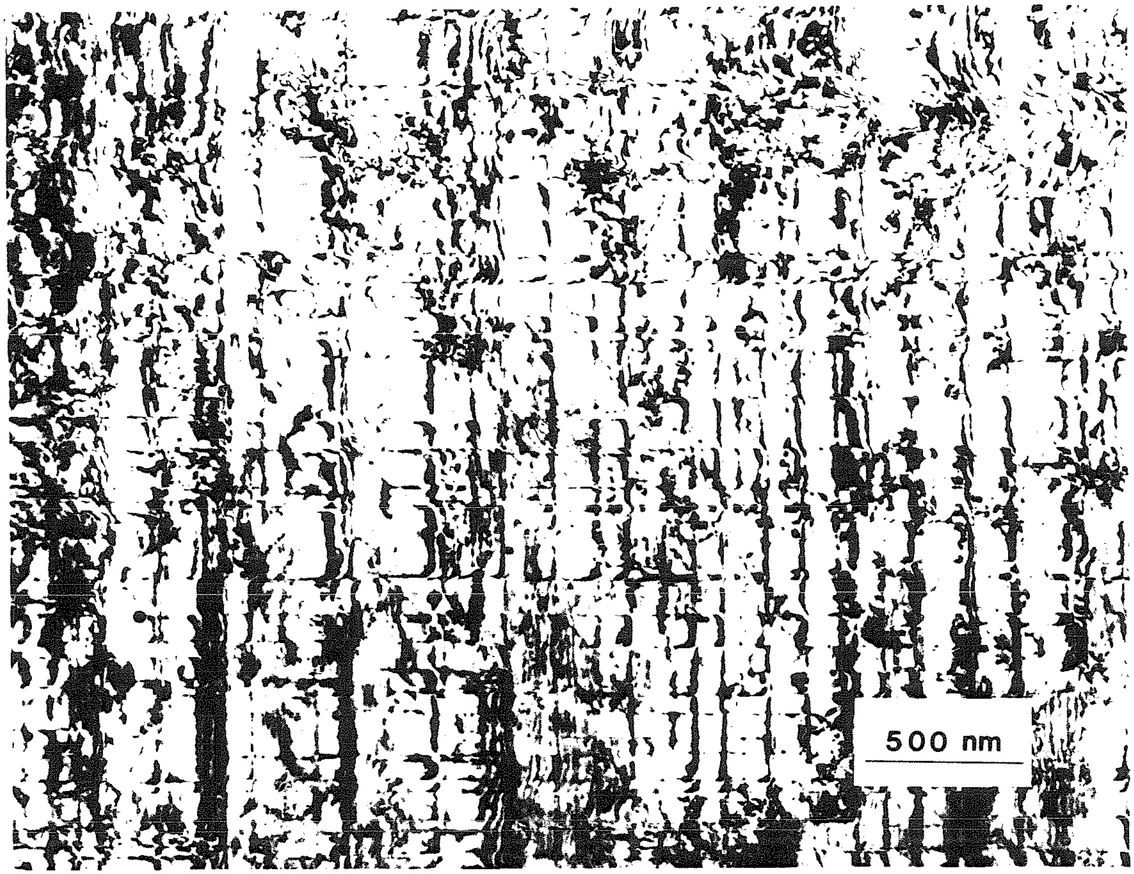

Figure 4.5: Bright-field plan-view TEM image of sample SL 37, grown at 530 °C, showing a network of misfit dislocations lying near the Si buffer-layer/superlattice interface. The dislocation density is approximately $1.5 \times 10^5 \mathrm{cm}^{-1}$.

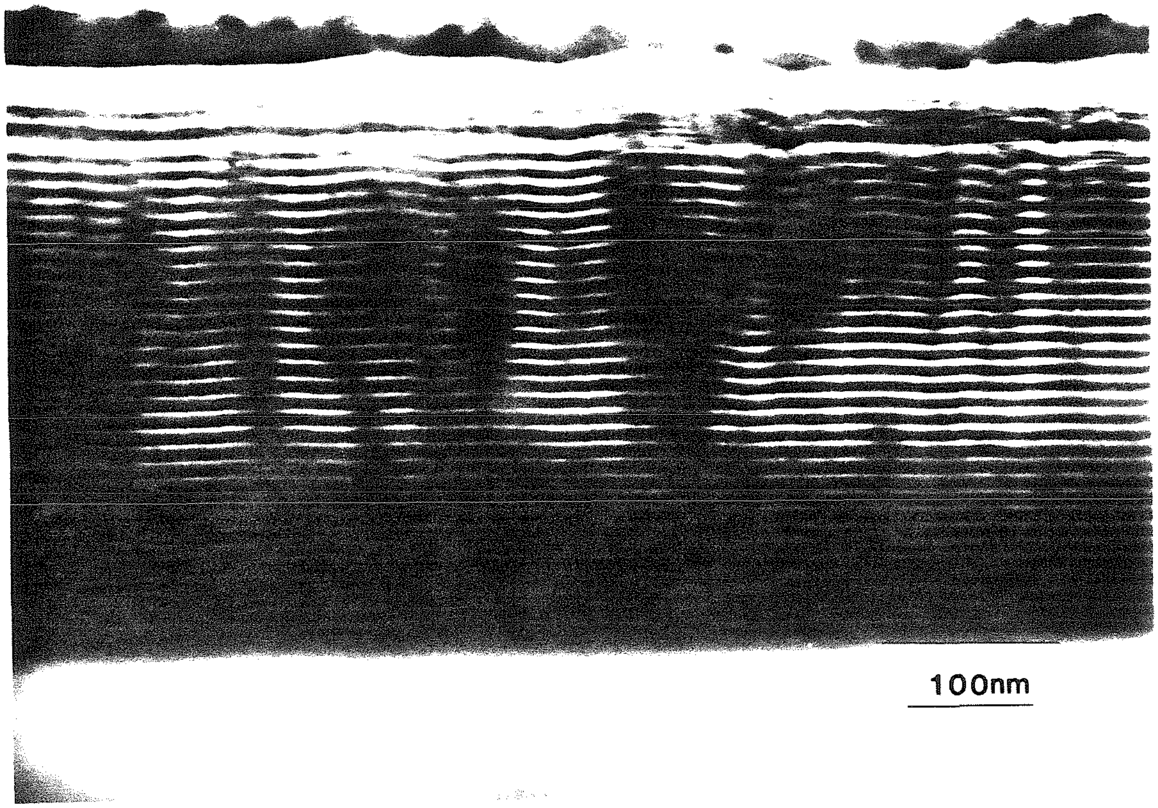

Figure 4.6: Cross-sectional TEM micrograph of sample SL 29, grown at 330 °C. Although superlattice layers near the Si buffer layer are quite planar, the morphology degrades considerably near the top surface. Note also the high density of threading dislocations.

4.4 Discussion

The experimental results can be summarized as follows. We observe single-crystal growth above 300 °C. Superlattice SL 29, grown at 330 °C, accommodates lattice mismatch primarily through elastic strain. This sample displays a high number of threading dislocations, however. The structure grown at 365 °C (SL 78) shows excellent surface morphology and a defect density too low to be detected by TEM ($< 10^5 \mathrm{cm}^{-2}$). As the growth temperature is increased to 530 °C, the superlattices display monotonically increasing densities of structural defects, with misfit dislocation densities reaching $1.5 \times 10^5 \mathrm{cm}^{-1}$ for SL 37, grown at 530 °C.

Our results clearly demonstrate that the appearance of misfit dislocations is strongly dependent on growth conditions. The nature of this temperature-driven process is not clear at present. Examination of the mismatch between the thermal expansion coefficients of Ge and Si shows that the changes we observe cannot be attributed solely to bulk thermal contractions and expansions. Differences in thermal expansion coefficients[33] strain samples at 530 °C by an additional 0.03% compared to those at 330 °C. As the lattice mismatch for Ge grown on Si is 4.2%, this temperature effect is equivalent to a change in Ge fraction of less than 1% (*i.e.*, consideration of thermal expansion coefficients suggests that a superlattice at 530 °C will be under less stress than a superlattice with a 1% greater Ge fraction at 330 °C). Thus, the effect of thermal expansion coefficients is very small, and is more than compensated by the spread in composition of our samples, which exceeds 1%. Ge-rich structures grown at low temperatures display lower defect densities than less-stressed samples grown at higher temperatures. Thus, the temperature activation we observe is more likely associated with dislocation nucleation, glide, or interaction. The precise nature of the process is currently under study.

Comparison with theoretical critical thicknesses suggests that our samples should be highly defective. Calculated limits are plotted in Fig. 1.9 for the $\mathrm{Ge}_x\mathrm{Si}_{1-x}$

system. The individual 65 Å $Ge_{0.5}Si_{0.5}$ layers within the superlattices are sufficiently thin to lie below the critical thickness predicted by the People and Bean model,[34] but exceed the limits calculated by Ball and Van der Merwe[35,36] and Matthews and Blakeslee.[37] However, treating the superlattices as alloys of equivalent total thickness and average composition[38] shows that the overall structures lie beyond all of the predicted limits.[34,35,36,37] Nevertheless, although samples grown at high temperatures display misfit dislocations in keeping with the predictions of the traditional critical thickness models, we find lattice mismatch to be elastically accommodated in a compositionally identical sample grown at 365 °C.

It is important to note that past critical thickness calculations have been based on *equilibrium* theories that neglect parameters such as temperature. Low-temperature growth techniques such as MBE clearly produce metastable structures[39] in which kinetics plays a dominant role. Thus, it should not be surprising that the appearance of misfit dislocations is rarely seen to be in agreement with theory. Our results suggest that critical thicknesses are not uniquely specified by lattice mismatch and material system. Recent attempts to model the relaxation of misfit stresses in a metastable system have met with some success.[40] Whether models such as these can be used to predict the onset of dislocation formation in a variety of structures remains to be determined.

It should be noted in passing that the precise definition of critical thickness is currently a matter of debate. In the past, critical thickness has typically been identified as the point at which average strain fields begin to deviate substantially from coherently strained values. With the development of cathodoluminescence techniques,[41] it has become possible to identify the thickness at which the first dislocation is nucleated in a thin film poorly lattice-matched to its substrate. The point at which this occurs is of questionable significance, however. Even under circumstances in which each of the appropriate growth parameters is precisely reproduced, the process of dislocation nucleation would appear to be better characterized by the activation conditions under which statistically significant densities of dislocations are observed, rather than by identification of the first fluctuation sufficient to nucleate a misfit dislocation on a 3" wafer. From a practical standpoint, the tolerance of a particular application to the presence of dislocations will determine a requirement of crystalline perfection that may be best described by activation energies characterizing the introduction of defects during the various stages of device growth and processing. Such activation energies are beginning to be examined in the Ge_xSi_{1-x} system.[42] Initial results suggest the presence of different activation energy domains, defined by the increased importance of dislocation interactions at high defect densities.

Regardless of the choice of definition of critical thickness, it is clear that the appearance of dislocations is not uniquely specified by a particular lattice mismatch and material system. We have demonstrated that growth conditions play a major role in inhibiting the introduction of dislocations within a film.* It is reasonable to expect that critical thicknesses should also be dependent on factors such as growth direction. Strain relaxation rates are known to vary substantially for films grown along different orientations;[43,44] identical critical thicknesses are exceedingly unlikely when either the component of the Burger's vector in the plane of the interfaces or the extent of the glide necessary for dislocation motion changes because of a change in growth direction.

---

*Note that dislocation formation is appropriately described as inhibited, rather than stimulated, by these growth conditions, as the calculations of Ball and Van der Merwe[35,36] show that the free-standing or unstrained cases represent substantially lower-energy states than the commensurate limit for the samples examined here.

4.5 Conclusions

The accommodation of lattice mismatch in Ge_xSi_{1-x}/Si superlattices has been demonstrated to be highly dependent on the conditions under which a sample is grown. Dislocation densities of $1.5 \times 10^5 cm^{-1}$ and $< 10^5 cm^{-2}$ have been measured in compositionally identical superlattices grown at 530 °C and 365 °C, respectively. It is clear that by lowering growth temperatures it is possible to freeze a structure in a highly strained metastable state well beyond the critical thickness limits calculated by equilibrium theories. There appears to be a large kinetic barrier blocking dislocation nucleation or glide; the effect we observe cannot be explained by mismatched thermal expansion coefficients alone.

The film thickness at which dislocations appear is clearly dependent on growth conditions. While past theories provide equilibrium limits to defect-free growth, predicting the appearance of defects in samples grown at low temperatures will require consideration of the kinetics of defect formation. It should not be surprising that experimentally observed critical thicknesses vary substantially, given the importance of variations in growth conditions in fundamentally metastable structures. Recognizing that defect creation can be inhibited in severely mismatched systems should be important in growing heavily strained films of high quality. While the durability of these structures under prolonged use remains uncertain, by tailoring growth conditions it is possible to obtain defect-free structures well beyond the equilibrium critical thicknesses.

References

1. H. Jorke and H.-J. Herzog, *J. Electrochem. Soc.* **133**, 998 (1986).
2. M. D. Camras, J. M. Brown, N. Holonyak, Jr., M. A. Nixon, R. W. Kaliski, M. J. Ludowise, W. T. Dietze, and C. R. Lewis, *J. Appl. Phys.* **54**, 6183 (1983).
3. Compare, for example, T. G. Andersson, Z. G. Chen, V. D. Kulakovskii, A. Uddin, and J. T. Vallin, *Appl. Phys. Lett.* **51**, 752 (1987) and N. G. Andersson, W. D. Laidig, R. M. Kolbas, and Y. C. Lo, *J. Appl. Phys.* **60**, 2361 (1986).
4. R. H. Miles, T. C. McGill, S. Sivananthan, X. Chu and J. P. Faurie, *J. Vac. Sci. Technol. B* **5**, 1263 (1987).
5. B. W. Dodson, J. Y. Tsao, and P. A. Taylor, *Proceedings of the Third International Conference on Superlattices, Microstructures, and Microdevices*, to be published.
6. K. Sakamoto, T. Sakamoto, S. Nagao, G. Hashiguchi, K. Kuniyoshi, and Y. Bando, *Jpn. J. Appl. Phys* **26**, 666 (1987).
7. G. J. Whaley and P. I. Cohen, *J. Vac. Sci. Technol. B* **6**, 625 (1988).
8. T. Tatsumi, H. Hirayama, and N. Aizaki, *Appl. Phys. Lett.* **52**, 895 (1988).
9. H. Temkin, J. C. Bean, A. Antreasyan, and R. Leibenguth, *Appl. Phys. Lett.* **52**, 1089 (1988).

10. G. L. Patton, S. S. Iyer, S. L. Delage, S. Tiwari, and J. M. C. Stork, *IEEE Electron Device Lett.* **EDL-9**, 165 (1988).

11. T. P. Pearsall and J. C. Bean, *IEEE Electron Device Lett.* **EDL-7**, 308 (1986).

12. T. P. Pearsall, J. Bevk, L. C. Feldman, J. M. Bonar, J. P. Mannaerts, and A. Ourmazd, *Phys. Rev. Lett.* **58**, 729 (1987).

13. K. Eberl, G. Krötz, R. Zachai, and G. Abstreiter, to be published.

14. I. Morrison and M. Jaros, *Superlattices and Microstructures* **2**, 329 (1986).

15. S. Froyen, D. M. Wood, and A. Zunger, to be published.

16. Y. Rajakarunanyake and T. C. McGill, unpublished.

17. H. Temkin, J. C. Bean, T. P. Pearsall, N. A. Olsson, and D. V. Lang, *Appl. Phys. Lett.* **49**, 155 (1986).

18. J. C. Bean, in *Silicon Molecular Beam Epitaxy*, edited by E. Kasper and J. C. Bean (Chemical Rubber, Boca Raton, FL, 1987).

19. D. C. Houghton, D. J. Lockwood, M. W. C. Dharma-Wardana, E. W. Fenton, J.-M. Baribeau, and M. W. Denhoff, *J. Cryst. Growth* **81**, 434 (1987).

20. A. Ishizaka, K. Nakagawa, and Y. Shiraki, *Collected Papers of MBE-CST-2, 1982, Tokyo* (Japanese Society of Applied Physics, Tokyo, 1982), p. 183.

21. D. C. Streit and F. G. Allen, *J. Appl. Phys.* **61**, 2894 (1987).

22. J. C. Bean, T. T. Sheng, L. C. Feldman, A. T. Fiory, and R. T. Lynch, *Appl. Phys. Lett.* **44**, 102 (1983).

23. E. Kasper, *Festkörperprobleme* **27**, 265 (1987).

24. I. J. Fritz, *Appl. Phys. Lett.* **51**, 1080 (1987).

25. M. M. J. Treacy, J. M. Gibson, *J. Vac. Sci. Technol. B* **4**, 1458 (1986).

26. R. J. Hauenstein, A. T. Hunter, R. H. Miles, and T. C. McGill, unpublished.

27. P. Voisin, *Surf. Sci.* **168**, 546 (1986).

28. H. P. Klug and L. E. Alexander, *X-ray Diffraction Procedures for Polycrystalline and Amorphous Materials* (Wiley, New York, 1974).

29. *International Tables for X-ray Crystallography*, edited by C. H. MacGillavry and G. D. Rieck (Kynoch, Birmingham, 1963).

30. L. C. Feldman, J. W. Mayer, and S. T. Picraux, *Materials Analysis by Ion Channeling* (Academic, New York, 1982).

31. W.-K. Chu, J. W. Mayer, and M.-A. Nicolet, *Backscattering Spectrometry* (Academic, New York, 1978).

32. A. T. Fiory, L. C. Feldman, J. C. Bean, and I. K. Robinson, *Mat. Res. Soc. Symp. Proc.* **25**, 497 (1984).

33. *American Institute of Physics Handbook*, edited by D. E. Gray (McGraw-Hill, New York, 1972).

34. R. People and J. C. Bean, *Appl. Phys. Lett.* **47**, 322 (1985); **49**, 229(E) (1986).

35. J. H. Van der Merwe, *J. Appl. Phys.* **34**, 123 (1963).

36. C. A. B. Ball and J. H. Van der Merwe, in *Dislocations in Solids, Volume 6*, edited by F. R. N. Nabarro (North Holland, Amsterdam, 1983), p. 122.

37. J. W. Matthews and A. E. Blakeslee, *J. Cryst. Growth* **27**, 118 (1974); **29**, 273 (1975); **32**, 265 (1976).

38. R. Hull, J. C. Bean, F. Cerdeira, A. T. Fiory, and J. M. Gibson, *Appl. Phys. Lett.* **48**, 56 (1986).

39. A. T. Fiory, J. C. Bean, R. Hull, and S. Nakahara, *Phys. Rev. B* **31**, 4063 (1985).

40. B. W. Dodson and J. Y. Tsao, *Appl. Phys. Lett.* **51**, 1325 (1987); **52**, 852(E) (1988).

41. P. L. Gourley, T. J. Drummond, and B. L. Doyle, *Appl. Phys. Lett.* **49**, 1101 (1986).

42. R. Hull, J. C. Bean, R. E. Leibenguth, and D. J. Werder, *Mater. Res. Soc. Proc.*, to be published.

43. H. Munekata, L. L. Chang, S. C. Woronick, and Y. H. Kao, *J. Cryst. Growth* **81**, 237 (1987).

44. H. Munekata, A. Segmüller, and L. L. Chang, *Appl. Phys. Lett.* **51**, 587 (1987).

Appendix A

Appendix

Electronic band gaps have been calculated for a variety of superlattices composed of II-VI semiconductors. Calculations are based on the Bastard model[1] described in Section 2.4, with strain effects included through a four-parameter deformation potential.[2] The superlattices are assumed to be strained in a free-standing configuration. As explained in Section 2.4, this configuration minimizes the elastic energy of the coherently-strained superlattice. A (100)-oriented zinc-blende crystal structure is assumed.

Parameters used in the calculations are listed in Table A.1.

Table A.1: Properties of II-VI semiconductors.

	CdTe	CdSe	CdS	ZnTe	ZnSe	ZnS
$E_{\mathbf{gap}}^{4K}$	1.606	1.84	2.56	2.38	2.82	3.80
E_v	-0.88	-1.33	-1.73	-0.98	-1.41	-1.87
Δ_0	0.91	0.42	0.07	0.92	0.43	0.07
m_h^*	1.38	1.6	2.	1.27	1.44	1.76
E_p	20.7	23.	21.	19.1	24.2	20.4
a_0	6.481	6.05	5.820	6.104	5.669	5.409
a	1.23	1.24	1.31	1.35	1.35	1.58
c	-2.2	-2.47	-2.68	-2.7	-2.82	-3.60
b	-1.18	-1.	0.4	-1.78	-1.2	0.53
d	-4.83	-3.	-3.	-4.58	-3.81	-3.71
C_{11}	5.351	7.4	8.581	7.13	8.10	10.46
C_{12}	3.681	4.52	5.334	4.07	4.88	6.53
C_{44}	1.994	1.317	1.487	3.12	4.41	4.613

$E_{\mathbf{gap}}$, E_v, Δ_0, E_p, a, c, b, and d are in eV; m_h^* is expressed as a fraction of a free-electron mass, a_0 is in Å, and elastic constants C are in units of 10^{11}dyne/cm^2. Band gaps, spin-orbit splittings, heavy-hole masses, and p-matrix elements are from Ref. 3. Absolute energies of valence band edges were taken from Refs. 4 and 5. Deformation potentials are from Refs. 6,7,8. Lattice constants and elastic constants are from Ref. 9.

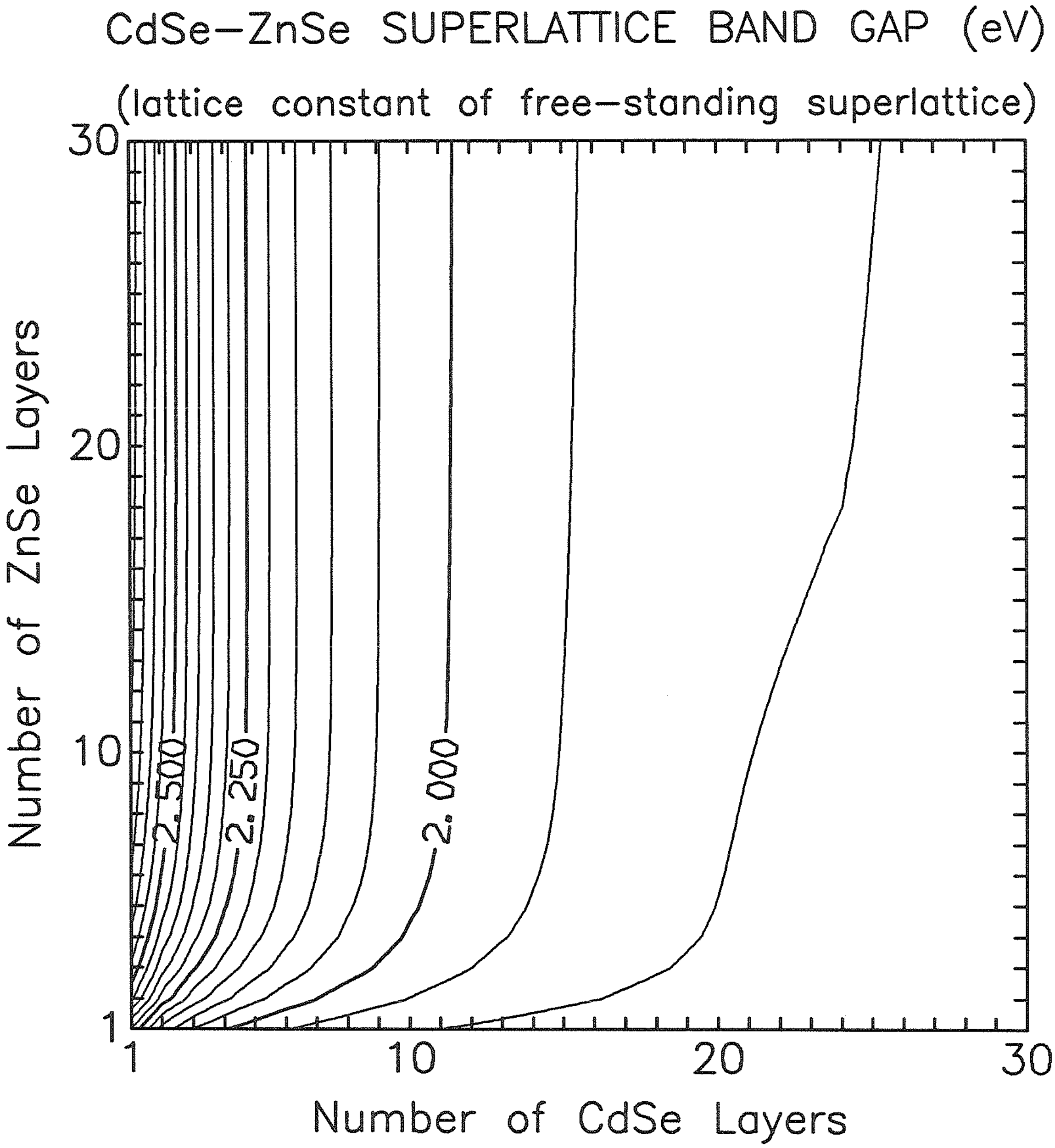

Figure A.1: Calculated CdSe/ZnSe superlattice band gaps with strain effects included. Contour interval is 50 meV. Calculations assume in-plane lattice constants appropriate to free-standing superlattices.

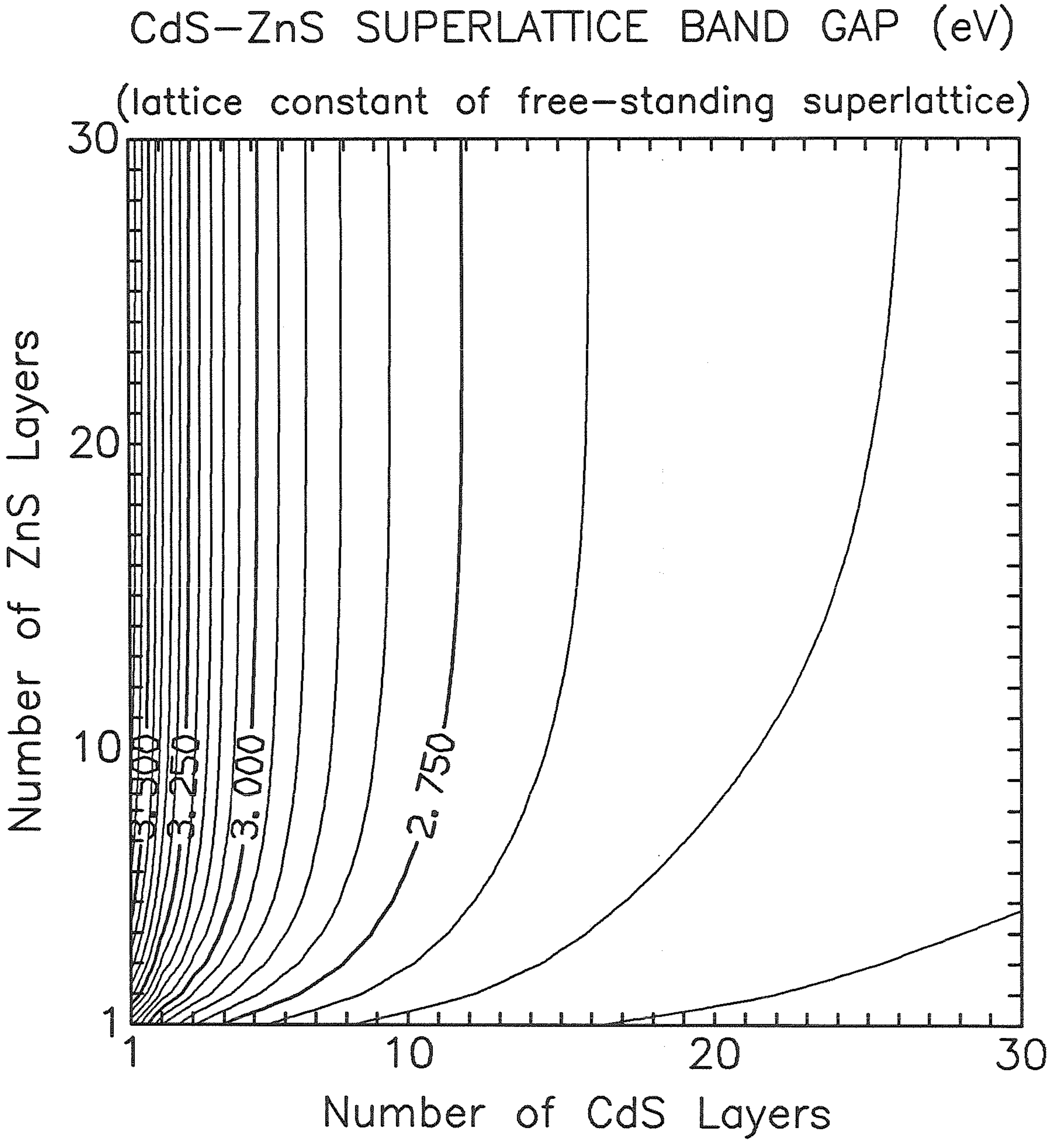

Figure A.2: Calculated free-standing CdS/ZnS superlattice band gaps.

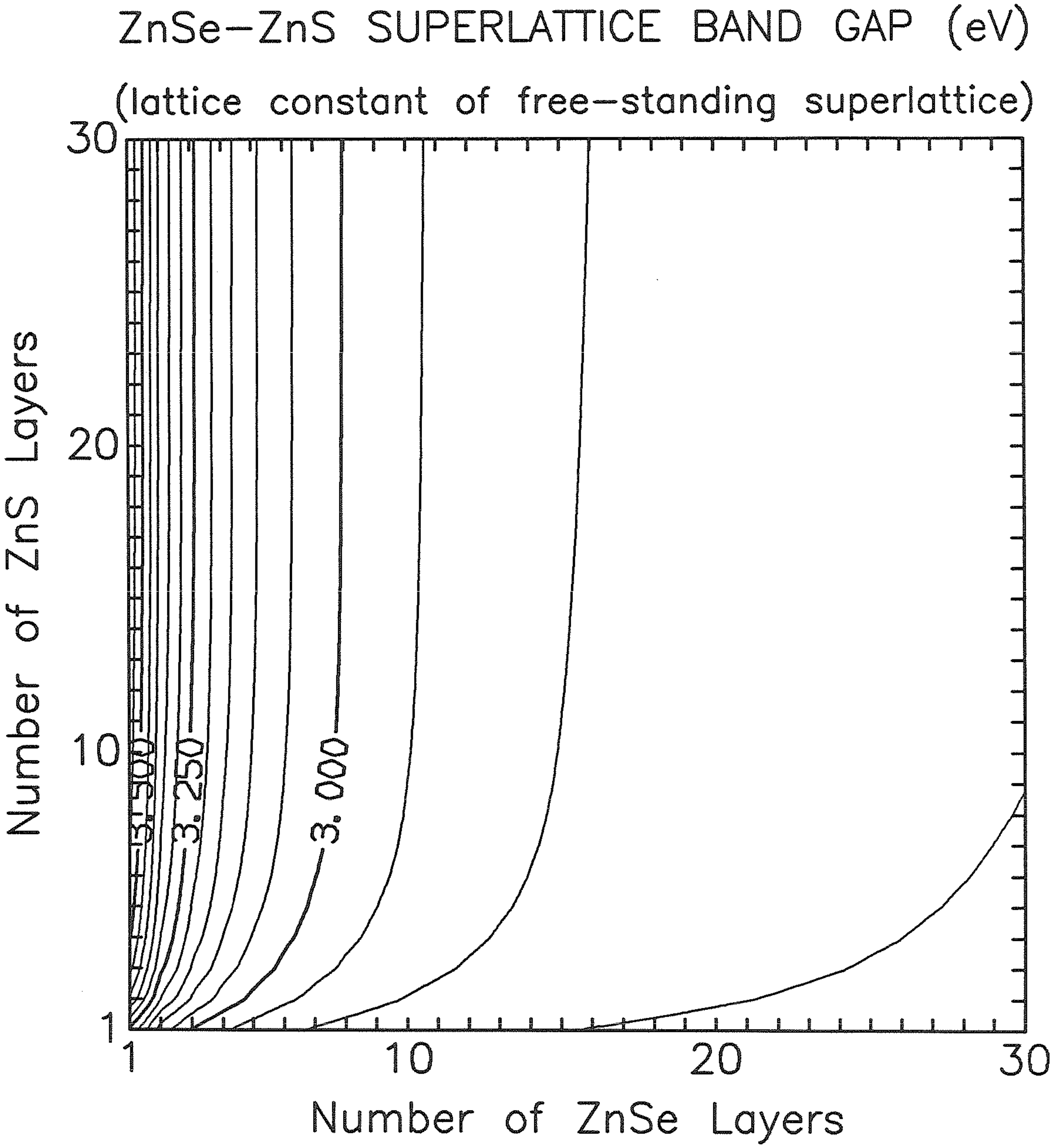

Figure A.3: Calculated free-standing ZnS/ZnSe superlattice band gaps.

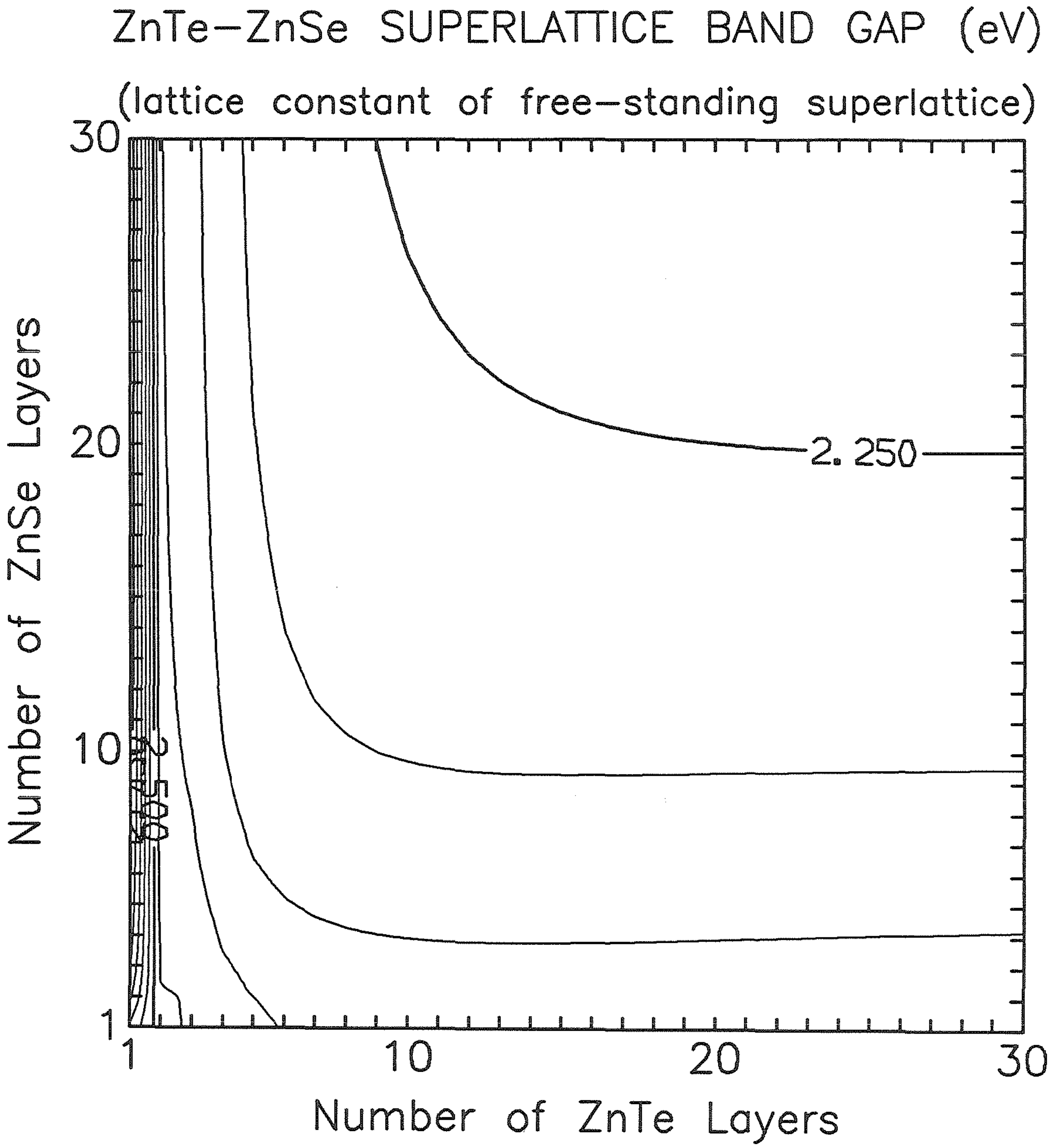

Figure A.4: Calculated free-standing ZnSe/ZnTe superlattice band gaps.

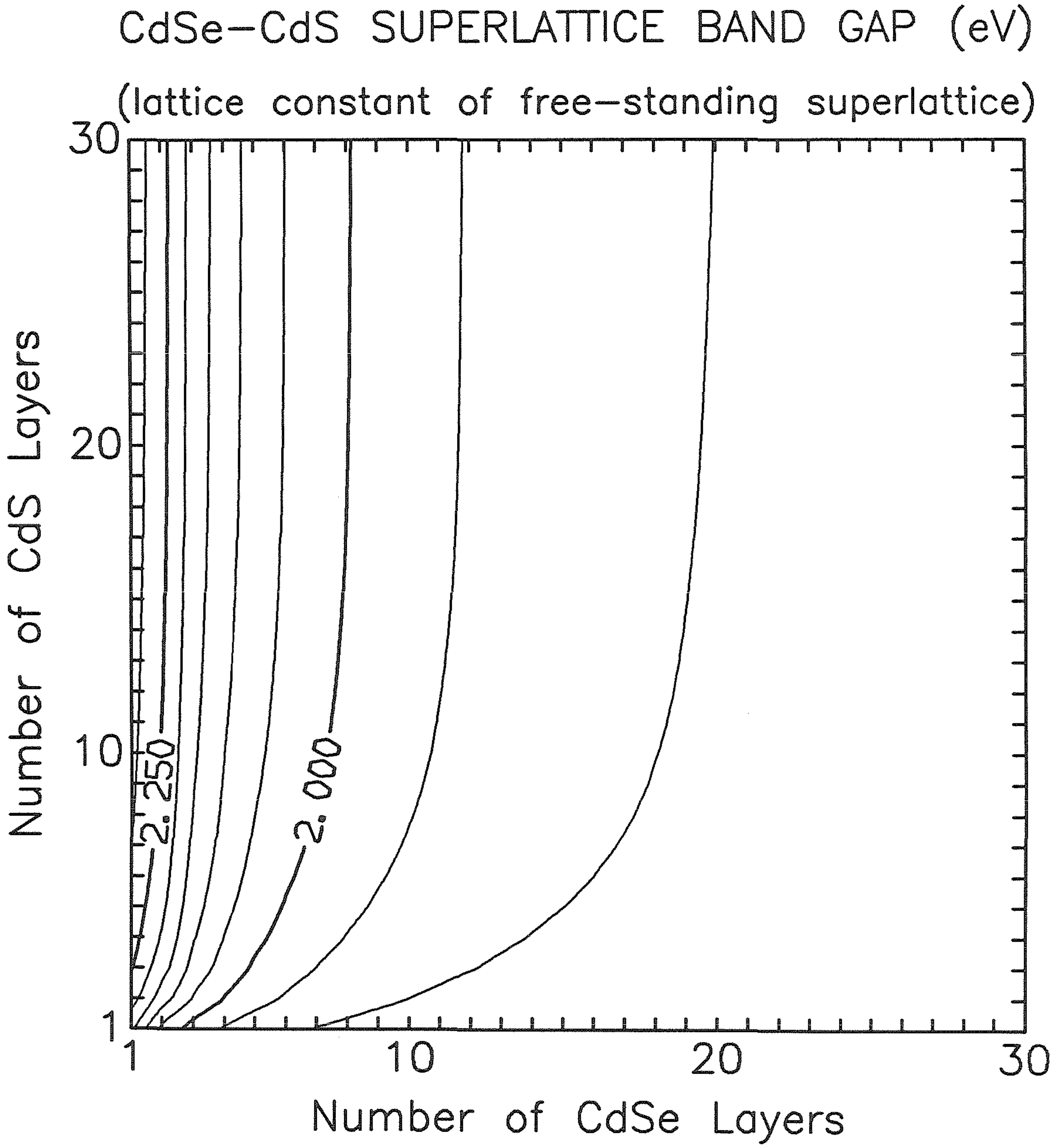

Figure A.5: Calculated free-standing CdS/CdSe superlattice band gaps.

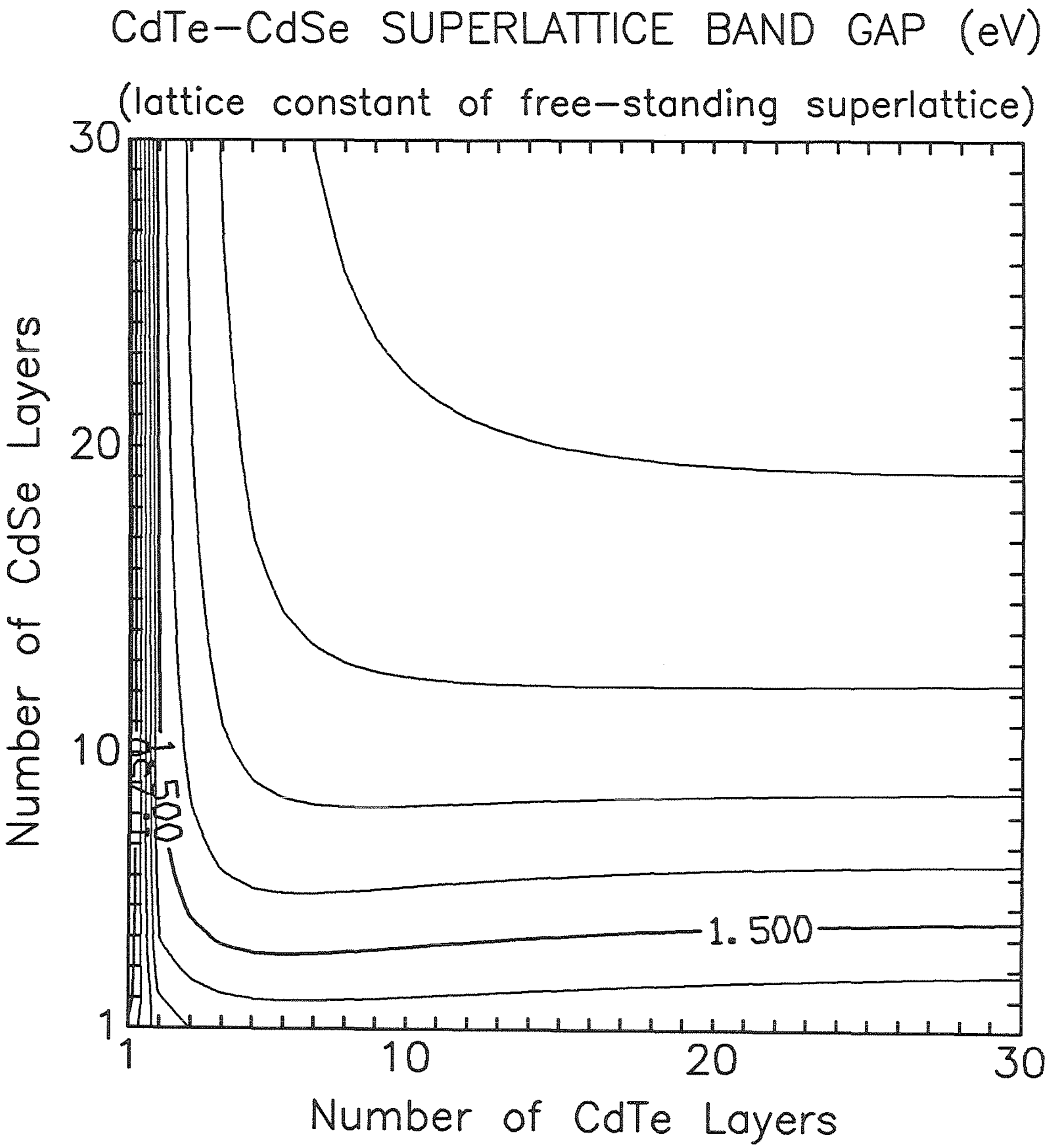

Figure A.6: Calculated free-standing CdSe/CdTe superlattice band gaps.

References

1. G. Bastard, *Phys. Rev. B* **24**, 5693 (1981); **25**, 7584 (1982).
2. G. L. Bir and G. E. Pikus, *Symmetry and Strain-Induced Effects in Semiconductors* (Keter, Jerusalem, 1974).
3. P. Lawaetz, *Phys. Rev. B* **4**, 3460 (1971).
4. A. D. Katnani and G. Margaritondo, *Phys. Rev. B* **28**, 1944 (1983).
5. W. A. Harrison and J. Tersoff, *J. Vac. Sci. Technol. B* **4**, 1068 (1986).
6. A. A. Kaplyanskii and L. G. Suslina, *Soviet Physics - Solid State* **7**, 1881 (1966).
7. D. G. Thomas, *J. Appl. Phys. Suppl.* **32**, 2298 (1961).
8. D. L. Camphausen, G. A. N. Connell, and W. Paul, *Phys. Rev. Lett.* **26**, 184 (1971).
9. *Physics and Chemistry of II-VI Compounds*, edited by M. Aven and J. S. Prener (Wiley, New York, 1967).